Technische Universität München
Fakultät für Maschinenwesen
Lehrstuhl für Flugantriebe

Experimental and Numerical Investigation of a Centrifugal Compressor Stage with Variable Inlet Guide Vanes

Nan Chen, M.Sc.

Vollständiger Abdruck der von der Fakultät für Maschinenwesen der Technischen Universität München zur Erlangung des akademischen Grades eines

Doktor-Ingenieurs (Dr.-Ing.)

genehmigten Dissertation.

Vorsitzende(r): Prof. Dr.-Ing. Hartmut Spliethoff

Prüfer der Dissertation:

1. Prof. Dr.-Ing. Oskar Haidn
2. Prof. Dr.-Ing. Stefan Schlechtriem

Die Dissertation wurde am 21.11.2016 bei der Technischen Universität München eingereicht und durch die Fakultät für Maschinenwesen am 18.01.2017 angenommen.

This dissertation is dedicated to
my parents and my wife
for their endless support and encouragement,
and in memory of
Professor Hans-Peter Kau († 05.05.2013),
Ordinarius des Instituts für Flugantriebe.

Acknowledgment

First of all, I would like to thank my doctoral supervisor, Professor Dr. Oskar Haidn, and my academic supervisor Dr. Wolfgang Erhard, for their intensive instructions on my research activities at the institute. They have encouraged my endeavor spirit to analyze engineering problems with careful considerations in technical details and from wider industrial aspects.

I give my special thanks to my colleague M.Sc. Sebastian Lang for his systematic coaching with great patience on the test rig and for his assistance in the problem-solving during the rig setup and operation. I would like to also thank my colleague Dipl. Marcel Schmieder for his collaborations in helping with the the test rig preparation.

I give my deep appreciation to the colleagues at GE Global Research, including Dr. Christian Aalburg, Dr. Ismail Sezal, and Dipl. Robbert Pannekeet, and Dr. Matthias Lang, for their collaborations on the TUM-GE research projects. In respect of numerical simulations I would like to thank my colleague Dipl. Christian Bauer, Dipl. Marc Kainz and Dr. Momme Allalen at Leibniz Supercomputing Centre for their kind suggestions.

Many thanks go to many colleagues at the Institute for creating such a pleasant working environment. I would like to especially thank Professor Dr. Hans Rick, Professor Dr. Andreas Hupfer, Dipl. Daniel Paukner, Dipl. David Rockel, M.Sc. Joona Seppälä, M.Sc. Meng Luo, and Dipl. Martin Kerler, for sharing the daily tasks on research and teaching activities. I would like to sincerely express my thanks to our workshop colleagues, Mr. Roland Grubert, Miss Zoe Gerstung and Mr. Bernhard Ritter, for the high-quality mechanical parts they have manufactured for my project.

Last but not the least, I would like to give my greatest gratitude to our secretary, Mrs. Angelika Heininger, for her enthusiasm, dedication and the enjoyable working time she has shared with us.

Garching, December 2016
Nan Chen

Abstract

Centrifugal compressors are widely used in the Oil & Gas industry and jet engine applications to compress the working fluid to higher pressure levels. For a centrifugal compressor, variable inlet guide vanes (IGV) can be introduced to expand the compressor operation range by adding pre- or counter-swirl into the impeller inlet flow. A successful IGV design provides a maximum spectrum of setting angles with correct flow guidance, minimum aerodynamic losses and smallest flow distortion. This dissertation covers the experimental and numerical investigation of three different IGV designs developed for a typical industrial process compressor. The first IGV comprises of symmetrical, standard NACA airfoils as the baseline. The second IGV configuration contains uniquely cambered, circumferentially non-uniform profiles. The third IGV is based on a circumferentially non-uniform multi-airfoil, which consists of a fixed front part and an adjustable tail. The three IGV designs are firstly experimentally validated by integration into a typical Oil & Gas centrifugal compressor stage on the test rig. Subsequently, CFD simulations are performed to investigate the interactions between IGV and impeller and their impact on the impeller performance. It is found that the two new IGV designs can reduce pressure losses and flow non-uniformities while keeping moderate incidence angles at large IGV setting angles, which together contribute to the significant improvement on the centrifugal compressor performance.

Kurzfassung

Radialverdichter sind weit verbreitet in der Oil & Gas Industrie und bei Flugtriebwerken zur Komprimierung des Arbeitsfluides auf höhere Druckniveaus. Bei einem Radialverdichter können zur Erzeugung eines Vordralls verstellbare Leitschaufeln am Eintritt (IGV) eingeführt werden, um den Betriebsbereich der gesamten Verdichterstufe zu erweitern. Eine IGV Konstruktion soll ein möglichst breites Spektrum von Anstellwinkeln mit korrekter Strömungsführung bei minimalen aerodynamischen Verlusten und geringen Strömungsasymmetrien bereitstellen. In dieser Dissertation werden drei verschiedene IGV Konfigurationen, die für einen typischen Radialverdichter entwickelt wurden, experimentell sowie numerisch untersucht. Das Referenz-IGV besteht aus symmetrischen NACA Profilen. Die zweite IGV Konfiguration verwendet einseitig gewölbte Profile, die über den Umfang des Einlaufs variable sind. Die dritte Konfiguration beinhaltet einen umfangsasymmetrischen, zweiteiligen Flügel bestehend aus einem festen Vorderteil und einem verstellbaren Heckteil. Alle drei IGV Typen werden zuerst in eine typische Oil & Gas Radialverdichterstufe am rotierenden Prüfstand integriert und experimentell validiert. Nachfolgend werden durch CFD Simulationen die Interaktionen zwischen IGV und Verdichter und das daraus resultierende Betriebsverhalten des Verdichters numerisch untersucht. Es kann gezeigt werden, dass die zwei neuen IGV Konfigurationen in der Lage sind, für große Anstellwinkel eine gute Anströmung mit angemessener Inzidenz bei geringeren Druckverlusten zu erzeugen. Dies führt zu erheblichen Verbesserungen des Betriebsverhaltens des gesamten Radialverdichters.

Contents

List of Figures

List of Tables

Nomenclature

Latin Symbols

A	[m^2]	Area
C	[−]	Constant
D	[m]	Diameter
L	[m]	Length
Ma	[−]	Mach number
Mu	[−]	Impeller tip Mach number
N	[RPM]	Rotational shaft speed
P	[kW]	Working power
Re	[−]	Reynolds number
Q	[m^3/s]	Volumetric flow rate
T_s	[K]	Static temperature
T_t	[K]	Total temperature
T_u	[−]	Turbulence intensity
U	[m/s]	Mean velocity
V	[m^3]	Volume
X,Y,Z	[m]	Cartesian coordinates
a	[m/s]	Speed of sound
b	[m]	Channel width
c	[m/s]	Absolute velocity
c_p	[J/(kg · K)]	Specific heat at constant pressure
h	[−]	Head coefficient or static enthalpy
h_t	[J/kg]	Specific total enthalpy
$\dot{m}$	[kg/s]	Mass flow rate
n	[−]	Exponent
p_s	[Pa]	Static pressure
p_t	[Pa]	Total pressure

q	[−]	Physical quantity
r	[m]	Radius
s	[J/kg]	Entropy
s_l	[−]	Stagnation loss
t	[s]	Time
u	[m/s]	Impeller tip rotational velocity
$u^{'}$	[m/s]	Velocity fluctuation
w	[m/s]	Relative velocity or specific work
y^+	[−]	Dimensionless wall distance
z	[−]	Blade number

Greek Symbols

α	[Deg]	Absolute velocity angle
β	[Deg]	Relative velocity angle
Δ	[−]	Difference or error
η	[−]	Polytropic efficiency
γ	[Deg]	Pitch angle
κ	[−]	Isentropic exponent
ω	[rad/s]	Angular velocity
ϕ	[−]	Flow coefficient
ψ	[Deg]	Yaw angle
ρ	[kg/m^3]	Density
τ	[−]	Work coefficient
θ	[Deg]	Circumferential coordinate

Abbreviations

BPP	Blade passing period
CFD	Computational fluid dynamics
DP	Design point
EXP	Experiment

FA	Full annulus
FFT	Fast Fourier transformation
IGV	Inlet guide vane(s)
LC	Loss coefficient
LFA	Institute for Flight Propulsion
NP	Nominal point
OL	Overload
PCB	Fast-response pressure sensor by PCB
PL	Partload
PS	Pressure side
R.S	Rotating Stall
SS	Suction side
SP	Single passage
STE	Steady simulation
TBR	Transient blade row
TC	Thermocouple
TE	Trailing edge
TPR	Total pressure ratio
TUM	Technische Universität München
TRA	Transient simulation
abs	Absolute
amb	Ambient conditions
ax	Axial direction
e.g	For example
m	Meridional direction
n	Normalized
p	Polytropic
r	Radial direction
shr	Shroud
u	Circumferential direction

Chapter 1

Introduction

Centrifugal compressors are widely applied in the Oil & Gas and aviation industry to provide pressured gases. Since the end of the 19^{th} century, centrifugal compressors began to be widespread in ventilation, pneumatic transportation, refrigeration and petrochemical processes. During the first decade in the 20^{th} century, centrifugal compressors were indispensable for the earliest gas turbines, such as the first successful industrial gas turbine patented by Aegidius Elling as described in Krain [57]. Later in the 1930s, the two inventors for jet engines, Frank Whittle in England and Von Ohain in Germany, individually chose a centrifugal compressor as part of compressor system for their first jet engines. Today, centrifugal compressors are commonly found in small aircraft engines for business jets, helicopters and axillary power units (APUs),or as process compressors for industrial applications. The development of centrifugal compressors to achieve higher efficiency and wider operation range requires more advanced control mechanisms such as inlet guide vanes (IGVs). As an introduction, this chapter briefly summarizes the background of industrial centrifugal compressors and the early milestones on the development of IGVs.

1.1 Research Background

A centrifugal compressor is a radial turbo machine which compresses its working fluid to higher pressure levels. A centrifugal compressor distinguishes itself from an axial compressor by its outlet flow primarily in radial direction. Compared to axial compressors, since the flow passes through the blade passages with an increasing radius, more kinetic energy can be transferred by the additional centrifugal force. This results in more compact designs and larger total pressure ratios for centrifugal compressors compared to their axial counterparts within the same mass flow rate ranges. Although centrifugal compressors were firstly applied in aircraft engines, the development of gas turbines later in the 20^{th} century tends to shift the focus to axial compressors due to their higher isentropic efficiencies

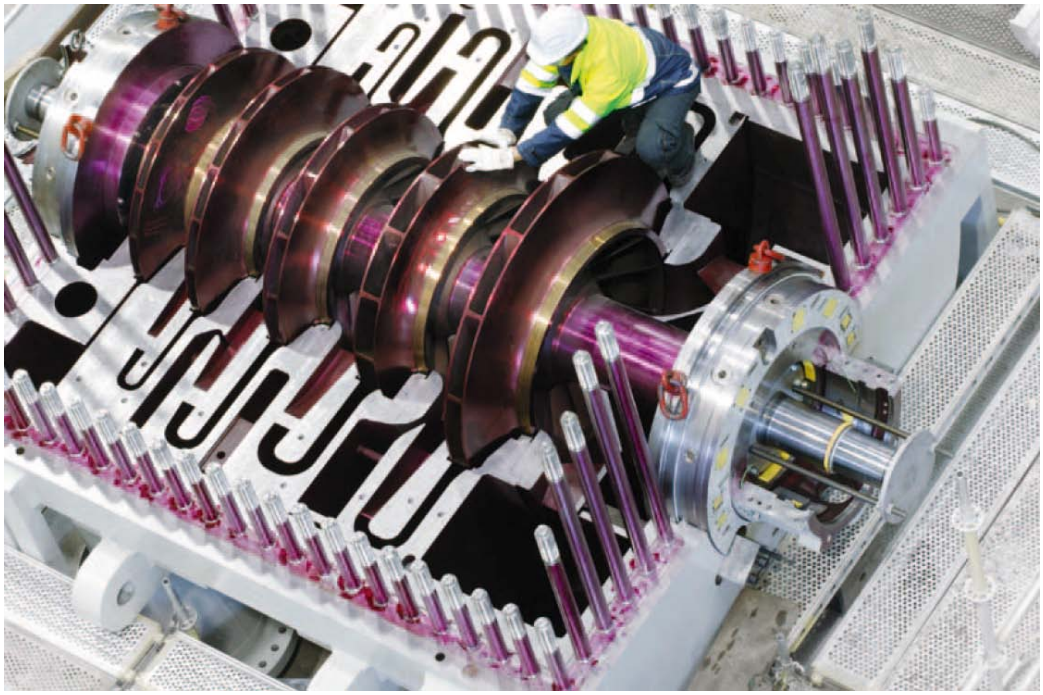

Figure 1.1: Typical multistage process compressor from Siemens [74]

and larger power outputs when they have the same frontal areas as the centrifugal compressors. Nevertheless, today centrifugal compressors are still commonly found in small gas turbines, such as the last stage of aircraft engines for business jets and helicopters. Saravanamuttoo [69] summarized the advantages of centrifugal compressors as follows:

- High suitability for handling small mass flow rates;
- Good flexibility to deal with varying mass flow rates;
- Compact design with a shortened length;
- High resistance to damages by external objects;
- Insensitivity to the performance losses due to the deposit built-up on the blades.

In addition, due to its superb reliability over a wide operation range, a centrifugal compressor stage is often found as process compressor in the Oil & Gas, refinery and petrochemical industry for delivering industrial gases (GE [36]). For example, Figure 1.1 illustrates a multistage process compressor applied in the Oil & Gas industry from Siemens [74]. It contains a series of centrifugal compressor stages located on the same machine axis, each comprising of radial inlet, impeller, diffuser, U-bend, return channel and radial outlet. In contrast to a centrifugal compressor used in aircraft engines, the blade passages of a

process compressor are usually closed as the so-called shrouded impeller. A shrouded impeller can prevent the flow leakage at the blade tip region by completely eliminating the tip clearance. However, since its shroud part becomes part of the rotor, a shrouded impeller is inevitably subject to additional centrifugal forces Borm [16]. Furthermore, according to Cumpsty [22] for a multistage compressor consisting of several impellers, a simultaneous setting of axial location and tip clearance for all the open impellers is extremely difficult. Therefore, nowadays process compressors are almost exclusively shrouded impellers. Downstream from the impeller, the stator is mostly a simple channel called vaneless diffuser. A vaneless diffuser is characterized by its more extended operation range which favors the operation conditions with larger mass flow variations. As a compromise, a vaneless diffuser often has lower peak efficiency compared to other vaned diffuser types.

For a process compressor, the operation range is an essential criterion for evaluating the stage performance, because in practice the amount of working fluid for process compressor may greatly vary Lüdtke [60]. The operation range of a process compressor is determined by the maximum and minimum allowable mass flow rates. While the maximum mass flow rate is limited by compressor choke, the minimum mass flow rate is more dangerous because it involves flow instabilities in the blade passages which further lead to stall or surge. In practice, a reduction in the mass flow may occur when the amount of gas delivery has to decrease from the peak period. In order to deal with the mass flow variations, various types of stage regulation mechanisms have been introduced, such as tip flow injection and extraction (Lang [59]), variable drive train Greco ([26]), bypass regulation (Lüdtke [60]), variable inlet guide vanes (Rodgers [68]) and variable diffuser vanes Simon ([75]).

Among these possibilities, the concept of inlet guide vane has been adopted as an effective control mechanism, which adds pre-swirl and counter-swirl to the compressor flow, so that the flow incidence at partload and overload can be corrected. Particularly in the Oil & Gas industry, variable IGVs are often installed into an inlet plenum which is located upstream of the impeller as illustrated in Figure 1.2-(a). With the application of such an IGV plenum, the performance turndown of a centrifugal compressor stage, which typically occurs at partload to the extend of typically 20% from its peak efficiency (shown in Figure 1.2-(b)), can be effectively recovered.

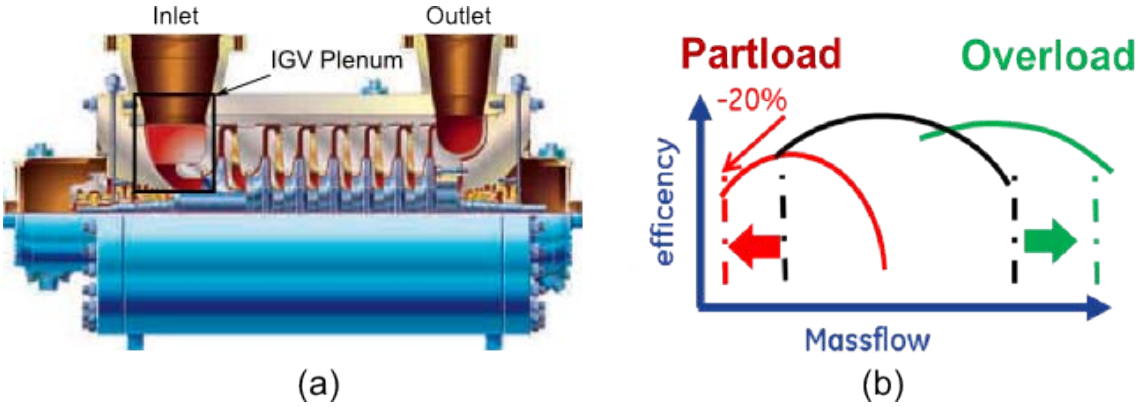

Figure 1.2: (a) A multistage process compressor with radial plenum at the stage inlet from GE [36]; (b) Performance turndown with shifted speedlines by IGVs at partload and overload

1.2 Literature Review

The early studies on the inlet guide vanes can be traced back to the 1960s. Traupel [84] discussed the theoretical benefits of adding pre-swirl to the centrifugal compressor by velocity diagram analysis. Steinke [79] divided the pre-swirl into four patterns: inverse, constant, linear, and quadratic swirl. Whitfield [86] experimentally measured the flow rate of a centrifugal compressor with/without IGVs, and found that the group with IGVs had an increase in the surge margin up to 40%. Similarly, Rodgers [68] experimentally proved that the IGVs could prohibit a stall in the impeller at extremely small mass flow rates. Later Grimaldi [41] measured an IGV stage equipped in a transonic compressor to provide a reduced Mach number for the compressor tip leading edge. Similar results were found by Shaw [73] with another IGV stage for a transonic fan.

The shape of IGV has evolved from its primitive flat plates into more sophisticated profiles with significant aerodynamic improvements. Firstly in the 1980s, a typical IGV shape was merely in the form of several uncambered vanes arranged in an annulus Ishino [53]. The first generation of guide vanes with simple profiled shapes were originated from the classic NACA profiles. Later some IGVs with cambered profile were introduced e.g. by Jackson [54] to further improve the flow guidance and pressure development on the blade surface at higher setting angles. With the advent of modern CFD techniques more advanced guide vanes were proposed in relatively quick design processes. For example, Coppinger [18] applied CFD simulations for the design of a tandem-shape IGV, which contained a straight frontal part and a tail. The pressure losses of this IGV profile were measured to be noticeably lower than the traditional flat-plate vanes. The related test results can be found in Coppinger [20] and [19]. Later on, Boehle [14] tested a similar flapped IGV for

highspeed compressible flow applications. This design was proved to be advantageous in producing flow conditions with reduced losses and controlled flow turning. Mohseni [64] further numerically investigated three different IGV profiles (symmetric, s-cambered and tandem) for a turbocharger. The flow simulation showed that the s-cambered IGV and tandem IGV successfully prevented the flow separations at higher IGV setting angles. The flapped IGV also finds its applications in the real transonic compressors and fans especially for military jet engines Hobson [52], where a large coverage of various operations under various flight conditions is of prior concern. Recently, a new concept of IGV was proposed by Hill [50], which contained a dedicated flow circulation mechanism on the blade to make use of the Coanda effect for flow separation prevention. Besides the investigations on the aerodynamic aspects of IGV, several other research studies concentrate on the mechanic aspects when the IGV is put into practice together with its affiliated mechanical parts. Some relevant studies can be found in Hensges [48] and Duong [28] which discussed the damage modes under aero-mechanical interactions, and Ebisawa [29] on the topic of the rotordynamics of a centrifugal compressor stage with the IGV blades installed. In addition to the application of IGV, some other devices can be also utilized to provide similar swirling effects to the impeller, such as the upstream slots and fins found in Tamaki [81] and [82].

The aerodynamic performance of an IGV stage is determined not only by the guide vanes, but also by the position where the IGVs are installed. For example, Cui [21] simulated an impeller together with a suction elbow at the inlet section to evaluate the unsteady effects with/without IGV to the stage. Kim [56] proved that an additional IGV stage inside a radial inlet section could deliver more homogeneous flow at the impeller inlet.

Despite of the positive effects of pre- and counter-swirl generation, IGVs may also impose some types of undesired flow effects to the downstream compressor blades. Some of the negative impacts are e.g. the stator-rotor interactions manifested as the blade vibrations Zemp [91], the wake impingement Soranna [78], and the tip-vortex flows Leichtfuss [61]. In order to investigate these flow behaviors, modern measurement technologies may offer an access to the internal flow structures related to the IGVs. For example, Zemp [92] measured the transient blade pressure fluctuations to evaluate the IGV-induced blade forces. Soranna [78] visualized the wake impingement of the upstream IGVs on the downstream rotor stage using the particle image velocimetry (PIV). Händel [51] employed a stepwise traversing wake probe to measure the influence of Reynolds number, Mach number and flow angle at the blade regions inside the IGV stage with high resolution.

In practice, sometimes the variable IGVs can be combined with other regulation mecha-

nisms together to achieve best synergic effects. As an example, Simon [75] measured that an overall stage efficiency improvement could be achieved by a combination of variable IGVs and variable diffuser vanes with proper coupling strategies. Similarly, Tetu [83] applied CFD to show an improved stage performance realized by a variable diffuser geometry and IGVs working simultaneously. Greco [26] evaluated the further potentials in the IGVs for a centrifugal compressor stage in addition to an already applied speed regulation. It is expected that in future, the IGVs will be likely adopted as just one of several control mechanisms at the same time.

1.3 Project Description

This project focuses on the the validation of three different IGV configurations for a centrifugal compressor stage. Based on the first IGV design using NACA profile as the baseline, two new IGV configurations have been developed within the scope of this study. The first new IGV design has a cambered profile, and the second new design contains a multi-part airfoil with a rotating tail. These three IGV configurations were validated by a complete rotating test campaign, which was accomplished by applying each of the three IGV configurations respectively to a typical Oil & Gas centrifugal compressor stage. The experimental results from the test campaign were then compared with the previous static test results on the IGV plenum alone as well as the related CFD predictions. After the test campaign was accomplished, a CFD study was performed to better understand the reasons for the stage performance achieved by the new IGVs, and the internal flow mechanisms. As a whole, this project can be seen as a validation process for the three IGV configurations by both experimental tests and CFD simulations.

1.4 Dissertation Outline

This dissertation contains a total of six chapters. After the introduction in Chapter 1, Chapter 2 provides the fundamental theories on the thermodynamics, the centrifugal compressor flow physics, and the inlet guide vane design. Chapter 3 describes the test rig including the instrumentation setup, and then the measurement results collected from the test campaign with three IGV configurations. Chapter 4 presents the CFD simulations applying the experimental data from the stage performance tests. Finally, Chapter 6 gives a summary for the whole project and an outlook on the future work.

Chapter 2

Theory and Fundamentals

This chapter provides the theoretical background and fundamental knowledge for this research project. Firstly, the thermodynamics and performance characteristics for centrifugal compressors are introduced. The second part describes the centrifugal compressor flow physics with a focus on the impeller inlet flow, where the inlet guide vanes have a direct impact. Finally, the IGV design is presented including its working principle, type of swirl, aerodynamic design and mechanical components.

2.1 Thermodynamics and Performance Characteristics

From a thermodynamic viewpoint, a compressor stage, which typically comprises of a rotor and a stator, can be treated as an open system with energy conversion and mass transfer across the system boundaries. During a compression process, the energy conversion involves the energy transfer from the mechanical energy of the rotor into the internal energy of the fluid. If the control system is non-adiabatic, the energy transfer still includes the heat transfer across the system boundaries. The mass transfer is characterized by the working fluid continuously entering and leaving the system. Particularly for a steady-state compressor stage with a constant mass flow rate, the thermal process can be expressed by the 1st Law of Thermodynamics:

$$P + \dot{Q} = \dot{m}\left[h_2 - h_1 + \frac{1}{2}(c_2^2 - c_1^2) + g(z_2 - z_1)\right] \tag{2.1}$$

It indicates that the sum of work done by the rotor and the heat transfer across the boundaries is equal to the amount of energy changes between the system inlet and system outlet, which are comprised of static enthalpy, kinetic energy and potential energy.

Due to the small density of most gaseous fluids, the potential energy change can be negligible. In addition, for an adiabatic system the heat transfer $\dot{Q}$ is zero. Under these two simplications the specific work of the rotor w can be calculated as:

$$w = \frac{P}{\dot{m}} = h_2 - h_1 + \frac{1}{2}(c_2^2 - c_1^2) = h_{t2} - h_{t1} = \Delta h_t \tag{2.2}$$

Based on the conservation of angular momentum described in Rick [67], the ideal sum of moments acting by the fluid on the rotor blade of a compressor can be expressed as:

$$M = \dot{m}\left(c_{u2} \cdot r_2 - c_{u1} \cdot r_1\right) \tag{2.3}$$

Assume that the leakage due to cavities and disk friction between the rotor and the shaft are negligible, the specific work w can be derived as:

$$w = \Delta h_t = c_{u2}u_2 - c_{u1}u_1 \tag{2.4}$$

This is known as the Euler's turbomachinery equation.

Given that:

$$c_{u2}u_2 = \frac{1}{2}\left(u_2^2 + c_2^2 - w_2^2\right); \quad c_{u1}u_1 = \frac{1}{2}\left(u_1^2 + c_1^2 - w_1^2\right) \tag{2.5}$$

Equation 2.4 can be transformed into a second form:

$$\Delta h_t = c_{u2}u_2 - c_{u1}u_1 = \frac{u_2^2 - u_1^2}{2} + \frac{c_2^2 - c_1^2}{2} - \frac{w_2^2 - w_1^2}{2} \tag{2.6}$$

With $h_t = h + \frac{c^2}{2}$, it can be rewritten as:

$$h_1 + \frac{1}{2}w_1^2 - \frac{1}{2}u_1^2 = h_2 + \frac{1}{2}w_2^2 - \frac{1}{2}u_2^2 \tag{2.7}$$

By defining a physical property "rothalpy" as $h_{rot} = h + \frac{1}{2}w^2 - \frac{1}{2}u^2$, it can be described as:

$$h_{rot,1} = h_{rot,2} \tag{2.8}$$

It shows that under all simplifications mentioned above, the rothalpy remains constant throughout the rotor.

Alternatively, for a working fluid traveling through a compressor stage, such as a centrifugal compressor including an impeller (rotor) and a diffuser (stator), its thermal process can

be illustrated by a h-s diagram in Figure 2.1 according to Lüdtke [60]. The performance parameters, which are defined to quantify the performance of the rotor (station 1 to 2), the stator (station 2 to 3) and the stage as a whole (station 1 to 3), can be easily visualized in the h-s diagram. Some of the main performance parameters applied for this study are:

- Total pressure ratio: the ratio between total pressure at rotor (or stage) outlet and total pressure at rotor (or stage) inlet.

$$\Pi_t = \frac{p_{t,out}}{p_{t,in}} \tag{2.9}$$

- Polytropic efficiency: the ratio between polytropic total enthalpy change and actual total enthalpy change.

$$\eta = \frac{\Delta h_{t,poly}}{\Delta h_t} = \frac{\kappa - 1}{\kappa} \cdot \frac{n}{n-1} = \frac{\kappa - 1}{\kappa} \cdot \frac{\ln\left(p_{t,out}/p_{t,in}\right)}{\ln\left(T_{t,out}/T_{t,in}\right)} \tag{2.10}$$

- Isentropic efficiency: the ratio between isentropic total enthalpy change and actual total enthalpy change.

$$\eta_{is} = \frac{\Delta h_{t,is}}{\Delta h_t} = \frac{\left(p_{t,out}/p_{t,in}\right)^{\frac{\kappa-1}{\kappa}} - 1}{\left(p_{t,out}/p_{t,in}\right)^{\frac{\kappa-1}{\kappa \cdot \eta}} - 1} \tag{2.11}$$

- Work coefficient: the fraction between total enthalpy change and u_2^2.

$$\tau = \frac{\Delta h_t}{u_2^2} = \frac{c_p\left(T_{t,out} - T_{t,in}\right)}{u_2^2} \tag{2.12}$$

- Head coefficient: the product of polytropic efficiency and work coefficient. The head coefficient is specifically applied for process compressors to evaluate its compression capability and energy consumption in combination.

$$h = \tau \cdot \eta \tag{2.13}$$

For the diffuser part, the following parameters are commonly used to quantify the quality of diffusion:

- Loss coefficient: the ratio between the total pressure loss during the diffusion and the dynamic pressure portion at the diffuser inlet. This parameter can be also used to quantify the aerodynamic performance of other stationary components along the

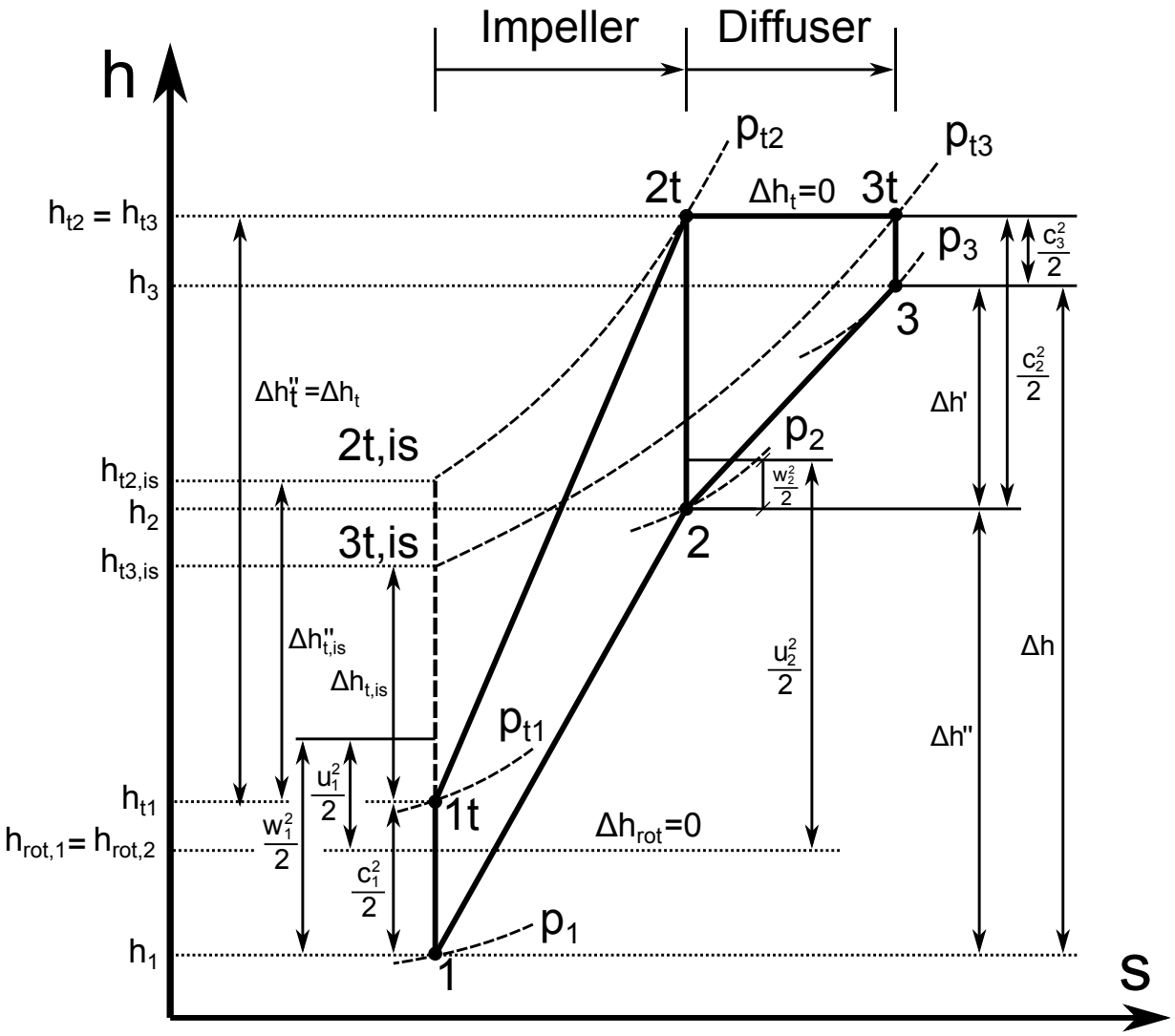

Figure 2.1: h-s diagram of a centrifugal compressor stage; shown are the rotor impeller and the stator according to Lüdtke [60]

compressor stage, such as the IGV plenum for this project (shown later in Figure 3.4).

$$LC = \frac{p_{t,in} - p_{t,out}}{p_{t,in} - p_{s,in}} \tag{2.14}$$

- Recovery factor: the ratio between the static pressure rise achieved by the diffusion and the dynamic pressure portion at the diffuser inlet.

$$C_p = \frac{p_{s,out} - p_{s,in}}{p_{t,in} - p_{s,in}} \tag{2.15}$$

Additionally, in fluid mechanics the following non-dimensional parameters are defined to examine the flow based on its similarity:

- Flow coefficient: the non-dimensional mass flow rate calculated by the volumetric flow rate in relation to the tip diameter and the circumferential velocity at the impeller outlet.

$$\phi = \frac{4\dot{m}}{\rho\pi D^2 u} \tag{2.16}$$

- Circumferential Mach number: the ratio between the circumferential velocity and the local speed of sound.

$$M_u = \frac{u}{\sqrt{\kappa RT}} \tag{2.17}$$

- Axial Mach number: the ratio between the axial velocity and the local speed of sound.

$$M_{ax} = \frac{c_{ax}}{\sqrt{\kappa RT}} \tag{2.18}$$

- Reynolds number: the non-dimensional fluid quantity defined as the ratio between the inertial force and the viscous force.

$$Re = \frac{\rho v d}{\eta} = \frac{v d}{\nu} \tag{2.19}$$

2.2 Centrifugal Compressor Flow Physics

In this section, the flow that passes through a centrifugal compressor stage is briefly discussed by describing the flow patterns in the main stage components, including the impeller, vaneless diffuser and the return channel.

2.2.1 Impeller Flow

Before the flow reaches the impeller, it has often already experienced a velocity acceleration accompanied with a static pressure drop as it travels through the stage inlet components. At the impeller inlet section, the flow will be turned strongly by the blade forces in the circumferential direction, and meanwhile needs to pass through the blade passages following the radially outwards direction. The flow trajectory within the impeller follows a so-called "pseudo-helical" pattern Japikse [55]. Figure 2.2 illustrates the primary flow with simple untwisted blades (a) as well as the changes in the velocity triangles at the impeller leading edge due to different locations at near hub, midspan and near shroud (b). The real flow is simplified here as a two-dimensional flow at meridional sections.

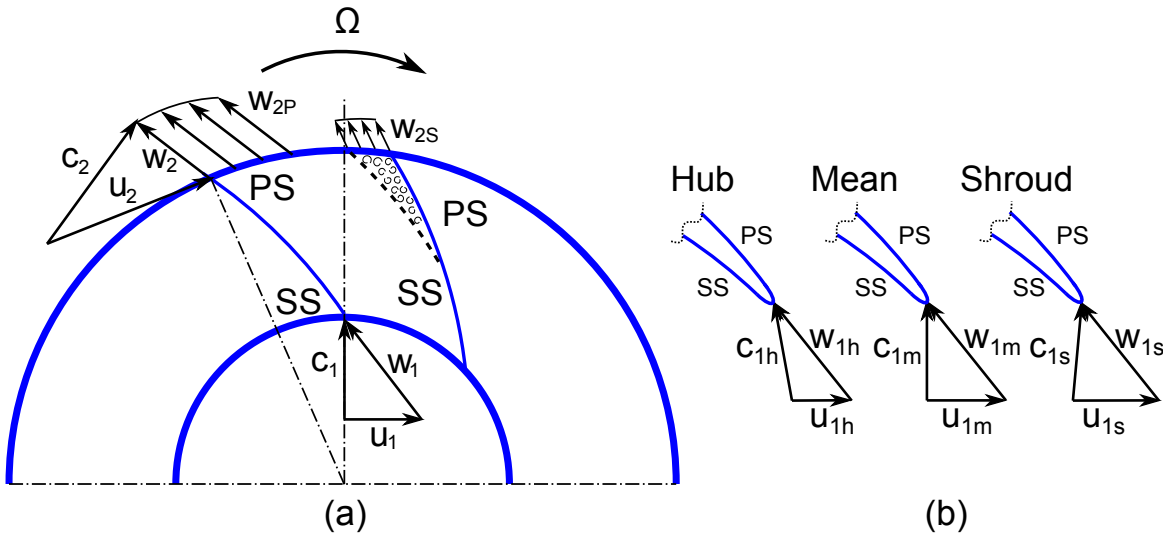

Figure 2.2: Impeller 2D primary flow with inlet and outlet velocities and jet-wake flow from Japikse [55] (a), and the velocity triangles under ideal operation at three spanwise sections from Baskharone [7]
(b).

Between the inlet and outlet the classical two-zone model is drawn by $\boldsymbol{w_{2p}}$ and $\boldsymbol{w_{2s}}$ with different vectors. They are the results of the non-isentropic, secondary flow which leads to the suction-side flow's tendency to depart from the blade surfaces. This secondary flow pattern is referred as a "jet-wake" flow, which was firstly discussed by Dean [25] and Benvenuti [9], and later extensively measured by Eckardt [30]. In these works the jet-wake flow was recognized as a flow momentum deficit near the impeller shroud on the suction side, and at the same time a flow energization near the impeller hub on the pressure side. In Figure 2.3-(b), the three ideal velocity triangles demonstrate that in an ideal operation case, the relative velocity $\boldsymbol{w}$ should match the direction prescribed by the blade camber line direction at the leading edge. Since the circumferential velocity $\boldsymbol{u}$ increases continuously

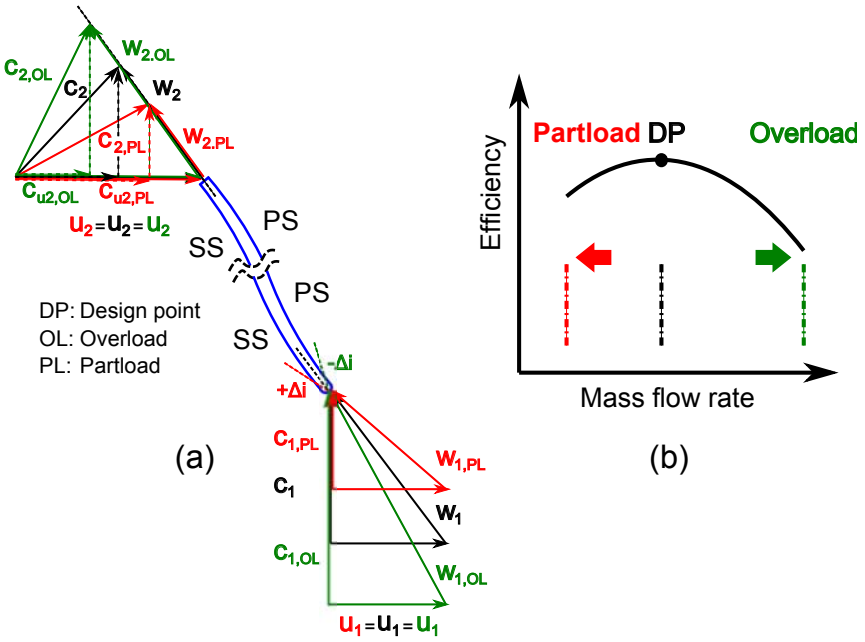

Figure 2.3: Impeller flow with velocity components at inlet and outlet for working at design point (DP) as well as under partload (PL) and overload (OL)

from hub to shroud along with the ever-increasing blade radius, the ideal absolute inlet velocity $\boldsymbol{c_1}$ must be altered accordingly Baskharone [7]. In practical applications, the direction of inlet velocity $\boldsymbol{c}$ can be controlled by adding an additional blade cascade in front of the impeller, for example an IGV stage as discussed in this study.

For a real compressor stage with varying mass flow rates, the inlet velocity triangle has to be deviated from its original direction. To illustrate the effects of mass flow variations in the impeller flow directions, Figure 2.3 presents a sketch of the velocity triangles for the compressor flow at the impeller leading edge and trailing edge (a) due to the changes in the mass flow at its partload and overload (b). The sketch is made with the simplification with an axial inlet flow $\boldsymbol{c_{1,DP}}$ (or called free-of-swirl) at the impeller leading edge at its design point. The relative velocity $\boldsymbol{w_{1,DP}}$, which approaches the blade leading edge, should be ideally aligned to the impeller camber line at leading edge, so that the impeller inducer works best without incidence losses. In an ideal case, the impeller flow should also follow the impeller blade profile perfectly, resulting in a relative velocity at the trailing edge $\boldsymbol{w_2}$ also aligned with the blade direction at the trailing edge.

Now, suppose the mass flow is reduced to the amount at partload, the absolute inlet velocity $\boldsymbol{c_1}$ has to decrease to a smaller value $\boldsymbol{c_{1,PL}}$. Under the same rotating speed $\boldsymbol{u_1}$, the relative inlet velocity $\boldsymbol{w_{1,PL}}$ deviates from the original direction aligned with the blade camber line, which leads to a positive incidence increase $+\Delta i$. This incidence angle has

a tendency to cause the flow to leave from the blade suction-side surface, and thus may induce a suction-side flow separation. Assume that despite of the incidence deviation at the leading edge, the impeller flow eventually still follows the blade profile, the relative outlet velocity $\boldsymbol{w_{2,PL}}$ then only reduces its magnitude without changing its direction. This change in the $\boldsymbol{w_{2,PL}}$, in combination with the constant $\boldsymbol{u_2}$, will cause the absolute outlet velocity $\boldsymbol{c_{2,PL}}$ to be turned towards the tangential direction, resulting in a larger magnitude of $\boldsymbol{c_{u2,PL}}$ as illustrated in Figure 2.3 at the impeller trailing edge.

Next, if the impeller works at overload with an excessive mass flow rate, the larger $\boldsymbol{c_{1,OL}}$ leads to a negative incidence deviation $-\Delta i$, which gives the impeller flow a tendency for a pressure-side flow separation. As a consequence, the velocity triangle at the impeller trailing edge will transform into a larger and steeper shape, with the absolute velocity $\boldsymbol{c_{2,OL}}$ turned towards the radial direction.

It should be emphasized that in Figure 2.3 the impeller flow is only examined based on the primary flow pattern. The real flow at the impeller trailing edge may still contain other possible secondary flow effects, such as the jet-wake flow as discussed in the previous session, the possible flow separation in the blade passages, the possible leakage flow due to cavities, and boundary layer flow causing slips at impeller trailing edge (Cumpsty [22]). These secondary flow factors also impact the real impeller flow to be more complicated than what is shown here in Figure 2.3.

While the impeller flow is proceeding through the blade passages, the total pressure rise realized by the impeller can be roughly calculated from Japikse [55] as:

$$\Pi_t = \left(1 + (\kappa - 1)\eta\tau M_u^2\right)^{\frac{\kappa}{\kappa-1}} \tag{2.20}$$

$$= 1 + \kappa\eta\tau M_u^2 + O(M_u^4) + \sum_{n=6} O(M_u^n) \tag{2.21}$$

while the real flow effects such as disk friction, the cavity leakage and recirculation are neglected. Therefore, the total pressure ratio Π_t obtained by a centrifugal compressor is a function of specific heat ratio κ, impeller efficiency η, impeller work coefficient τ and machine Mach number Mu. Among these parameters, the impeller work coefficient τ is directly correlated to the c_{u2} and c_{u1} as shown previously in Equation 2.6 and 2.12, in which c_{u1} is further directly influenced by a pre-swirl or counter-swirl created by IGVs. Therefore, an existing IGV stage has great impact on the total pressure ratio obtained by the compression.

2.2.2 Diffuser Flow

As the flow arrives at the diffuser, it often reaches a high velocity level, which is achieved by the strong rotation at the impeller trailing edge as well as the flow acceleration throughout the blade passages. Thus a diffuser is applied to convert this portion of kinetic energy into further pressure rise. A diffuser often has two forms: vaneless diffuser and vaned diffuser. Compared to a vaned diffuser of similar scale, a vaneless diffuser offers a wider operation range since it does not contain a throat subject to earlier choke at an overload operation. Therefore, a vaneless diffuser is mainly applied in process compressors and turbochargers where the mass flow rates greatly vary due to large variations of operation modes.

Figure 2.4 illustrates the geometry of a vaneless diffuser. This diffuser is comprised of two parallel walls, which circumscribe a radial annulus space with a constant width b. For a simplified, incompressible fluid, the flow trajectory should follow a logarithmic spiral Japikse [55]. This is because the diffuser flow is constrained by the conservation of angular momentum ($r \cdot c_u = \text{constant}$). Thus from the diffuser inlet to the outlet with in response of an ever-increasing radius r, the circumferential velocity c_u should decrease proportionally. Meanwhile, based on the conservation of mass, the meridional velocity c_m should decrease due to the ever-increasing cross section $A = 2\pi rb$:

$$r \cdot c_u = const. \tag{2.22}$$

$$\rho \cdot c_m \cdot 2\pi rb = \dot{m} = const. \tag{2.23}$$

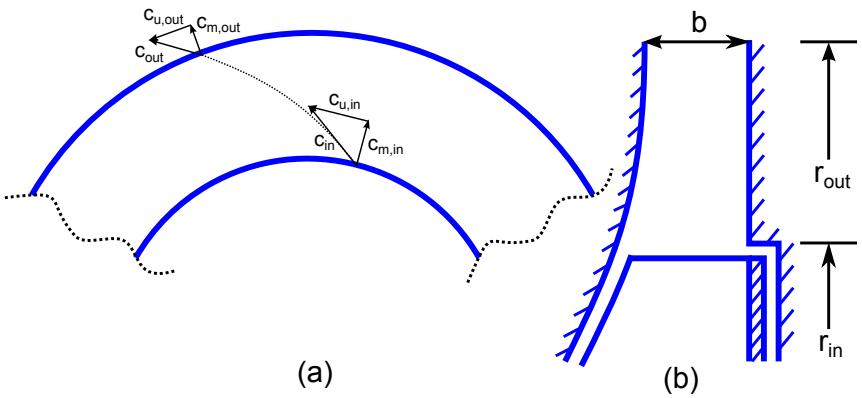

Figure 2.4: Flow in the vaneless diffuser with velocity components at the diffuser inlet and outlet (a) and sketch of a diffuser together with the impeller outlet (b)

These two equations govern the diffuser flow angle between the meridional and the circumferential velocities:

$$\tan\alpha = \frac{c_u}{c_m} = \frac{C_1/r}{\dot{m}/(\rho \cdot 2\pi r b)} = C_2 \cdot \frac{\rho b}{\dot{m}} \tag{2.24}$$

Therefore, for an incompressible flow in a vaneless diffuser, the diffuser flow angle should remain constant. This is known as the logarithmic law as the ideal flow for vaneless diffuser.

In reality, a vaneless diffuser flow deviates from the logarithmic spiral when it is subjected to other secondary flow effects, such as wall friction, vortex shedding from the impeller, boundary layer flow and even reversed flow due to strong adversed pressure gradients, as well as flow leakage and local pinch steps between the impeller hub and the diffuser hub. In addition, for a non-adiabatic diffuser with $\dot{q} \neq const$, a certain portion of heat will be lost by heat conduction through the diffuser walls, resulting in a lower state of total energy at the diffuser outlet compared to the diffuser inlet.

2.2.3 U-Bend and Return Channel Flow

For a typical centrifugal compressor such as process compressor, the downstream components mainly include a U-bend, a return channel (mostly with static vanes inside), and a stage outlet. The downstream components are responsible for the main task to guide the flow back from radial to axial to be ready for the next stage while eliminating the strong swirling effects still existing after the flow passes the diffuser. It should also avoid inducing additional flow losses in order to maintain the total pressure level already achieved. Therefore, the studies on the U-bend and return channel often involve the reduction of pressure losses by the applications of e.g. truncated diffuser and U-bend with new static vanes (deswirler) Kunte [58], Wilkosz [89] and Schmidt [70], improved return channel geometry Hildebrandt [49], Aubry [5] and De Bellis [24], flow control for the return channel Simpson [76], and new aerodynamic designs as the return channel vanes Aalburg [1] and Franz [33].

2.3 Inlet Guide Vane Design

From the previous discussion, it becomes clear that without IGV the flow direction at the impeller leading edge has to be changed at partload and overload, which in turn deteriorates the performance of compression. By introducing an additional IGV stage,

the incidence deviation can be greatly recovered. This section further discusses the inlet guide vane design including its working principle, type of swirl, aerodynamic design and mechanical design for its affiliated components.

2.3.1 Working Principle

The working principle of IGV can be explained using the velocity triangles as shown in Figure 2.5. The conditions for the compressor discussed here include constant rotating speed $\boldsymbol{u}$ and initially zero incidence at design point ($\boldsymbol{c} = c_{ax}$). Suppose that the impeller is working at partload without IGV, the absolute velocity $\boldsymbol{c}$ keeps its direction but with a shortened magnitude. This leads to the relative velocity $\boldsymbol{w}$ turned towards the pressure side. Under such condition ($i > 0$), the flow at the leading edge has a tendency to leave from the suction-side blade surface, which may further progress a suction-side flow separation. For a centrifugal compressor in practice, a suction-side flow separation is often a precursor for surge and thus should be prevented. With the IGVs installed, the absolute velocity $\boldsymbol{c}$ can be turned back to the positive direction in respect to $\boldsymbol{u}$, which leads to a positive velocity component c_u represented as a pre-swirl. With a correct magnitude of c_u, this positive $\boldsymbol{w}$ will be just to keep the relative flow velocity $\boldsymbol{w}$ still aligned to the blade the camber line so the incidence is kept at 0.

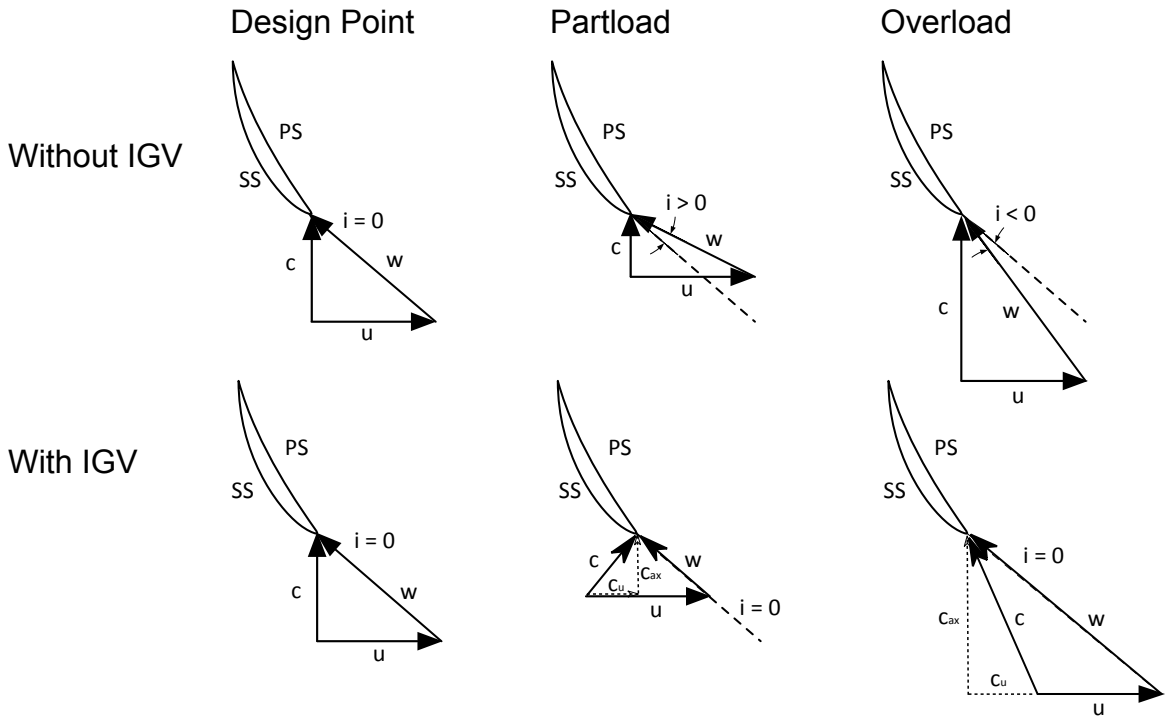

Figure 2.5: Working principle of inlet guide vanes

In contrast, if the impeller works at overload, the magnitude of $\boldsymbol{c}$ has to be enlarged, resulting in the relative velocity $\boldsymbol{w}$ turned towards the blade suction side. This negative incidence ($i < 0$) has a tendency to induce pressure-side flow separation. With IGV installed, a proper negative swirl called counter-swirl, will be utilized to correct the flow direction of $\boldsymbol{w}$ to be aligned at zero incidence again.

In practice, for a compressor stage at large variations of mass flow rates, the amount of counter- or pre-swirl provided by one particular IGV setting angle may not perfectly match the level of change in $\boldsymbol{c}$, which will lead to certain incidence deviations. As long as the incidence deviation is small, the impeller leading edge may be still able to tolerate with it. This tolerance within certain incidence range can be best expressed by a "bathtub" chart as shown in Figure 2.6 from Saravanamuttoo [69], which shows the relationship between total pressure losses and incidence angle (called stagnation loss). The stagnation loss is defined as:

$$s_l = \frac{p_{t1} - p_{t2}}{\frac{1}{2}\rho c_1^2} \tag{2.25}$$

and the angle deflection ϵ is defined as:

$$\epsilon = \alpha_1 - \alpha_2 \tag{2.26}$$

in which 1 and 2 are impeller inlet and outlet stations. The bathtub chart shows that the incidence should be kept within the flat portion of the stagnation loss curve.

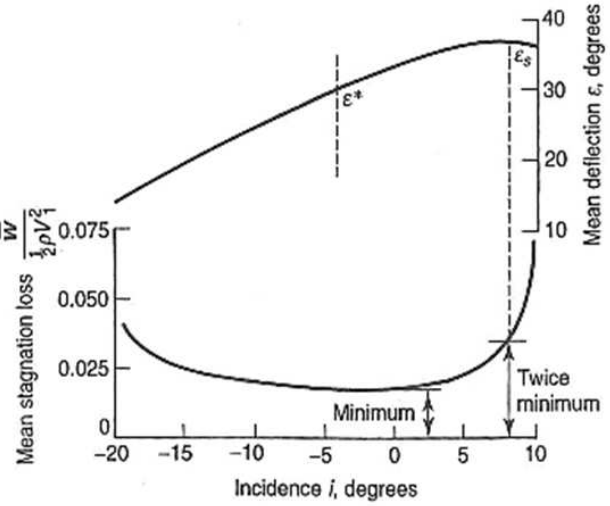

Figure 2.6: Stagnation loss and flow direction deflection in relation to the incidence from Saravanamuttoo [69]

2.3.2 Type of Swirl

A pre-swirl or counter-swirl created by IGVs can be quantified by its magnitude of circumferential velocity component in the whole flow field. In general, it can be described as:

$$c_u = \frac{A}{r} + B + C \cdot r + D \cdot r^2 \tag{2.27}$$

in which r is the radius and A-D are constants of the manitudes corresponding to the different types of swirl. For this study, one IGV type can only induce one certain pattern of swirl. Thus the c_u distribution can be simplified as:

$$c_u = E \cdot r^n \tag{2.28}$$

the index n denotes the various types of swirl such as:

- $n = -1$: inverse swirl;
- $n = 0$: constant swirl;
- $n = 1$: linear swirl;
- $n = 2$: quadratic swirl.

as illustrated in Figure 2.7.

Steinke [79] further analyzed the impacts of the four swirl types on a blade cascade by simplified CFD code. The main findings are summarized in Figure 2.8. Firstly, on the left, the impacts of four different swirl types were depicted as the changes of incidence angle in the radial direction at one particular IGV setting angle (30°) when the blade tip has zero incidence. The four curves for each type of swirl show that the inverse swirl ($n = -1$) and the constant swirl ($n = 0$) have increased incidence deviations from blade tip to blade hub.

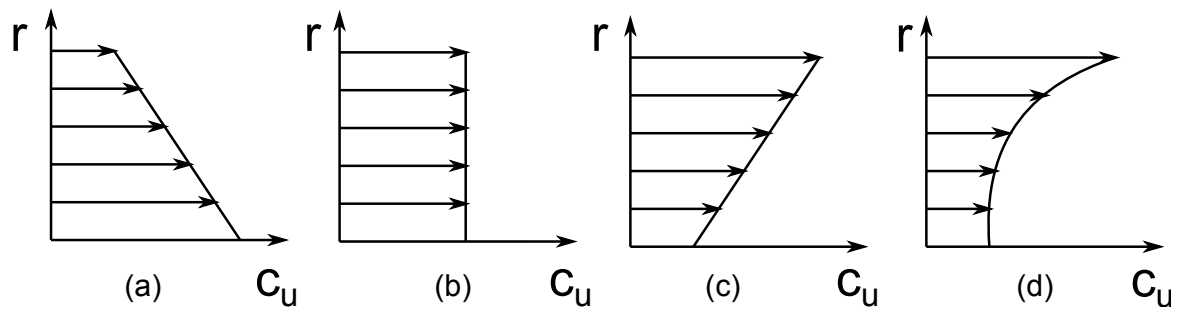

Figure 2.7: Type of swirl: (a) inverse swirl; (b) constant swirl; (c) linear swirl; (d) quadratic swirl

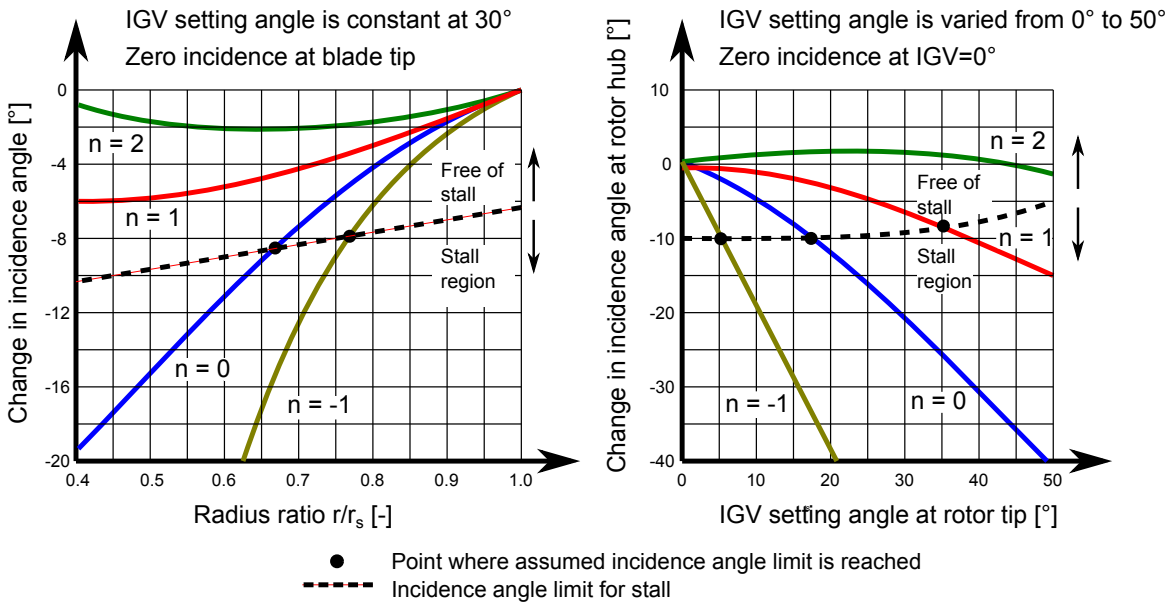

Figure 2.8: Change of incidence angle for the four types of swirl from Steinke [79]

In contrast, the linear swirl ($n = 1$) has only a restrained growth in the deviation, and the quadratic swirl ($n = 2$) even delivers an incidence recovery starting from the midspan to the hub. The dashed line denotes the limit of the maximum tolerable incidence change for the blade until a stall shows up. This limit line divides the whole chart into a stall-free region (above the limit) and a stalled region (below the limit). Thus the inverse swirl (n = -1) and constant swirl (n = 0) have certain parts across the stalled region, while the constant swirl (n = 1) and quadratic swirl (n = 2) always stay in the stall-free region, and thus are beneficial to prevent stall.

Secondly on the right, for the four swirl types all starting from zero-incidence at IGV = 0°, the changes of incidence at the rotor hub are displayed in relation to the increase of IGV setting angle measured at the rotor tip. The black dashed curve as the limit denotes the maximum IGV setting angle at which a stall firstly occurs at the rotor hub. It again divides the whole area into a safe region (above) and a stalled region (below). As the IGV setting angle increases from 0°, the inverse swirl firstly reaches the maximum tolerable incidence (5°), then follows the constant swirl (18°). The constant swirl reaches the limit subsequently (35°), and finally the quadratic swirl (44°). In summary, the results indicate that merely from the aspect of preventing stall on the blade, the preference for choosing the type of swirl should be: quadratic swirl > linear swirl > constant swirl > inverse swirl

Based on these findings, the inverse swirl and the constant swirl should be avoided in piratical use. In addition, in reality in order to obtain a real quadratic swirl (n = 2), the IGV blade needs to be severely leaned along the spanwise direction, which is much

more difficult to be manufactured than a simple straight blade. On the other hand, the previous Figure 2.2-(b) indicates that a $c_u \propto r$ is beneficial for keeping the correct inlet flow direction. For these reasons, the linear swirl (n = 1) has become the standard choice for the later development of IGV design.

2.3.3 Aerodynamic Design

In the early time period, an inlet guide vane was merely a flat plate mounted on an annulus apparatus. An example has shown in Figure 2.9 from Coppinger [19]. Its poor aerodynamic performance has caused by its bad flow guidance, large tip clearance to the casing at larger angle settings, and strong flow non-uniformity between the outer flow region and the internal core. Later more advanced blade shapes were put into practice, and the vane geometry has evolved into symmetric, uncambered profiles such as Rodgers [68] and Ishino [53]. For uncambered IGV, the IGV profile was a standard NACA profile whose aerodynamic behavior was extensively tested earlier by Abbott [3]. Later, the asymmetric cambered profiles appeared in Gelder [37], Tetu [83]. A summary on the early IGV geometry development until the 21st century can be found in Whitfield [85].

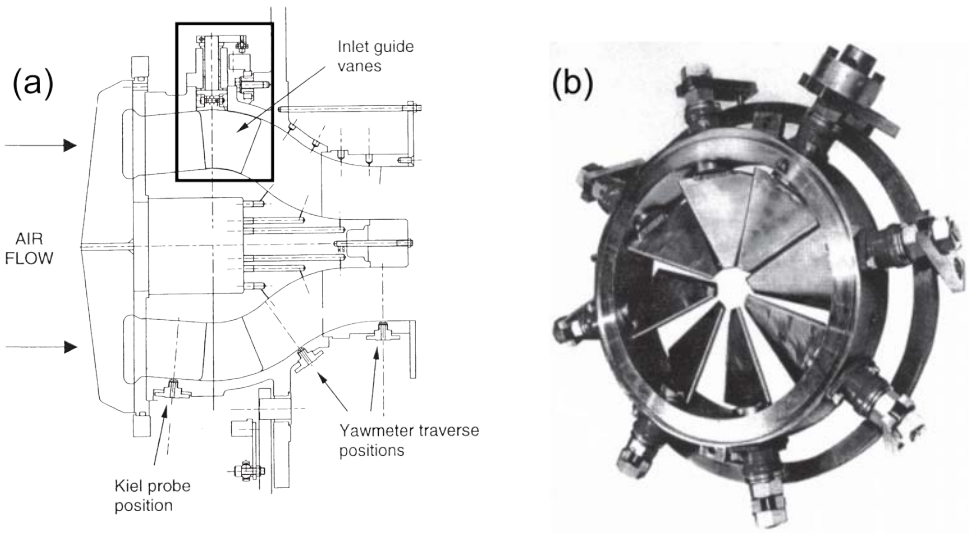

Figure 2.9: An early IGV system (a) and its mechanical assembly (b) from Coppinger [19]

In the last decades, more sophisticated IGV profiles have been developed with the assistance of CFD simulation techniques, which facilitates a quick turn-around by iterative optimization during design phase. For example, Coppinger [19] used CFD simulations to obtain a new tandem profile, which demonstrated improved aerodynamics in comparison with the conventional flat-plate IGV. Figure 2.10 shows the mesh model of tandem IGV (a) and the absolute velocity contours of the two IGV types at a high IGV setting angle

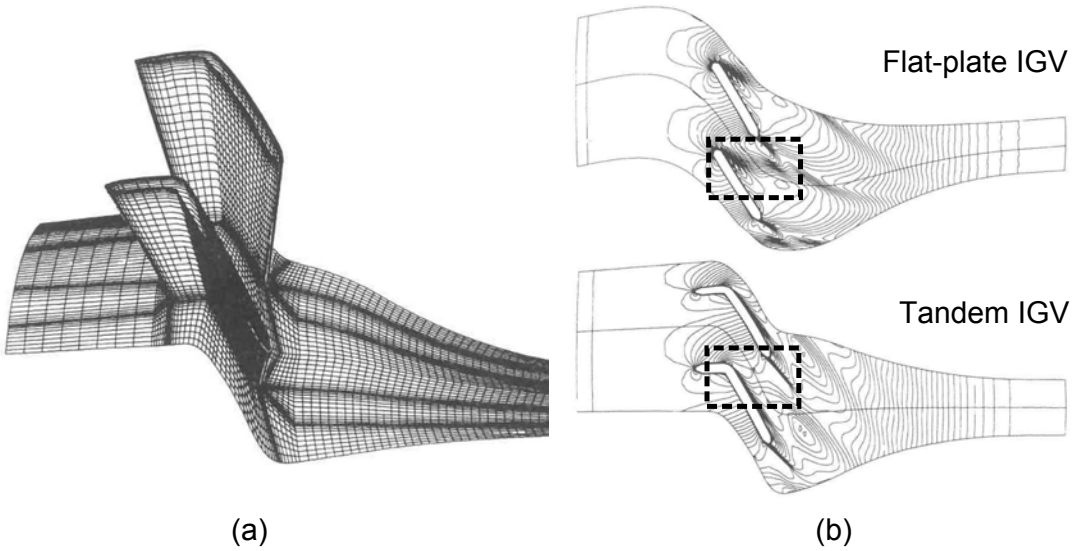

Figure 2.10: Mesh model of a tandem IGV (a) and comparison of absolute velocity contours between the flat-plate IGV and the tandem IGV (b) from Coppinger [20]

(b). It can be seen that the tandem IGV largely suppresses the flow separation which is dominant on the suction-side blade surface for the flat-plate IGV case. The benefit is mainly ascribed to the tandem shape which provides better flow guidance. This tandem IGV can be considered as the predecessor for the later flapped IGV shape seen as discussed by Boehle [14] and Hobson [52].

Besides the classical airfoil shapes, more recently there is a "circulation control" starting to draw attention. An introduction for this IGV type can be found in Hill [50] and Gunter [44]. In general, the airfoil with flow control utilizes a Coanda jet emitted towards the IGV trailing edge, which is designed to enhance the circulation level around the airfoil which is able to detain flow separation further downstream towards the trailing edge.

Figure 2.11 shows the four major aerodynamic designs for IGVs. They are symmetric, uncambered airfoil (a); asymmetric, cambered airfoil (b); multi-foil with flapped tail (c); airfoil with circulation control (d). No matter what specific geometry is applied, the aerodynamic design for an IGV stage should fulfill the following requirements that: (1) A large operation range and a good flow guidance, especially at high IGV setting angles; (2) Small incidence losses and small pressure losses; (3) Proper pre-swirl levels for the impeller inlet; (4) Reduced flow non-uniformity at the impeller inlet; (5) Minimum negative impacts concerning its integration with other associated components.

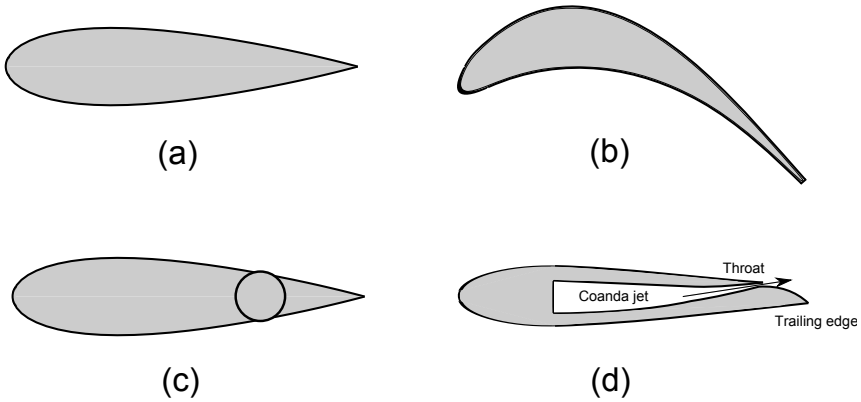

Figure 2.11: Four major aerodynamic IGV designs: (a) symmetric, uncambered airfoil; (b) asymmetric, cambered airfoil; (c) multi-foil with flapped tail (d) airfoil with circulation control

2.3.4 Mechanical Design

During the design phase of IGV, another important consideration is how to integrate them into real components. The previous Figure 2.9 already shows a common and simple mechanical assembly, including a cylindrical section and a vane cascade anchored by an external linkage. However, its empty core region usually became a major source of flow non-uniformity, because the axial jet is allowed to directly enter the impeller Coppinger [20].

Nowadays, complex mechanical systems have been applied as the adjustment mechanism for the IGVs. Figure 2.12 shows such an advanced IGV mechanical design in detail. This IGV assembly has three parts: IGV blades, internal gears and an actuator linked with a control rod. The control rod is to connect the gears with the actuator, and transfers the linear movement of the actuator into rotational movement of the gears. The friction and the spacing in the gears and actuator, as well as between the IGVs and the plenum walls need to be carefully examined to avoid unacceptable deviations between desired and actual IGV positions.

Figure 2.13 presents another modern IGV mechanical systems from Hensges [48], which is actually very similar to the real mechanical design adopted by this study. It comprises of a lever-type control mechanism driven by an actuator. By moving the drive ring and the lever to which all IGVs are linked, all IGVs can be accurately adjusted at the same time to the a desired angular position. To ensure a good contact between the driving ring and the IGV carrier, some spring-loaded sliding elements are in-pair arranged to support the drive ring. All IGVs use pivot bearings inside the carrier to allow a smooth rotating motion, and are contained inside a cover disc which is used to damp the vibrations induced by the

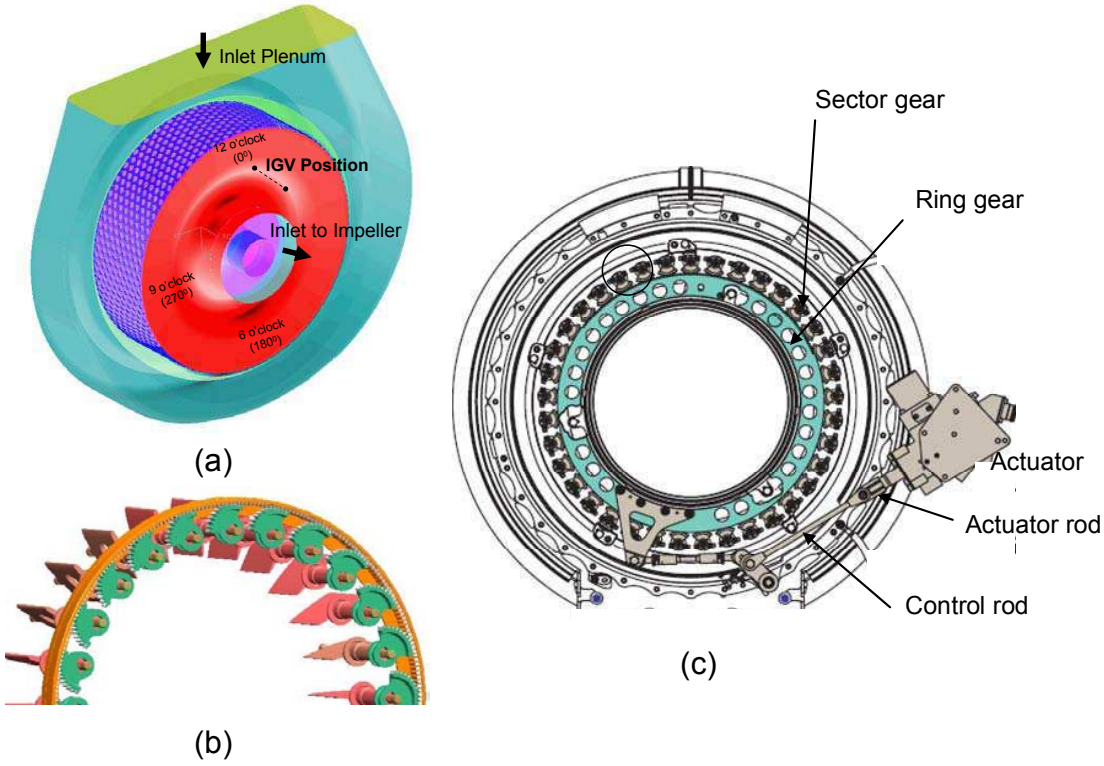

Figure 2.12: IGV plenum (a) with its gear-system (b) and assembly (c) from Duong [28]

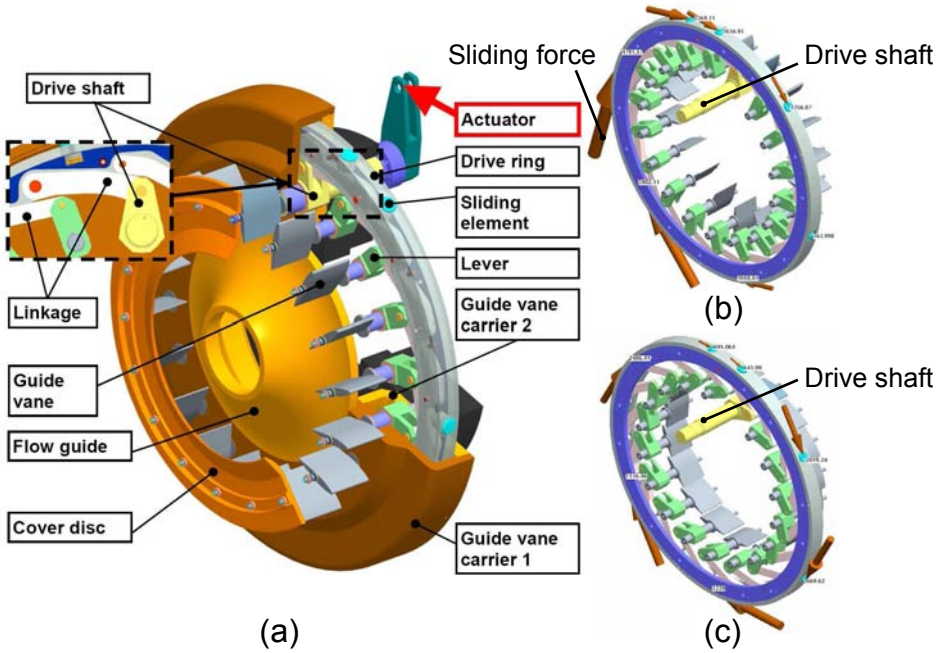

Figure 2.13: IGV mechanical system (a) with the IGV setting position at 0° (b) and maximum setting limit (c) from Hensges [48]

flow-structure interactions.

Regarding the practical issues associated with this type of mechanical assembly, McAlpin [62] summarized the possible failure modes such as cracking or seizing caused by corrosion, wear losses in bushings which causes loose contact and cyclic bending loads, high local contact stresses on the load bearing surfaces, and high-cycle fatigue cracking. In addition, since the IGV stage is located closely to the compressor, the flow-structure interactions may be induced due to vortex shedding propagating from the IGV stage downstream to the compressor blades, and thus should be taken into consideration for the IGV mechanical design. Some studies on this topic can be found in Bailie [6], Duong [28] and Hensges [48].

Chapter 3

Experimental Investigation

This chapter presents the complete IGV test campaign on the rotating test rig at LFA-TUM with a total of three IGV configurations, including a baseline IGV design with NACA profile, a unique-cambered IGV design, and a multi-foil IGV design. First of all, the test facility and the centrifugal compressor stage are introduced, followed by the instrumentation setup and the measurement accuracy. Secondly, the procedure of the test campaign is briefly described. As the main part of this chapter, the discussion of test results covers the steady measurement results for the stage performance tests, and the dynamic measurement results obtained from the surge tests. For the stage performance tests, the compressor stage with the IGVs installed is firstly analyzed separately at each component positions (IGV plenum, impeller, diffuser, return channel, and stage outlet), and then combined together to examine the overall stage performance. After that, the stage dynamic behavior is discussed based on the dynamic pressure data in the time and frequency domains. A brief summary for the whole test campaign is presented in the end.

3.1 Test Facility

The IGV test campaign was carried out on the TUM-GE highspeed centrifugal compressor test rig. The test rig was built-up in collaborative efforts to facilitate the research and development projects utilizing the full-scale rotating facility. The test rig contains an open-loop, single-stage configuration with ambient flow conditions at the stage inlet. The distance between the frontal and rear assembly walls allows for a quick adjustment for different test configurations. Figure 3.1 gives an overview of the test rig from Lang [59]. The test facility can be grouped into four major units: driving unit, control unit, test bench and data acquisition unit.

The driving unit includes a pair of electrical motors, a gearbox, a rotor cartridge and

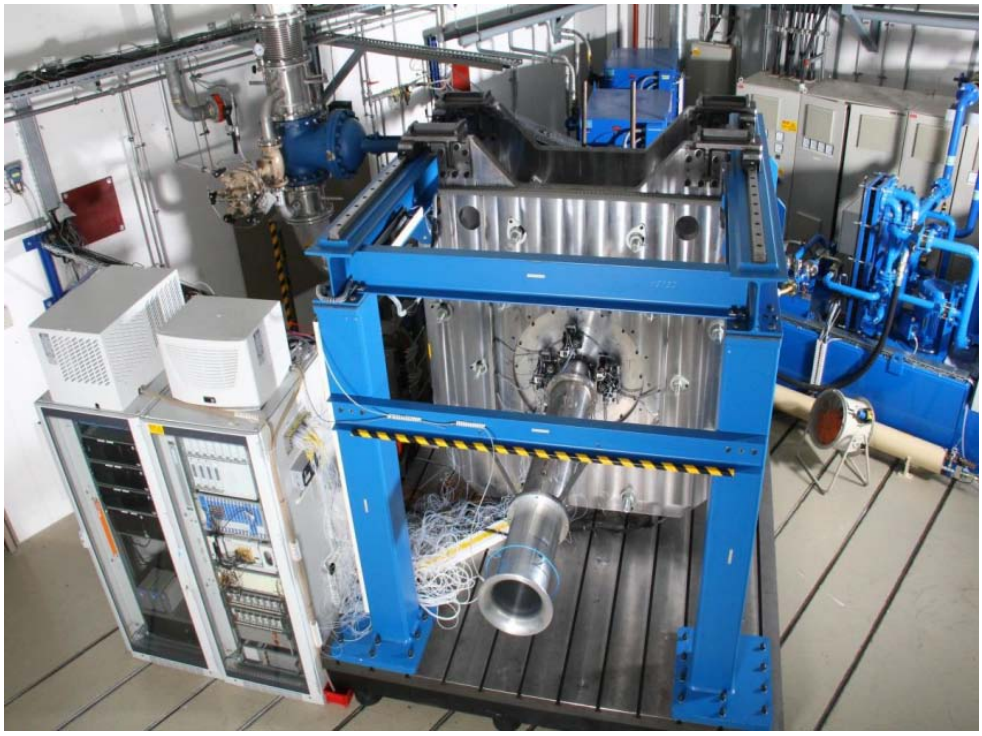

Figure 3.1: TUM-LFA centrifugal compressor test facility from Lang [59]

lubrication oil system. The two electrical motors are coupled in a master-slave mode to generate a maximum power of 800 kW. The shaft power is then transmitted through the 1:10 gearbox and the rotor cartridge to drive the overhang-mounted centrifugal compressor to reach a maximum speed of 30,000 rpm.

The control unit has three throttling valves: a main valve, a bypass valve, an anti-surge valve for emergency situations. The three valves are located downstream of the exhaust volute to control the mass flow rate of the working fluid. During each test, the flow rate can be either adjusted by the main valve or fine-tunned by the bypass valve. If the compressor stage is in danger of surge, the anti-surge valve can be automatically triggered to recover the flow rate immediately back to 100% opening. This is to prevent the compressor stage falling into deep surge cycles, which may damage the facility by imposing large periodic loadings and vibrations on the shaft. The anti-surge valve can be also manually triggered by the operator.

The test bench contains the whole compressor stage supported by a robust steel base and two vertical steel walls. Figure 3.2 shows a schematic sketch of the layout of the test bench for the IGV test campaign. This layout for the IGV is different from Figure 3.1 in that it contains an extra IGV plenum in front of the centrifugal compressor. In addition, before the flow enters the IGV plenum, it has to pass through a long vertical inlet pipe with a

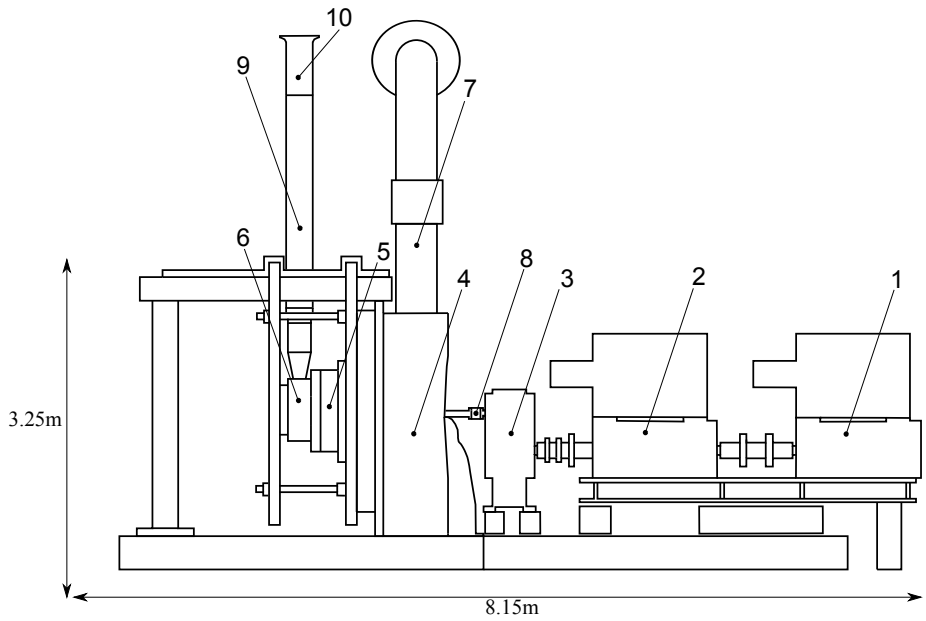

1	Motor 1 (400 kW)	6	IGV plenum
2	Motor 2 (400 kW)	7	Exhaust piping
3	Gearbox	8	Torque meter
4	Volute	9	Inlet piping
5	Compressor stage	10	Inlet venturi

Figure 3.2: Schematic sketch of the stage layout for the IGV rotating test

large L/D ratio to obtain homogeneous conditions.

The data acquisition unit contains several instrument devices, which are applied for e.g. machine monitoring, signal acquisition and data recording. For the IGV test campaign, the data acquisition systems are mainly: (1) Machine monitoring: Bentley Nevada® and NI-PXI® ; (2) Pressure measurement: Scanivalve DSA® and Agilent® ; (3) Temperature measurement: TemPoint® and Agilent® ;(4) Dynamic pressure measurement and surge detection: IfTA® and NI-PXI® . Several critical signals, such as the rotating shaft speed, the bearing vibrations, and dynamic pressure, are redundantly recorded by at least two systems independently.

3.2 Stage Components

The centrifugal compressor stage applied in this IGV study is an industrial process compressor used for Oil & Gas industry, which is described more in detail by Lüdtke [60] and Bloch [11]. Figure 3.3 shows a cross-section view of the complete stage including the IGV plenum, the compressor stage and the measurement positions, which are:

- Section 0: Stage inlet / IGV plenum inlet;

- Section 10: IGV plenum outlet / impeller inlet;
- Section 20: Impeller outlet / diffuser inlet;
- Section 40: Diffuser outlet / U-bend inlet;
- Section 41: U-bend top position;
- Section 41-60: Return channel (with static vanes inside, not shown);
- Section 60: Stage outlet.

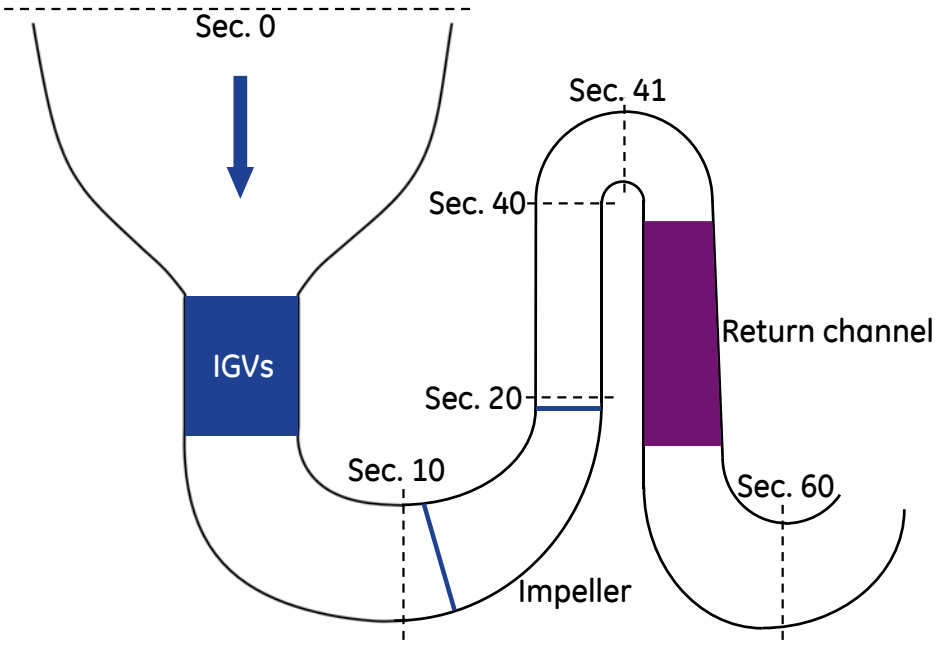

Figure 3.3: Cross-section view of the centrifugal compressor stage for the IGV rotating test

Figure 3.4 shows the real IGV plenum applied for this project and a similar impeller from Guidotti [43]. As the key components the IGV plenum and the impeller will be shortly described in the next session. More details on other affiliated stage components can be found in Aalburg [2], Bonaiuti [15] and Svensdotter [80].

3.2.1 IGV Plenum and IGV Blades

The IGV plenum is a radial plenum typically designed to guide the flow from the radial into the axial direction before the flow arrives at the impeller inlet (Luedtke [60]). For this project, the impeller inlet section overlaps with the IGV plenum exit section. The

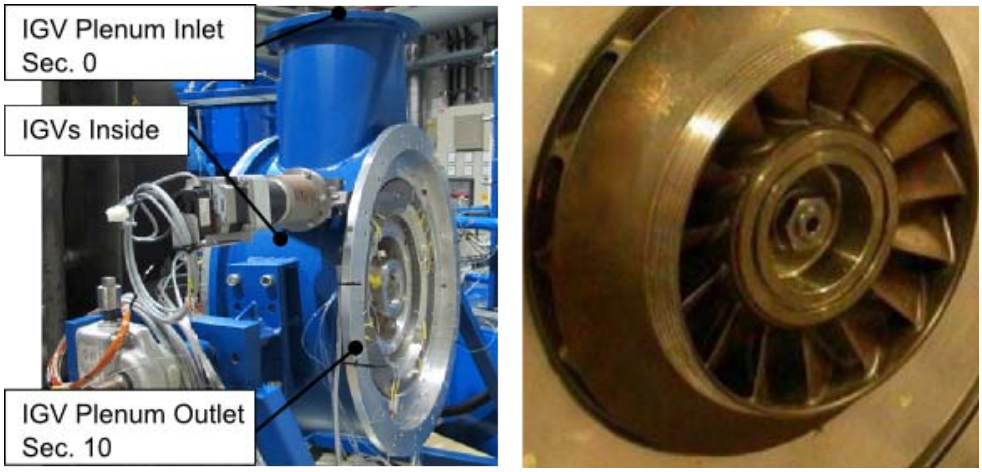

Figure 3.4: IGV plenum for the rotating test (left) and the impeller (right) from Guidotti [43]

main task for the IGV plenum is to provide a flow with desired pre- or counter-swirl for the impeller while maintaining the pressure losses to a minimum. A special feature of this radial plenum is that the flow for the IGVs at each circumferential position is quite non-uniform, because the flow entering the IGV plenum firstly need to pass over different distances before arriving at each IGV position. To visualize this, Figure 3.5 shows the CFD results of static entropy distributions for the IGV plenum with the standard baseline IGVs installed. At IGV = 0°, the inlet flow is symmetric between the left half and the right half. However at IGV = 60°, when the IGV blades are turned into one common direction, the flow becomes very asymmetric by comparing it between the left half and the right half. For the IGVs on the left half, the entering flow has to travel 180° to 360° until arriving at the left portion, resulting in larger entropy generation e.g. at the regions between 10 to 11 o'clock on the left half. It can be seen from the CFD results that in order to counter the circumferential flow non-uniformity, the IGVs located on the left half should be cambered more progressively.

Based on this finding, a total of three IGV types have been proposed as presented in Figure 3.6, in which the three IGVs are referred to as type-A, type-B and type-C. Type-A has a standard, symmetric NACA profile, which serves as the baseline to be compared with the other two types. Type-B contains an unique cambered profile. Its concave surface side facilitates the production of pre-swirl in the positive IGV setting angle range. However, the flow would impinge the convex side, which might further lead to flow losses and early separation at the negative IGV setting angle range. The last version, type-C, features a multi-foil with a fixed front part and a rotating tail. The rotating tail can be turned to a large extent of +/- 60°, which facilitates the flow guidance in a similar manner at both positive and negative IGV setting angles. In addition to the advanced blade profiles,

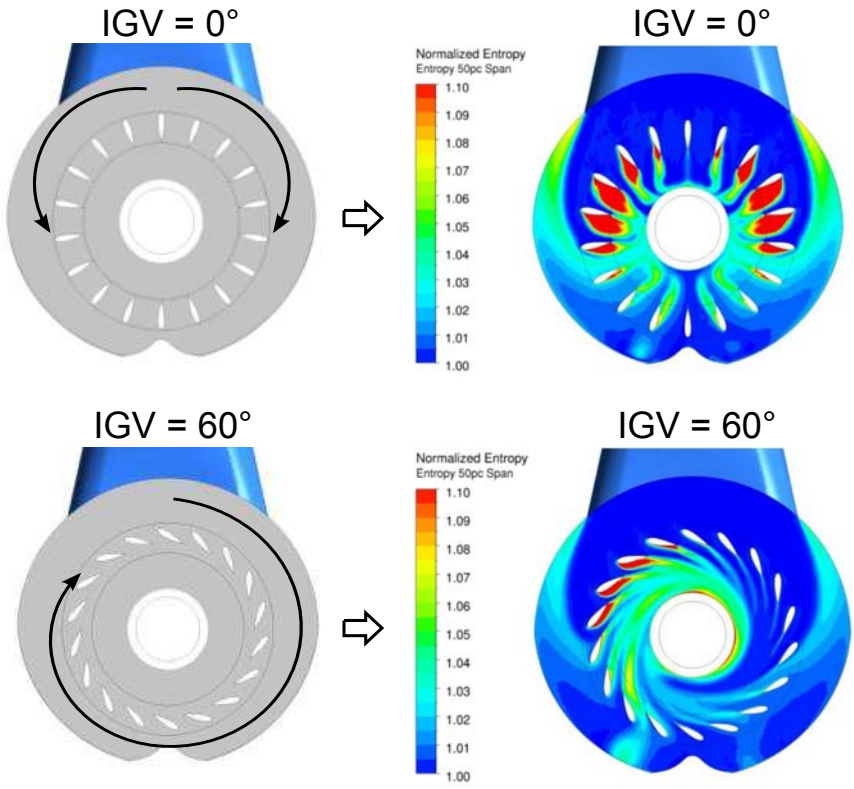

Figure 3.5: IGV plenum with symmetric IGVs (left), and contours of CFD predicted static entropy at IGV = 0° and 60° (right)

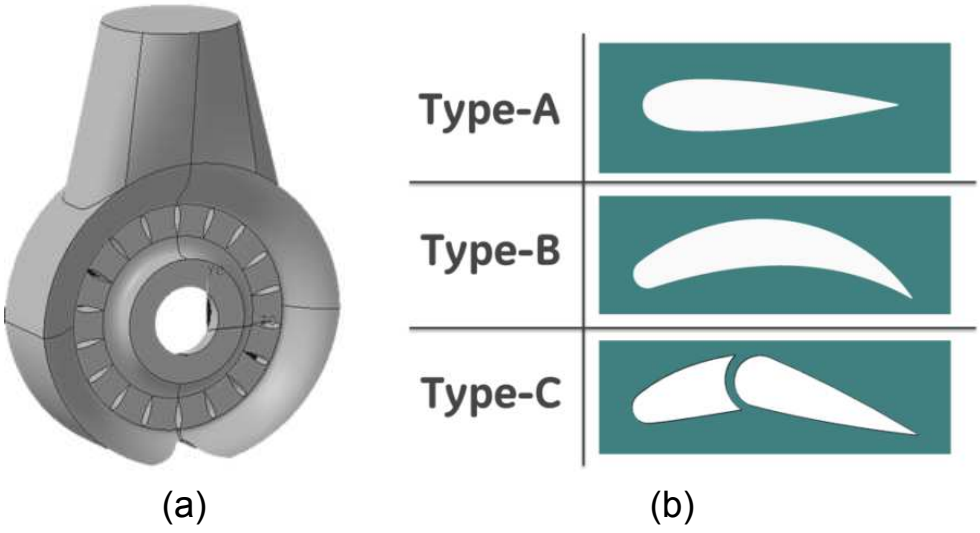

Figure 3.6: The IGV plenum (a) and the three IGV types applied for this project (b); shown are type-A (NACA baseline), type-B (unique cambered) and type-C (multi-foil)

type-B and type-C also contain distinct airfoil shapes at each individual position. This design feature aims at reducing the negative impact of flow non-uniformity as shown in Figure 3.5 using standard IGVs.

3.2.2 Impeller

The impeller used for the IGV project is a shrouded industrial process compressor applied in process industry, which features three dimensional blade geometries to achieve high efficiency over a wide operation range. The impeller is a backswept radial compressor with relative outlet angle $\beta_{20} > 90°$ which faciliates an linearly increasing head with reduced mass flow Boyce [17] and Dixon [27]. The main impeller parameters are shown in Table 3.1.

Table 3.1: Main parameters of the impeller applied for the IGV test campaign

Number of impeller blades	17
Design flow coefficient ϕ	0.1273
Design rotational Mach number M_u	0.73

3.3 Instrumentation Setup

The instrumentation setup includes the layout of all aero- and thermo-sensors located at the measurement sections from the stage inlet to the stage outlet. An overview of instrumentation for the IGV test campaign is listed in Table 3.2.

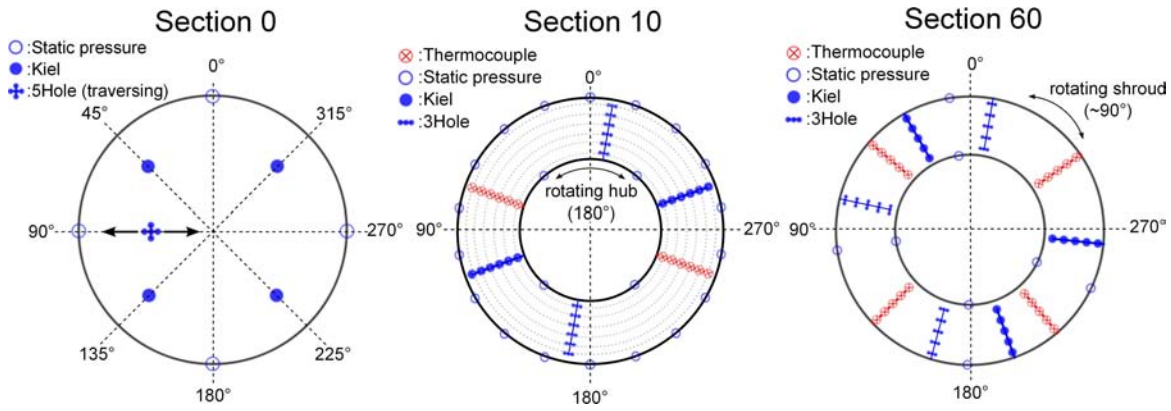

Figure 3.7: Instrumentation at section 0 (left), section 10 (middle), and section 60 (right)

To better illustrate the instrumentation layout, Figure 3.7 shows the cross-section views of the measurement positions at the stage inlet (section 0), impeller inlet and plenum outlet (section 10) and the stage outlet (section 60).

Section 0: The total pressure, static pressure, and flow direction are measured by Kiel probes, static pressure taps and a traversing 5-hole probe. The total temperature is measured by a thermometer (type: PT-100) in the vicinity of the inlet venturi (not shown)

Table 3.2: Instrumentation setup applied for the IGV rotating test campaign

Section	Total Pressure	Static Pressure	Total Temperature	Flow Velocity / Direction	Pressure Fluctuation
0	Kiel	Wall	-	5-hole	-
	1Probe x 4Rake	Taps	-	Traverse x 1	-
10	Kiel	Wall	TC-J	3-hole	PCB
	6Probe x 2Rake	Taps	6Probe x 2Rake	6Probe x 2Rake	x 2
20	Kiel	Wall	TC-J	5-hole	PCB
	Traverse x 1	Taps	Traverse x 1	Traverse x 1	x 3
40	Kiel	Wall	TC-J	3-hole	PCB
	Traverse x 1	Taps	Traverse x 1	Traverse x 1	x 3
41	Kiel	Wall	-	-	-
	5Probe x 2Rake	Taps	-	-	-
60	Kiel	Wall	TC-J	3-hole	-
	5Probe x 3Rake	Taps	5Probe x 4Rake	5Probe x 3Rake	-

upstream of the IGV plenum. The step size of the traversing 5-hole probe is set to 5mm. The horizontal traversed movement covers almost the complete diameter of the annulus at section 0. The Kiel probes are inserted into the locations at 75% radius of the annulus, and the static pressure taps are equally arranged along the duct circumference. In order to measure the inlet flow turbulence, the traversing 5-hole probe was once temporarily replaced by a hotwire probe (type: Dantec® CTA) during the test campaign.

Section 10: At section 10, the exit of the IGV plenum outlet section overlaps with the impeller inlet section. This section is heavily instrumented with moveable sensors, including two Kiel rakes, two total temperature rakes, and two 3-hole pressure rakes, each containing six probes in spanwise direction. The sensor arrangement is chosen to cover an equal area. During the performance tests at each IGV setting angle from -20° to 60°, before each speedline test started all rakes needed to be turned to the amount of IGV setting angle. The two rakes of the same type are mounted on a rotating hub with 180° offset to cover the whole 360° section by one half turn. The angular position of the rotating hub can be precisely set by an encoder-controlled step motor. The step size for the rotation is set to 2.5° to ensure high-resolution measurement. In addition to the probe rakes, section 10 contains 18 pieces of pressure taps equally distributed along the shroud wall, and 4

pieces along the hub wall to measure the local static pressure.

Sections 20 and 40: The two sections are installed with traversing probes, which are unconventionally inserted from the backside of the stage into the flow channel due to the obstruction caused by the IGV plenum mounted on the front side. The traversing probes include a Kiel, TC-, and 5-hole probe at section 20, as well as a Kiel, TC- and 3-hole probe at section 40. For each probe, the spanwise distance of the traversing movement has to be carefully examined in order to obtain a maximum coverage, while at the same time avoiding sensor collision with the wall. The probes can be also rotated by the step motors to be aligned to the oncoming flow. During the rotating test with these step motors controlled by the software, an in-situ searching for the flow direction was automatically processed before the probes started the measure.

Section 60: All TC-, 3-hole and Kiel probes are installed on a rotating shroud similar to section 10. However due to the space restriction caused by too many sensor wires tightly wrapped inside the shroud part, section 60 only covers a sectional area less than 90°, instead of a full 360° mapping as section 10. Since in the return channel between section 41 and section 60 (Figure 3.3), the static vanes are equally distributed which creates a nearly symmetric flow field at section 60 with pitchwise periodicity, the 90° measurement range at section 60 can be later reconstructed to cover an extended 360° area by the post-processing using periodic repeating.

In addition to the static sensors mentioned above, several fast-response PCB® sensors with three pieces in groups at section 10, 20 and 40 to continuously measure the dynamic pressure fluctuations as the stage approaches the surge limit. For the IGV test campaign, the thresholds of maximum pressure fluctuation are all set to 100 mbar peak-to-peak. The anti-surge valve will be opened immediately once this value is exceeded. The connection between the PCB sensors and the anti-surge valve is established through IfTA OMDS® (Oscillation Monitoring and Diagnostic System) with a sampling frequency of 51.2 kHz.

3.4 Measurement Accuracy

The measurement accuracy for the rotating test result mainly origins from the accuracy of sensors and the accuracy of instrument devices applied for the data acquisition.

The total and static pressure values are measured by Scanivalve® DSA 3218. Each chassis contains various signal receiving modules with measurement ranges of ± 1.0psi, ± 2.5psi,

±10psi, ±20psi and ±60psi, respectively. The measurement accuracy is 0.12% (F.S) for 1psi, 0.08% (F.S) for 2.5psi, and 0.05% (F.S) for 10psi, 20psi and 60psi modules. Before the rotating test, all pressure probes, including the 3-hole, 5-hole and Kiel probes, were newly calibrated by Nuovo Pignone® . In addition, the ambient pressure, which functions as the pressure reference, is measured by Rosemount® 3051 pressure transmitters inside the test cell with an accuracy of 0.04%.

For the temperature measurement, the TC-J sensors (thermocouple of type-J) and PT100 (Platinum resistance thermometer with resistance of 100 ohms) are connected to the TEMPpoint® modules. After calibration they have a measurement accuracy of 0.18°C. In addition, an Agilent® 34970A system with 1% inaccuracy for TC-J sensors is applied to provide some additional temperature channels for monitoring operation temperatures of the test cell, such as lubrication oil temperatures, driving motor temperatures, as well as temperatures on the vertical assembly walls and at exit volute.

The flow angle is obtained by an algorithm involving looking-up the calibration tables specifically for each individual 3-hole or 5-hole probes used, which achieves an accuracy of ±0.6° within the sensor calibration range. The traversed probe shafts are driven by the Velmex® step motors with high displacement accuracy (linear accuracy: 0.02mm; angular accuracy: 0.03°) to make sure that the probe movement driven by the step motors does not deteriorate its measurement accuracy.

The mass flow rate is measured by a Westenberg® venturi with 0.3% inaccuracy after calibration. The impeller rotating speed is computed by a speed sensor based on a phonic wheel, and a keyphaser as backup with ±5 rpm inaccuracy. The torque measurement is performed by Honeywell TMS® 9000 with an accuracy of 0.05% full scale.

The measurement uncertainty of the test result can be calculated based on the error propagation law according to NIST [66]. The propagation law states that for a given physical quantity q as a function of n independent parameters x_1, x_2, $\cdots$, x_n:

$$q = f(x_1,\ x_2,\ \cdots,\ x_n) \tag{3.1}$$

The uncertainty Δq can be calculated as:

$$\Delta q = \sqrt{(\frac{\partial q}{\partial x_1}\Delta x_1)^2 + (\frac{\partial q}{\partial x_2}\Delta x_2)^2 + \cdots, + (\frac{\partial q}{\partial x_n}\Delta x_n)^2} \tag{3.2}$$

Therefore, the uncertainties of performance parameters can be calculated by applying the original signal inaccuracies into Equation 3.2. As a result, the calculated uncertainties

for the stage performance parameters at the design point are: flow coefficient $\phi \approx 1\%$, polytropic efficiency $\eta \approx 0.2\%$, work coefficient $\tau \approx 0.7\%$ and head coefficient $h \approx 0.73\%$.

3.5 IGV Rotating Test campaign

During the IGV rotating test campaign, the three IGV configurations were installed with each at the IGV setting angles of -20°, 0°, 20°, 40° and 60° respectively, covering both the positive and negative ranges. The positive setting angle is defined by the swirl in the same rotating direction as the impeller, while the negative angle denotes the counter-rotating direction. The setting angles were pre-calibrated before the test campaign, and checked once per configuration change for each IGV type.

During the IGV rotating test campaign, each speedline was measured at a constant peripheral Mach number from choke down to the minimum flow rate before surge, including at least five steady-state measurement points on each speedline. The stage design point is derived from the original compressor stage without IGV, which is defined as the point with the designed value of flow coefficient at 0° setting angle. Since the pre-swirl or counter-swirl can shift the speedline to the left or right from its original mass flow range in the performance map, there is no real fixed design point for such a compressor stage with variable IGVs. For the later discussion, the middle point of each speedline is referred as nominal point, which is located near the efficiency peak of each speedline. Nearly all measurement points were recorded with the same ϕ for all three IGV groups, except that the points at the left (near-surge) and the right limits (choke) were determined by the real stage behaviors. The values of the flow coefficient ϕ at all nominal points (normalized) are summarized in Table 3.3.

Table 3.3: Flow coefficients at the nominal points of different IGV setting angles; shown are the values normalized by the value at design point

IGV angle [°]	-20°	0°	20°	40°	60°
ϕ	1.152	1.000	0.944	0.751	0.616

3.6 Performance Test Result

In this section, the test results from the performance tests for the stage components and the overall stage are presented. In order to exactly determine the separate source of losses, the stage components are firstly examined separately, including IGV plenum (section 0 -

10), impeller inlet (section 10), diffuser inlet (section 20) and diffuser outlet (section 40), and stage outlet (section 60). The performance test results for the IGV plenum can be compared with the earlier test data conducted at GE Global Research, including previous CFD results and measurements on a static test facility with the IGV plenum alone. By combining the flow quantities obtained at each section, the impeller performance (section 10 - 20), diffuser performance (section 20 - 40), the return channel performance (section 40 - 60) and the overall stage performance (section 0 - 60) can be obtained.

3.6.1 IGV Plenum Performance

The performance of the IGV plenum can be evaluated by its ability to control flow losses, and the quality of the swirling effect it generates for the impeller inlet. As the first test result, Figure 3.8 presents the yaw angle of the pre-swirl delivered at each setting angle for the three IGV types (left), and the averaged pressure losses (normalized by the value at design point) versus the yaw angle delivered at the plenum outlet (right). The non-dimensional pressure loss coefficient is defined by Equation 2.14 from the plenum inlet to the plenum outlet. In Figure 3.8 on the left, it can be identified that within the IGV setting range from -20° up to 60°, type-B and type-C have a better linearity between yaw angle measured and IGV setting angle compared to the baseline Type-A. Especially type-C only slightly deviates from the ideal linear line. In addition, it can be noticed that type-A generally has an overturned flow field ("overturn" = yaw angle magnitude larger than the setting angle) in positive and negative setting range, and type-B has largest overturned flow at -20°. This can be ascribed to the reason that although the biased camber line of type-B favors its positive range, it impairs the flow guidance within its negative range.

The right plot in Figure 3.8 demonstrates that within a small IGV setting range between +/-20°, type-B and type-C are able to successfully reduce the pressure losses up to 40%. This loss reduction offers a good basis for the compressor stage to obtain higher overall efficiency. At high IGV setting angles of 40° and 60°, type-C has a rapid increase in loss generation, and the level of loss coefficients quickly exceeds the other two types. In general, Figure 3.8 indicates a good agreement between the rotating test, the static test and the CFD prediction.

Figure 3.9 presents the distribution of local loss coefficients measured at the IGV plenum outlet (section 10). Since the IGV plenum outlet overlaps with the impeller inlet section, Figure 3.9 also shows the flow fields of different qualities at the impeller inlet. From left to right are the three IGV designs, and from top to bottom are the IGV setting angles of -20°, 0°, 20°, 40° and 60°. The local distribution of pressure loss coefficient not only quantifies

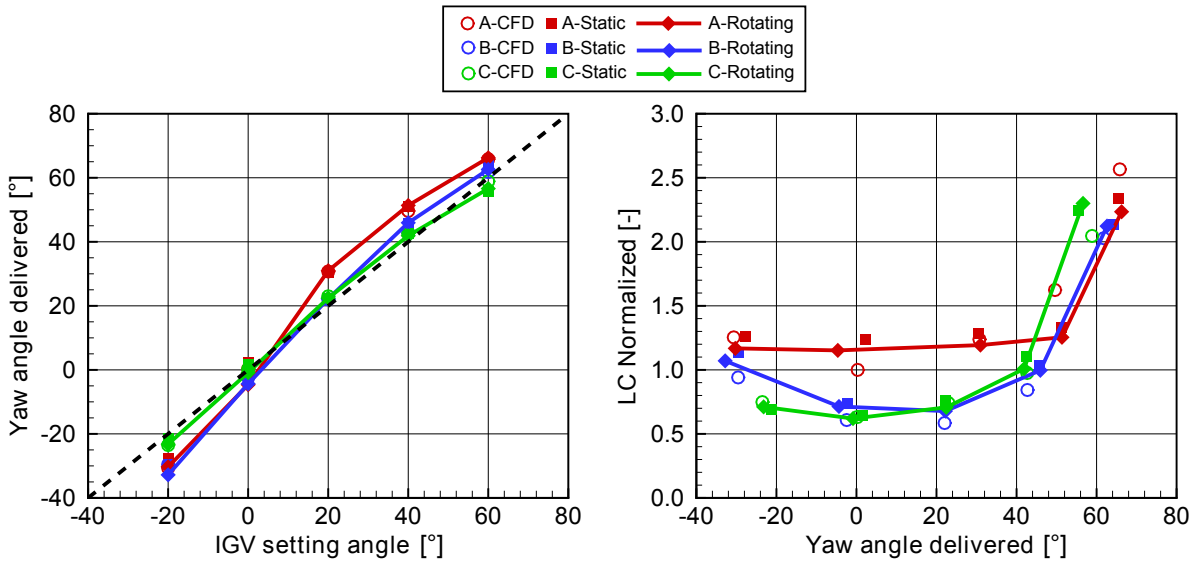

Figure 3.8: Yaw angle delivered at each IGV setting angle (left) and loss coefficient versus the yaw angle delivered at the plenum outlet (right); Compared are the results from rotating test, previous CFD simulation and static test

the flow losses, but also reflects the swirl patterns at the impeller inlet. For example it contains a clockwise-rotating pattern as representative of pre-swirl at IGV = 20°, 40° and 60°, and a counter-rotating pattern as counter-swirl at IGV = -20°. In addition at IGV = 0°, the loss pattern due to the contraction of the plenum inlet duct and the expansion of the plenum body can be also well identified. In general, type-B and type-C generate considerably less pressure losses than type-A, except that:

- Compared to type-C, type-B is not effective in reducing pressure losses at -20°. Actually, its contour map at -20° is almost identical as type-A. This finding agrees with type-B's design feature which only favors its positive working range.
- Compared to type-A and type-B, the capability of type-C in loss reduction is gradually declined as the IGV setting angle approaches 60°.
- At IGV = 60°, type-C even has increased flow distortion especially on the upper region near the shroud wall. This local flow distortion is consistent with previously the highest loss coefficient level for type-C at IGV = 60° in Figure 3.8.

A simple way to quantify the overall level of loss coefficient changes at section 10 is to introduce a counting parameter which represents the sum effect of all pressure losses measured. This can be realized by defining a "total pressure loss" parameter LC_{Σ} as an

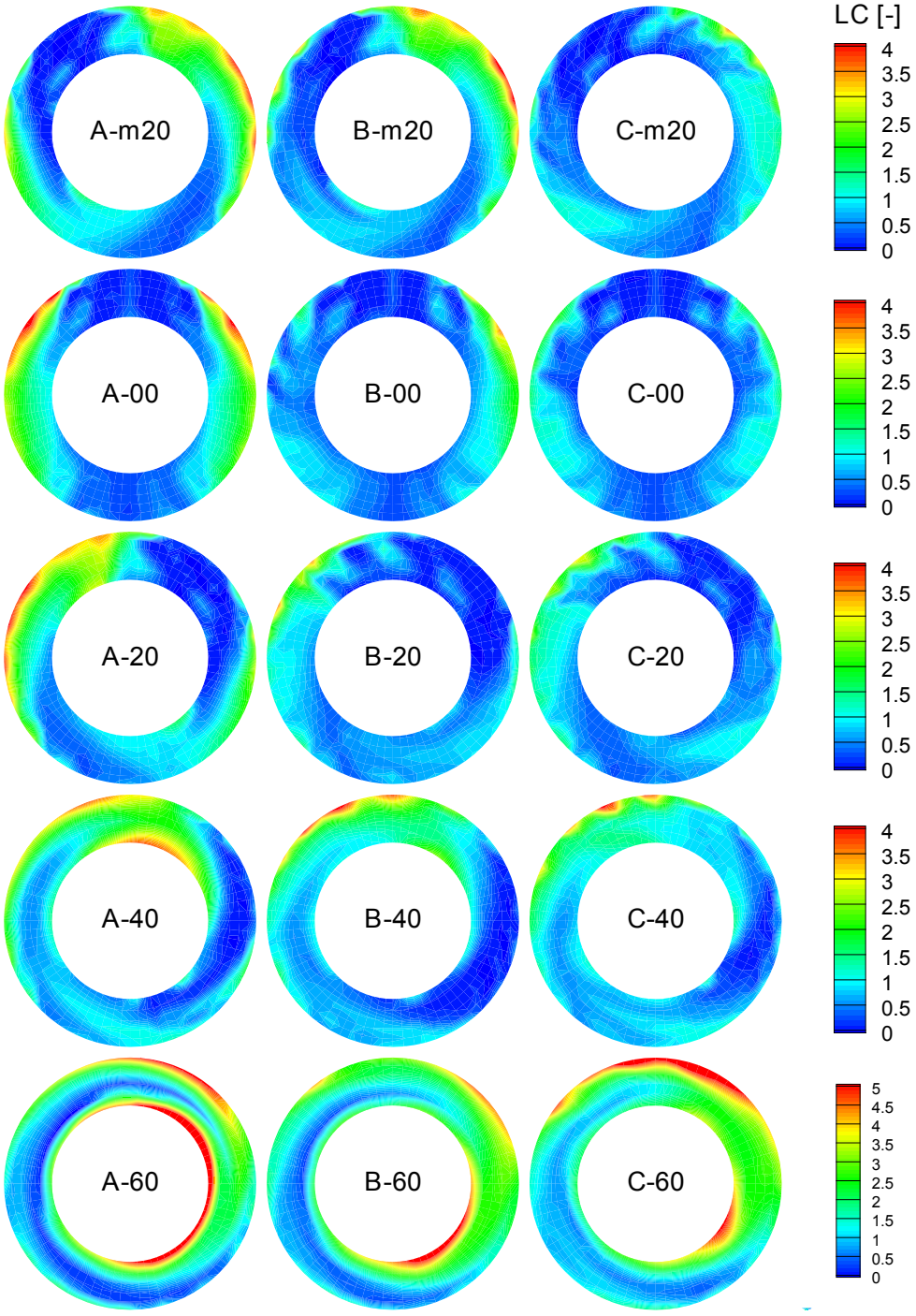

Figure 3.9: Loss coefficient at section 10 measured by the IGV rotating test

integral of each individual loss coefficient LC_i with its corresponding segment dA:

$$LC_\Sigma = \frac{1}{A_\Sigma} \int LC_i dA \tag{3.3}$$

as depicted in the Figure 3.10. Thus the contour plots in Figure 3.9 can be transformed into a clear chart with different levels as shown in Figure 3.11. Here all values are normalized by the level of LC_Σ for type-A at design point. Now it is quite clear that type-B and type-C generally have lower overall pressure losses than the baseline type-A. The benefits of type-B are mostly significant at positive IGV setting angles (from IGV = 20° to IGV = 60°), whereas type-C has lowest loss generation at IGV = -20° and IGV = 0°. The amount of improvements achieved by using the new IGVs can be quantified as much as 40% at lower IGV setting range (IGV = -20°, 0° and 20°). At higher setting ranges (IGV = 40° and 60°), however, the benefits of the two new IGVs begin to disappear. These findings are consistent with the trend of loss coefficent curves seen before in Figure 3.8, in which the benefits of pressure loss reduction for type-B and type-C were already cancelled out at IGV = 60°.

Figure 3.12 shows the contours of yaw angle measured at section 10. Again from left to right are the three IGV designs, and from top to bottom are the different IGV setting angles at -20°, 0°, 20°, 40° and 60°. At each setting angle on each row, the legend scale of all contour maps is chosen to be equally extended away from the setting angle as the middle value. It can be seen that the flow field provided by the IGV plenum at the impeller inlet is very non-uniform both in circumferential and in radial directions, and this flow non-uniformity is gradually diminished by type-B and type-C. In particular at IGV = -20°, type-A and type-B have very similar flow patterns and excessive regions of magnitudes, while type-C is able to deliver a much more uniformed flow with a magnitude closest to 20°. This indicates that type-B has little improvement in terms of providing uniform flow in negative working range. At IGV = 0° and 20°, both type-B and type-C show improved

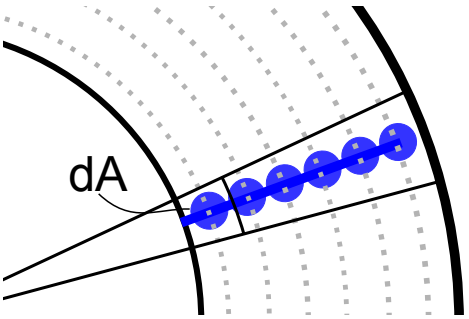

Figure 3.10: Sketch of the calculation method to obtain the total pressure loss at section 10

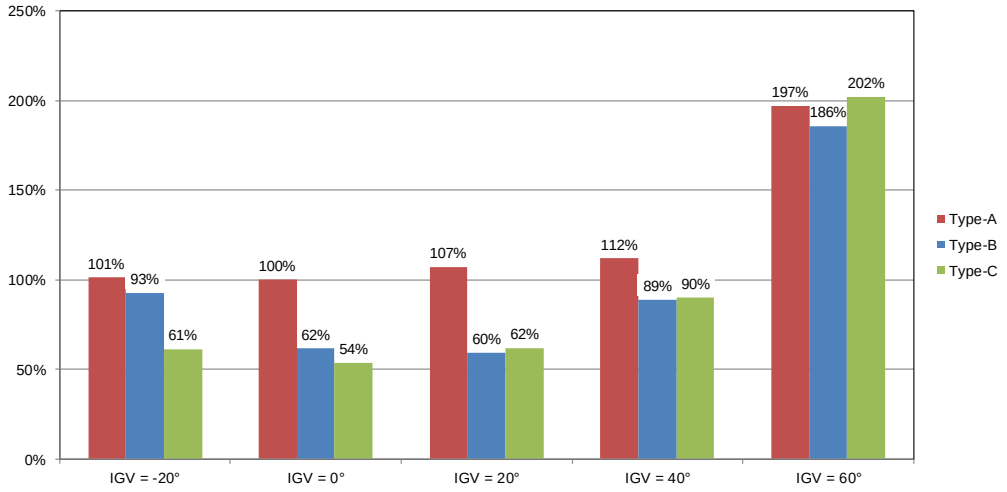

Figure 3.11: The total pressure loss parameter based on the loss coefficients; shown are the values in percentage and normalized to the value of type-A at IGV = 0°

uniformity compared to type-A, especially on the left half-circle section. At IGV = 40° and 60°, the magnitude levels among the three IGV types become quite obvious, which is consistent to their averaged levels shown before in Figure 3.8. Particularly at IGV = 60°, while type-A and type-B contain overturned yaw angle magnitude at e.g. midspan region, type-C still maintains an average level of around 60°. Also only the flow field generated by type-C does not contain an overturned in the midspan region. Figure 3.12 shows that while at lower IGV setting angles the differences among the three IGV types are mainly manifested in the amount of flow non-uniformity, at higher IGV setting angles the differences are mainly in the level of swirl angle.

Figure 3.13 presents the contours of axial Mach number measured at section 10 based on the calculation in Equation 2.18 to indicate the flow uniformity in the axial direction. From top to bottom, the absolute Mach number levels of legend scales continuously drop due to the ever-decreasing mass flow rate. Basically the flow features in the axial direction are agreed with the flow non-uniformity seen before in Figure 3.12. For example, type-B is similar to type-A at IGV = -20° and 0°, and type-C shows the mostly homogeneous flow fields in both positive and negative ranges. It can also be seen that the flow non-uniformity at IGV = 0° is mainly caused by the neck region of the radial plenum inlet. These local variations are later almost entirely eliminated by the strong swirl effects at higher IGV setting angles. These findings indicate that with suitable IGV designs and progressive setting angle, the swirling effect is advantageous to redistribute the flow field to be more uniform in the axial direction.

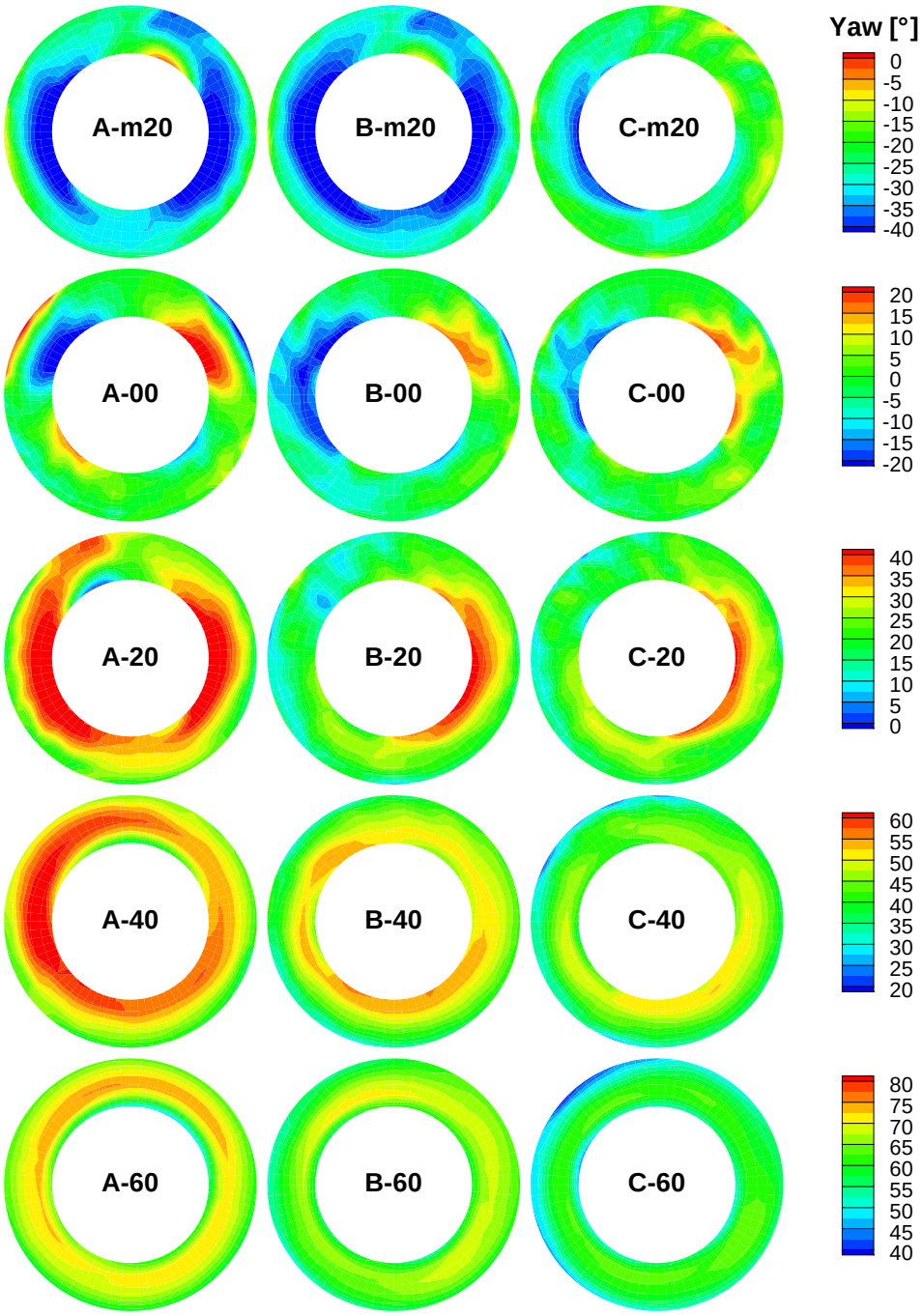

Figure 3.12: Yaw angle at section 10 measured by the IGV rotating test

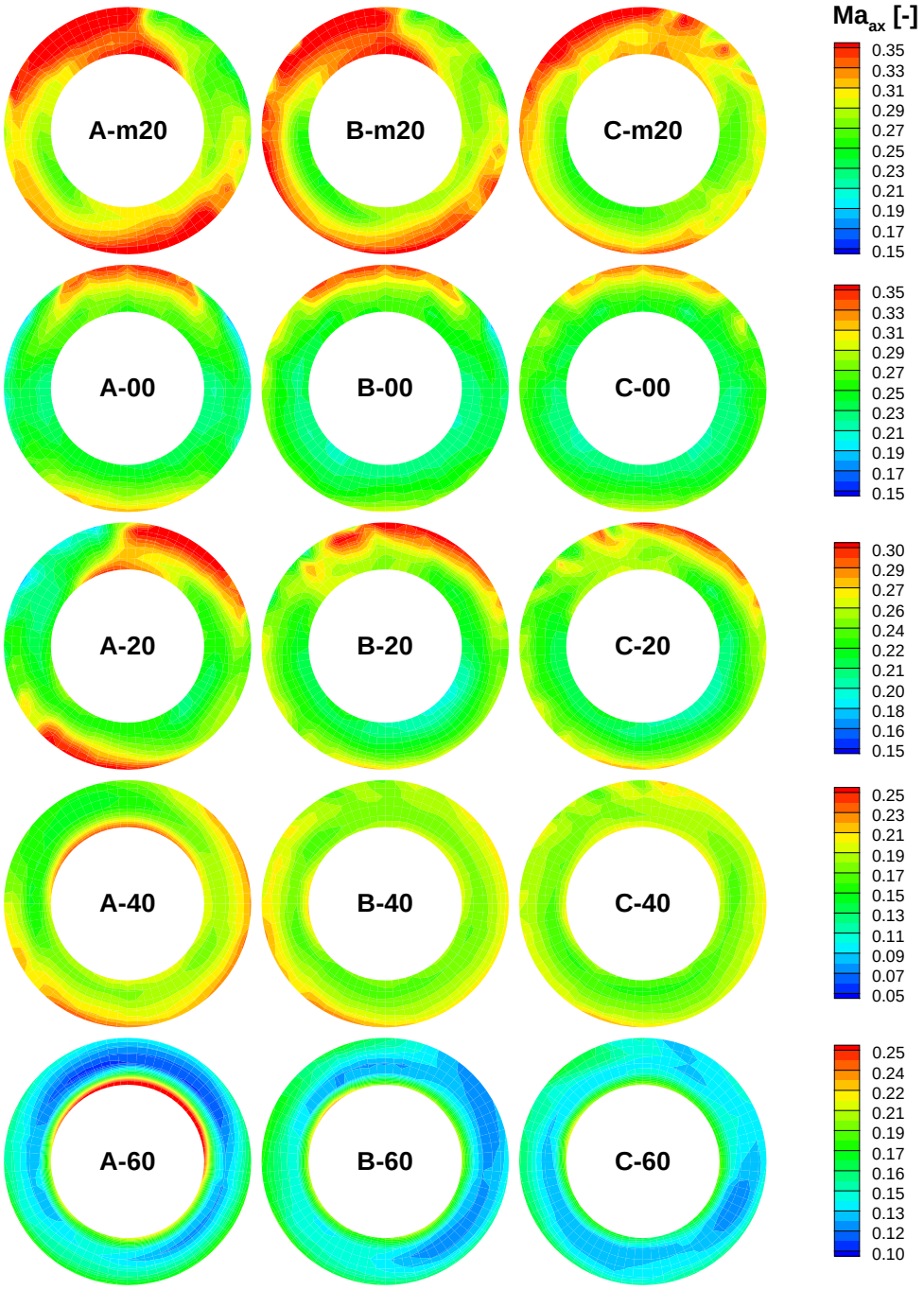

Figure 3.13: Axial Mach number at section 10 measured by the IGV rotating test

3.6.2 Impeller Performance

The impeller parameters between section 10 and 20 include total pressure ratio, work coefficient, polytropic efficiency and head coefficient. Due to the similar performance between the impeller and the overall stage as later seen in Section 3.6.4, the impeller total pressure ratio and the impeller polytropic efficiency are firstly discussed here.

The general compressor characteristics without IGVs can be demonstrated by the total pressure ratio (Π_t) versus flow coefficient ϕ, and the polytropic efficiency (η) versus flow coefficient ϕ as illustrated in Figure 3.14. The definitions of Π_t, η and ϕ can be found in Equation 2.9, 2.10 and 2.16. The limit at the minimum mass flow rate (surge limit) and the limit at maximum mass flow rate (choke) are also shown. A surge limit describes an operation point when the steady flow in the compressor completely breaks down due to the large flow separation occurred in the compressor blade passages at very low mass flow rate. A choke limit is a condition at the maximum allowed mass flow rate when the flow Mach number in the blade passages reaches unity. The compressor operation range is thus prescribed by the speedline (the characteristic curve at one constant speed) between surge and choke. As the mass flow rate decreases, the operation point moves from the right to the left along the speedline. When the mass flow rate reaches an optimum with a highest efficiency level, the operation point is defined as the design point (DP). If the mass flow rate further decreases, the compressor efficiency will dramatically drop due to the flow separation in the compressor blade passages. The efficiency of compression (η) would eventually affect the strength of compression (Π_t), so that the total pressure ratio Π_t would later also begin to drop as the operation point approach the surge margin until the minimum mass flow rate at the surge limit is reached.

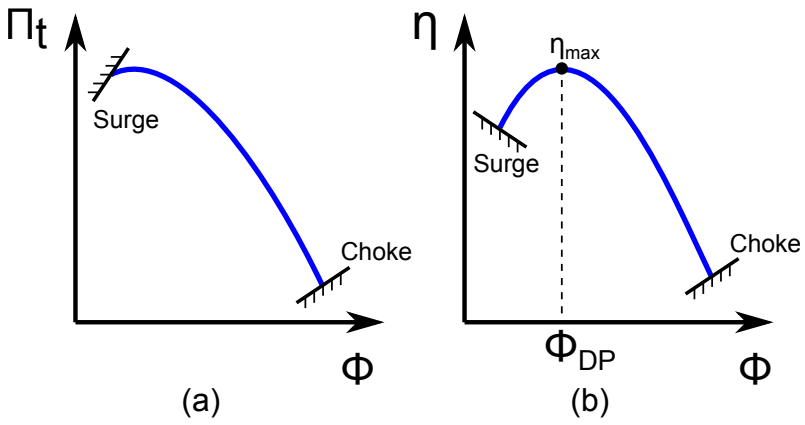

Figure 3.14: The curves of total pressure ratio (Π_t) (a) and polytropic efficiency η (b) for a general centrifugal compressor

Figure 3.15-(a) shows the test results of impeller pressure ratio versus the flow coefficient from the IGV test campaign. Each speedline denotes one of the three IGV types at a particular IGV setting angle. Both axis scales are normalized with their values at the design point. The five different line colors represent the different IGV setting angles from -20° up to 60°, while the three line shapes represent the three IGV types. Since the same impeller is applied, the total pressure ratio for each specific test case primarily depends on the incidence angle of the inlet flow. This is because a correct incidence angle, which is directly affected by the yaw angle magnitude measured in Figure 3.12, is the preliminary condition for the impeller inducer to work efficiently, which further guarantees a smooth compression in the impeller blade passages. At IGV = 0°, type-B and type-C already have higher Π_t than type-A. At IGV = 20°, type-C begins to deliver nearly identical Π_t levels as type-B, and both cases are still higher than type-A. Subsequently at IGV = 40° and 60°, type-C yields the highest Π_t compared to type-B and type-A. The highest level for type-C can be associated with its good linearity in the delivered yaw angle in respect to the IGV setting angle (Figure 3.8). In addition at IGV = -20°, type-B has the largest magnitude of yaw angle while type-C has the lowest level. Combined with their yaw angle magnitudes at IGV = -20° in Figure 3.9, it is likely that for this particular case at IGV = -20°, the ideal incidence angle for the impeller should be even lower than -20°, which is

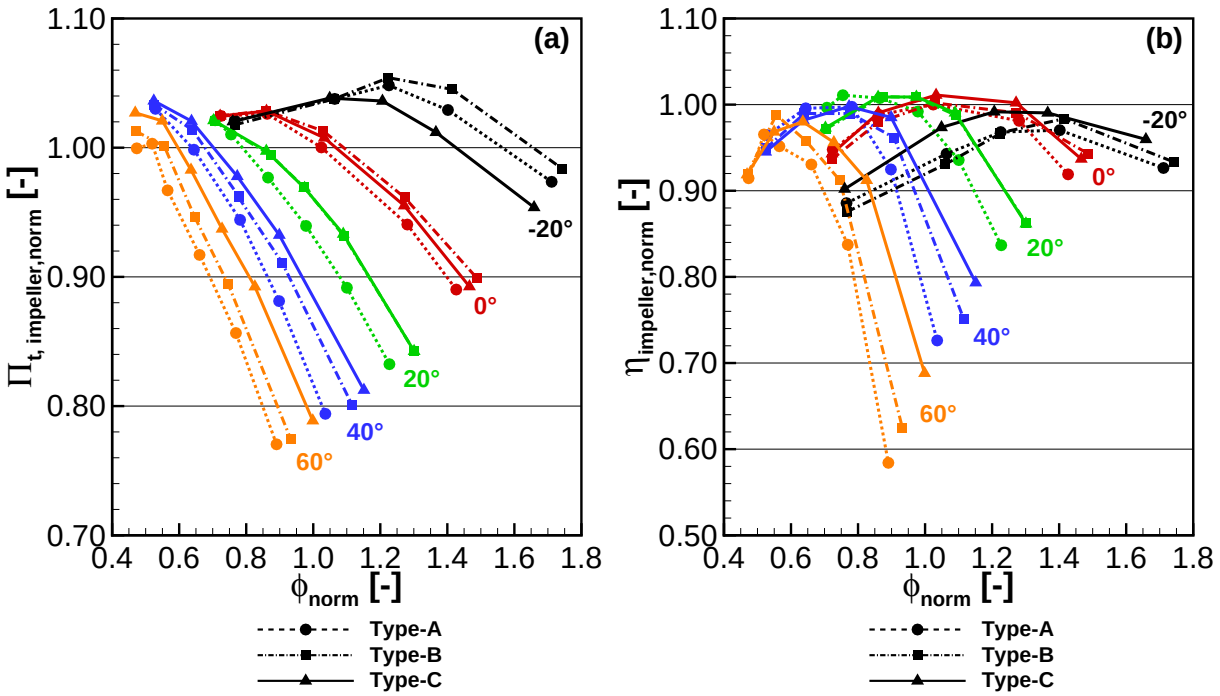

Figure 3.15: Impeller overall performance measured by the IGV rotating test; shown are total pressure ratio Π_t (a) and polytropic efficiency η (b)

best satisfied by the overturned counter-swirl induced by type-B.

Figure 3.15-(b) shows the polytropic efficiency η for all three IGV types. It is remarkable that at IGV = 0°, type-C yields the largest efficiency increase at the design point, surpassing type-A and type-B by 1%. This improvement is due to the improved flow uniformity demonstrated by Figure 3.12. For the other off-design points, type-B and type-C have even more spectacular improvements to the extend of as much as 20%, for example for IGV = 60° and near choke limit. However, in a practical centrifugal compressor stage with adjustable IGVs, these off-points can be substituted by other nominal points with better efficiency levels at other IGV setting angles. For example in Figure 3.15-(b), an operation point at $\phi_{\text{norm}} = 0.9$ for type-A at IGV = 60° can be substituted by the new point with the same flow coefficient at IGV = 20°, which yields a largely recovered efficiency level. In addition, although the improvements for type-B and type-C at IGV = 40° and 60° are significant, as mentioned before this comparison is inapproriate for type-A because its speedlines at higher setting angles are shifted further to the left due to its overturned flow. it is expected that if all three IGV types could work under their actual optimal mass flow rates at different high setting angles, the large benefits seen in the polytropic efficiency levels for type-B and type-C at IGV = 60° in Figure 3.15-(b) would be reduced.

3.6.3 Diffuser Performance

During the test campaign, the aero- and thermo-probes at section 20 and 40 were traversed in spanwise direction to obtain the steady-state points at each inserting depth. The points collected can be further post-processed as the circumferentially averaged profiles at section 20 and 40. Figure 3.16 present the total pressure profiles p_t/p_{t0} (normalized by the value of total pressure ratio at design point) and the yaw angle profiles measured at section 20 and 40. The span in percent is the relative distance from the hub wall (0%) to the shroud wall (100%). From left to right are the total pressure and yaw profiles for the nominal points at IGV setting angles -20°, 0° 20° and 60°. Since the profiles at section 40 generally have similar features as section 20 except the mixing-out effects in the diffuser channel, the discussion is mainly focused on section 20.

Total Pressure

The differences in the total pressure profile between the three IGV types become larger as the IGV setting angle increases. Originally at IGV = -20°, the three IGV types have only marginal differences. At IGV = 0°, the profile of type-A starts to have a deficit in the near-shroud region, and type-B has the largest p_t level due to the best filled shape near

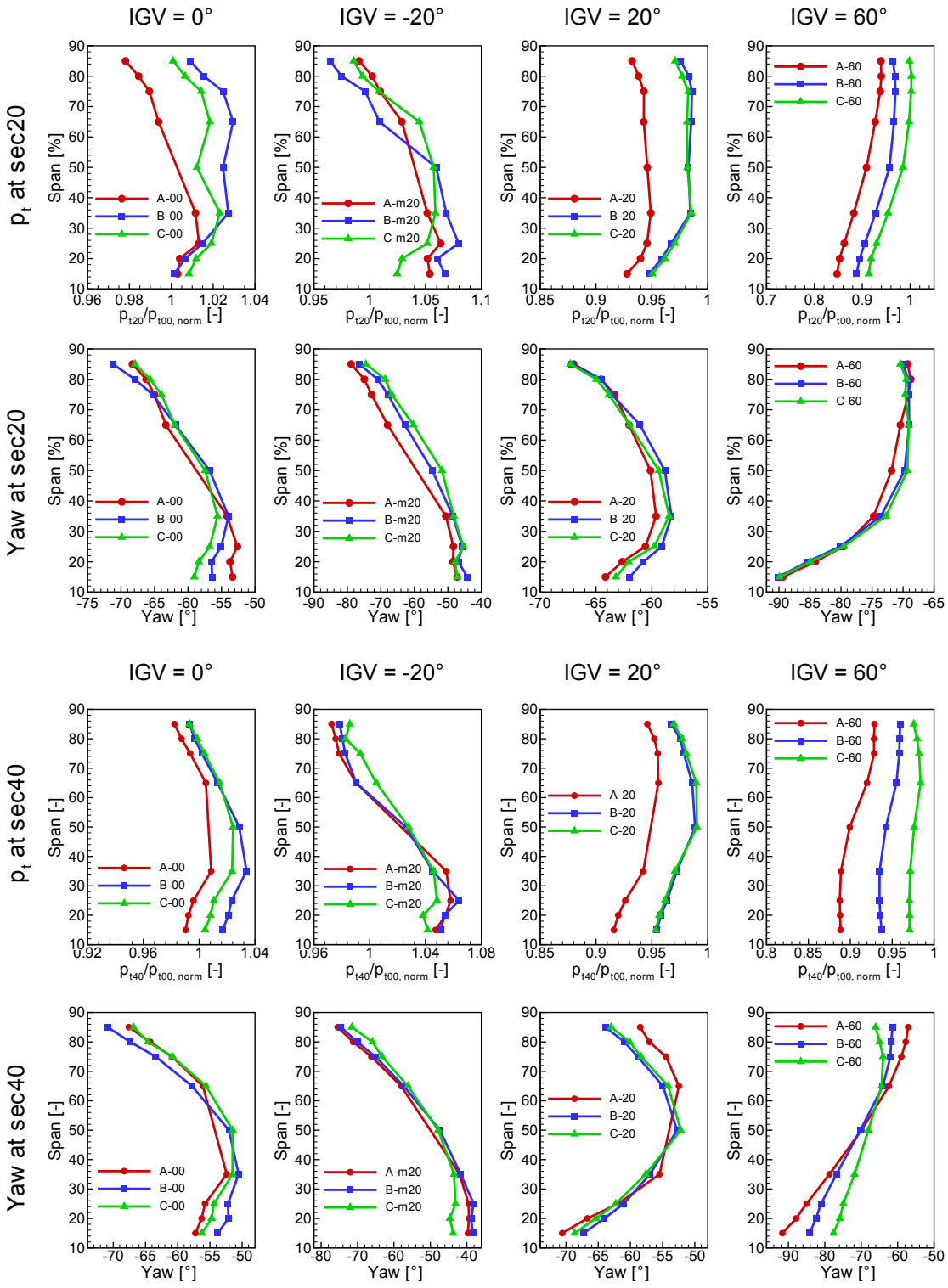

Figure 3.16: Diffuser performance at section 20 measured by the IGV rotating test; shown are the flow profiles of p_{t20}/p_{t00} normalized by the value at design point and the yaw angle

shroud. At IGV = 20°, type-B and type-C have nearly identical p_t levels, which clearly surpass the levels shown in the profiles for type-A. At IGV = 60°, type-C becomes the

highest level, then followed by type-B and type-A. Therefore, the findings here can be regarded as a supplement to what has been found from the impeller total pressure ratio in Figure 3.15-(a). Besides the comparison between the three IGV types, as the setting angle increases from -20° up to 60°, all p_t profiles tend to change from a hub-strong to a shroud-strong shape. This is a general feature for the flow in a centrifugal compressor as the mass flow rate decreases, because in most cases as the compressor approaches stall, the local reverse flow firstly appears on the hub-side wall at the diffuser inlet region Senoo [71].

Yaw angle

The yaw angle is mainly dependent on the radial velocity at the impeller outlet (c_{r20}), and the circumferential velocity c_{u20} corresponding to the rotating speed u_{20}. The local flow phenomena such as flow separation and re-attachment also affect the local yaw angle magnitude in the vicinity of the hub and shroud. Considering that the circumferential velocity at section 20 c_{u20} depends merely on the rotating speed u_{20}, which was kept constant for each speedline, the yaw angle profile largely represents the radial velocity profile c_{r20}. As the IGV setting angle increases from -20° up to 60°, the minimum magnitude of yaw angle gradually switches from the hub side to the shroud side, indicating the radial velocity c_r changes from a hub-strong type to a shroud-strong type. The maximum magnitude of yaw angle (around -90°) is accompanied by the minimum circumferential velocity c_{u20} (around 0). This is the case for all three IGV types at IGV setting angle 60° at section 20, and for type-A only at section 40. At IGV = 60°, all three IGV types generate yaw angle levels of larger than 90° near the hub, indicating that a reverse flow exists on the hub for all three IGV types. After passing through the diffuser channel, the magnitude of yaw angle for type-B and type-C decrease to less than 90°, while the yaw angle of type-A becomes even larger. This indicates that while for type-B and type-C the diffuser flow has been recovered by the diffuser, for type-A the reverse flow further develops in the diffuser.

3.6.4 Stage Overall Performance

The stage overall performance can be derived by combining all stage components as a whole from section 0 to 60. Figure 3.17 summarizes the test results of the stage characteristics as stage total pressure ratio, stage work coefficient, stage polytropic efficiency and stage head coefficient. In addition in Figure 3.17-(d), the stage surge limits during the performance tests are shown together. They will be discussed in the next surge test session.

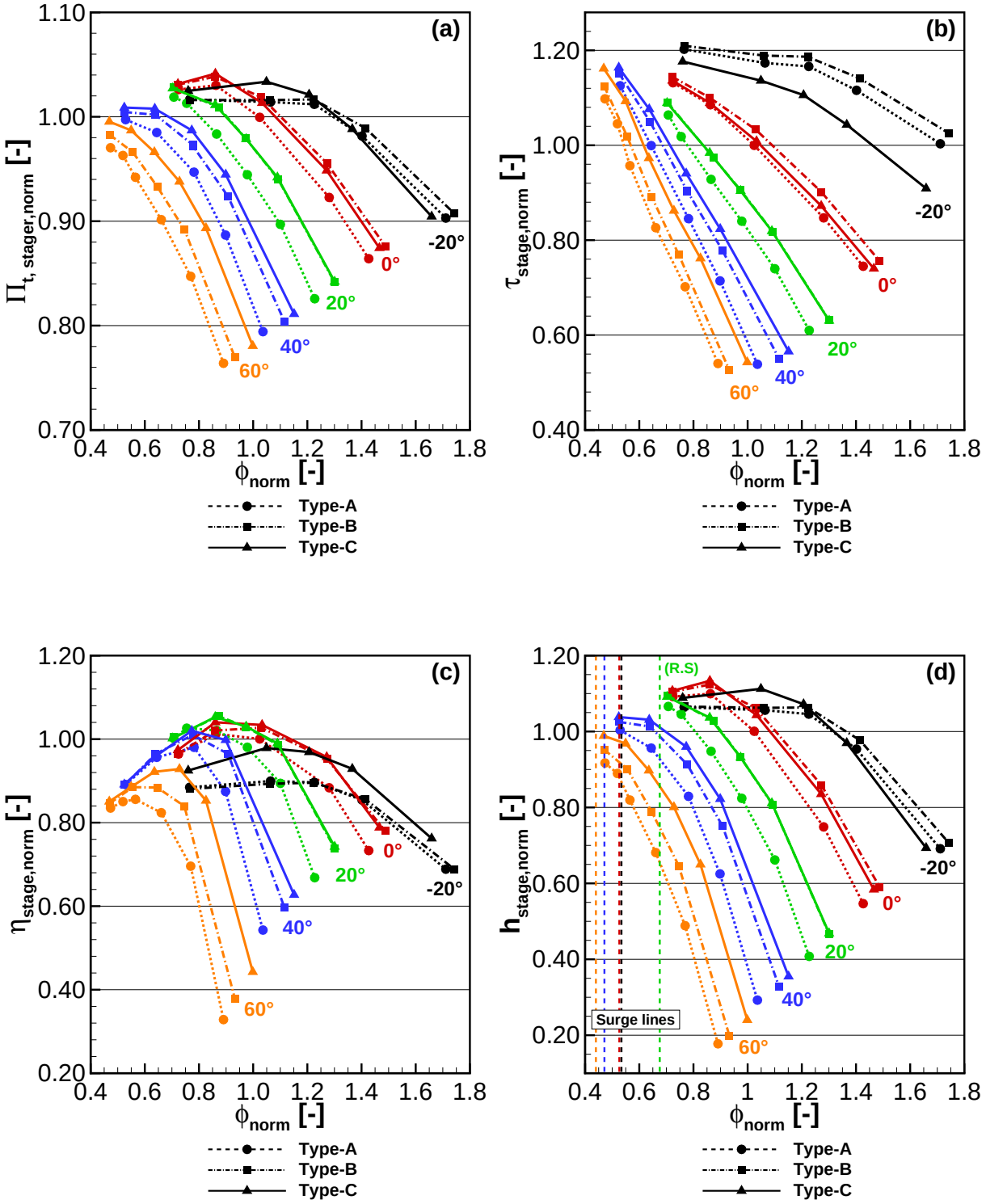

Figure 3.17: Stage overall performance measured by the IGV rotating test; shown are total pressure ratio Π_t (a), stage work coefficient τ (b), polytropic efficiency η (c) and head coefficient h (d). All values are normalized by the values at design point

Stage Total Pressure Ratio

Figure 3.17-(a) shows the stage total pressure ratio measured between section 0 and section 60. Similar to the impeller performance shown before in Figure 3.15, the improvements achieved by the application of two new IGV types are clearly to be seen. Along each performance curve, the maximum total pressure rise is located under high impeller loading, often appeared as the last or the second last point towards the surge limit. At design point ($\phi_{\text{norm}} = 1.0$) while IGV = 0°, the total pressure ratio levels obtained by type-B and type-C surpass the original level of type-A by at least 2%. At IGV = 20°, type-B and type-C have almost identical total pressure ratio along the complete speedline curves, which are 3% higher than type-A at the nominal points ($\phi_{\text{norm}} = 0.94$). As the IGV setting angle further increases to 40° and 60°, the deviations between the three IGV types at the same mass flow tend to be even larger. At IGV = 60°, the gaps in the total pressure ratio between type-A and type-C at nominal point ($\phi_{\text{norm}} = 0.616$) is enlarged to as much as 6%. The improved performance can be also identified at off-design points especially near the choke limits.

Stage Work Coefficient

For an adiabatic system with neglected heat losses in the diffuser component, the stage work coefficient is equivalent to:

$$\tau = \frac{\Delta h_t}{u_{20}^2} = \frac{u_{20}c_{u20} - u_{10}c_{u10}}{u_{20}^2} \tag{3.4}$$

in which the circumferential velocity c_{u10} is dominated by the inlet swirl generated by IGV as previously discussed in Chapter 2. The magnitude of c_{u10} is indirectly given by the yaw angle in Figure 3.12. A stronger pre-swirl manifested as a larger positive yaw angle and thus the magnitude of c_{u10}, decreases the work coefficient, while a stronger counter-swirl with larger negative yaw and c_{u10} lead to a work coefficient increase. As a consequence, the relative levels of impeller work coefficient can be regarded as the shifted results caused by the upstream swirl, as indicated in Figure 3.17-(b). Due to the better flow linearity and thus controlled swirl magnitude (small positive c_{u10}), type-C has the largest level of work coefficient at 60°. Meanwhile, at IGV = -20°, type-B becomes the largest one due to its strong overturned counter-swirl (large negative c_{u10}).

Stage Polytropic Efficiency

Figure 3.17-(c) shows that the benefits obtained by type-B and type-C can be as much as 2% in stage efficiency at design point 0°. They also surpass the baseline clearly at other off-design points. However, the improvements at off-design points need to be considered together with the shifting effects of incidence angle caused by different amount of pre-swirl. At IGV = -20° while type-C has a clear benefit compared to the baseline, type-B shows almost an identical level as type-A. The relative levels between type-C and type-B are more clearly than in the previous Figure 3.15 for the impeller performance, indicating that the large loss generation associated with type-B at -20° in the IGV plenum has a great impact on the overall stage.

It is expected that if a real-time IGV adjusting mechanism could be realized, the performance map for each IGV type would become an envelop curve comprised of all individual points with the efficiency peaks obtained by all speedlines from IGV = -20° to IGV = 60°. Figure 3.18 presents such a "fictive stage performance" containing three envelope curves for each IGV type. The length of each envelop curve has extended to a wider range, which indicates the IGVs can significantly improve the operation range of the compressor stage. The three curves clearly demonstrate that although type-B and type-C are both advanta-

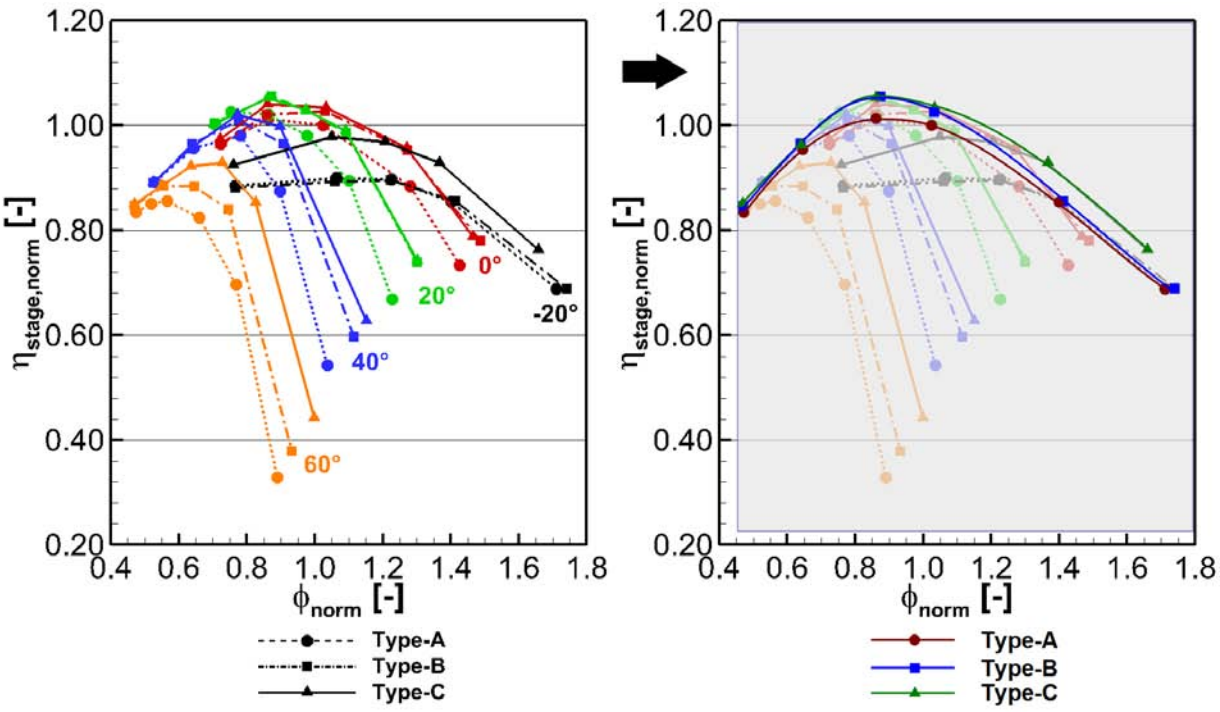

Figure 3.18: the assumed stage polytropic efficiency as the envelop curves covering all measurement points

geous in achieving higher efficiencies at small mass flow rates, type-B gradually loses its advantage at larger mass flow rates. In contrary, type-C maintains the highest efficiency levels at large mass flow rates. The different characteristics between type-B and type-C shows again the advantage of using a flapped design for type-C in comparison to the one-directional biased design of type-B. In practice with the realization of an adjustable mechanism for the IGVs, type-C will be the best choice over the complete operation range.

Stage Head Coefficient and Surge Margin

The head coefficient can be regarded as a combination of compression efficiency (η) and energy transfer into the fluid (τ), which is a common stage parameter in the Oil & Gas industry to quantify the compression capability of process compressors. It can be concluded from Figure 3.17-(d) that type-C is the best choice in terms of highest head coefficient delivered. At design point, type-B and type-C have about 5 % increase in the stage head coefficient compared to the baseline type-A.

For the convenience of later discussion for the surge test, the surge limits for each speedlines are also marked here in Figure 3.17-(d). During the surge test it was found that all three IGV types have identical minimum mass flow rates ($\Delta < 1\%$) at all IGV setting angles. Therefore, only one line is drawn which denotes all three IGV types at one IGV setting angle. It can be seen that at IGV = 0° and 20°, the locations of maximum head points are still with a distance from the surge margin. In contrast at IGV = 40° and 60°, the maximum head points are already very close to the surge margins, and thus might be not utilized in practice due to safety reason. The same locations of surge limits for all three IGV types indicate that the two new IGVs do not impose additional benefits regarding their capabilities in the surge margin expansion.

3.7 Surge Test Result

This section summarizes the analysis of dynamic test results based on the surge test.

3.7.1 Test Procedure

The surge test was conducted as a dynamic process by approaching the left limit from the nominal point with moderate, constant steps of throttling mass flow (0.1% in every 5 seconds) until the dynamic pressure oscillations exceed the threshold of 100 mbar peak-to-peak. This left limit detected is then specified as the surge limit. Therefore, the

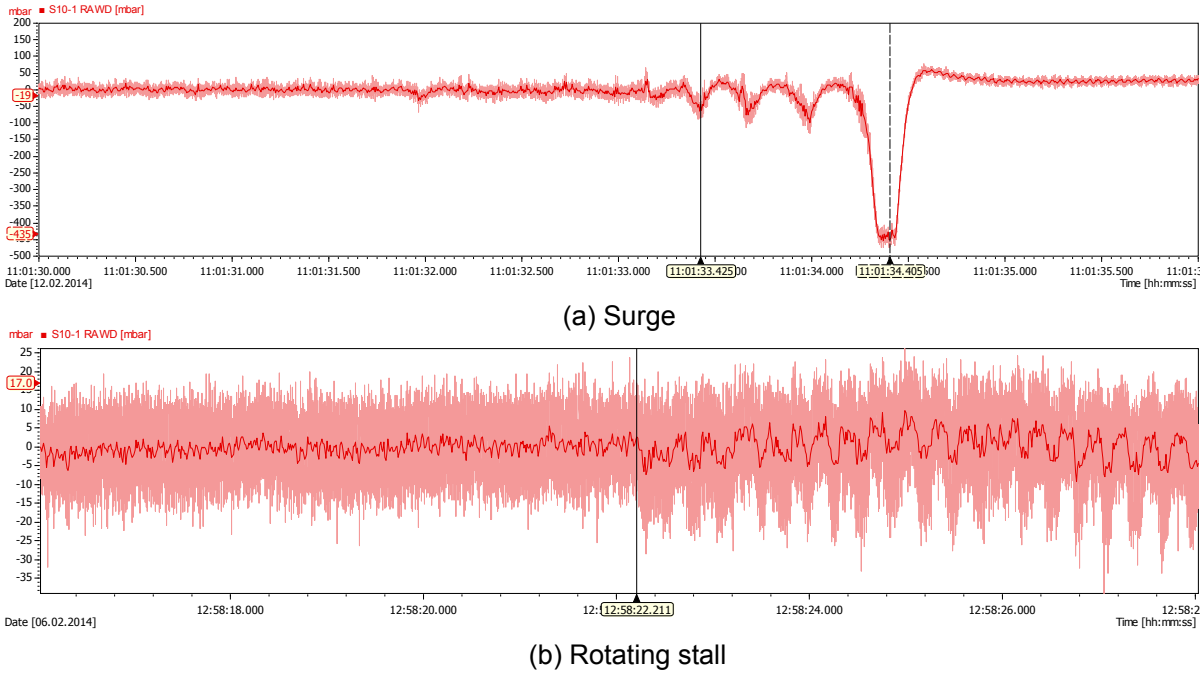

Figure 3.19: Example of dynamic pressure signals during surge and rotating stall; shown are the surge for type-A at 60° (a) and the rotating stall for type-A at 20°

"surge" defnition adopted for this study is actually a stability criterion based on pressure perturbations, which distingushes itself from other types of surge definitions such as the one determined by the occurance of periodic cycles between compressor flow breakdown and recovery by Day [23]. Therefore, the surge limit determined by this study is more conservative compared to the surge with deep breakdown cycles. For each IGV type at each IGV setting angle, the surge process was performed twice to ensure test repeatability.

The surge limits acquired by this way have been already shown in Figure 3.17-(d). For the test cases at IGV = -20°, 0°, 40° and 60°, they are exactly the locations during the surge test where the anti-surge valve was triggered. An exception is recorded at IGV = 20°, where during the surge test all three IGV types delivered a rotating stall. The rotating stall occurred much earlier than the other test cases, and during rotating stall the pressure disturbances were still below the threshold level. Therefore, in Figure 3.17-(d), the limit lines at IGV = 20° are noticeably much closer to the last measurement points on the left.

In order to illustrate such distinct features in the dynamic pressure signals between surge and rotating stall, Figure 3.19 shows the dynamic pressure amplitude versus the time progress for a surge process (e.g. type-A at IGV = 60°) and a rotating stall process (e.g. type-A at IGV = 20°). On the time axis, since there are too many dynamic pressure data collected within very short time scale, the test data overlap together into a fictive

curve with dark color. For this reason, later on the dynamic pressure amplitude will be shown together with its calculated RMS value, which is often used to evaluate the averaged fluctuation level. The first cursor in both plots indicates the onset of surge or the onset of rotating stall, and the second cursor in Figure 3.19-(a) denotes the time when the anti-surge valve was triggered. On the vertical axis, in order to to visualize the whole amplitude ranges of the surge signal and the rotating stall signal, the two axis ranges are different as much as 10 times. For the surge signal at the time when the surge event occurs, the dynamic pressure firstly had three resonance cycles with propagating amplitudes. Then the pressure amplitude exceeds the threshold so that the whole dynamic process has to be terminated by opening the anti-surge valve. Compared to the surge signal, the rotating stall signal only contains a series of limited oscillating cycles. It indicates that rotating stall stands for a certain flow state when the excitation and the damping effect reaches a dynamic equilibrium. It will be shown in the following discussion that the differences in the surge signal and the rotating stall signal are related to their dominate frequencies. A Fast Fourier Transformation (FFT) calculation will be applied to transfer the signal in the time series into frequency domain (displayed as waterfall plots).

3.7.2 Measurement Result

During the surge test, it is found that the three IGV types actually have very little differences regarding their surge behavior. It will be demonstrated later that for this centrifugal compressor stage, the diffuser part is the dominant component for the surge. Since the IGVs only change the local flow conditions at the impeller inlet, their effects on the downstream diffuser are very limited. Therefore in this section, only the measurement data of the type-A test cases are presented.

The result discussion covers the test cases at IGV = 60°, 20°, 0° and -20°. The test cases at IGV = 40° are very similar to the test cases at IGV = 60° and thus omitted. The analysis beginning with IGV = 60° is helpful because there the signals are dominated by a pure surge only. At IGV = 20° the signals reflect the features of rotating stall. At IGV = 0° and lastly at IGV = -20°, the dynamic pressure signals are comprised of a mixing combination of stall-to-surge flow features and miscellaneous disturbances caused by the counter-acting swirl at the impeller inlet.

The dynamic pressure signals are extracted from section 10, 20 and 40 as illustrated before in Figure 3.3. At each measurement locations a pair of two PCB sensor signals will be shown. The sensor arrangement at each measurement section may cause the the dynamic pressure amplitude measured by each PCB sensor to vary, since the internal flow

is asymmetric along the whole 360° circumference. However, for the surge study it is still acceptable since for the surge study the signal characteristics are dominated by the frequency instead of the amplitude.

The dynamic measurement data are represented in three forms: original raw signals (2 channels per each section), RMS values (2 channels per each section), and power spectrum (1 channel per each section). The power spectrum plots, or often called the waterfall, are set within a narrow frequency range up to 500 Hz. Thus the high-order frequency harmonics and the blade passing frequency ($n/60 \times 17 \approx 3500$Hz) will not be shown. The time cursor is always located at the time when surge or rotating stall firstly occurs.

IGV = 60°

Figure 3.20: At IGV = 60°, the compressor stage is able to operate at extreme low mass flow rate compared to the other test cases. During the surge test when the minimum mass flow was reached, the surge started with a clear audible violent noise with significant dynamic pressure increase within very short time. At this point, the inflow at the impeller inlet was so weak that the pressured air at the impeller outlet pushed back to the inlet. This strong surge effect is captured by the ever-increasing dynamic pressure amplitude as shown in Figure 3.20-(a). The RMS plots further indicate that during the accumulated pressure oscillations, several stepwise jumps of oscillation levels were recorded. It might be due to the compound sources of flow instabilities coming into effect as the mass flow rate decreases continuously. On the right side, the power spectrum plots indicate at section 20 and 40, a dominant, low frequency around 25 Hz accompanied with its 2^{nd} order harmonics. The 25 Hz frequency is mostly intensified at section 40 (diffuser outlet). Combined with the yaw angle measurement before in Figure 3.16 which shows a reversed flow existing in the diffuser, it becomes clear that the flow instabilities in the diffuser is the main source for the surge of the compressor stage. Compared to section 20 and 40, at section 10 hardly any frequency band can be detected. The low frequency at 25 Hz is consistent with the theoretical frequency range for a Helmholtz resonator Fink [32], which is often introduced as a simplified dynamic model (see Figure 3.21) to characterize the oscillations equivalent to the back-and-forth flow instabilities in the diffuser channel. Specifically, the Helmholtz frequency w is defined by Greitzer [39] as:

$$w = a\sqrt{\frac{A_c}{V_p L_c}} \tag{3.5}$$

in which a is the speed of sound, A_c the flow-through area of the compressor, V_p the exit plenum volume, and L_c the effective length of an equivalent duct for the test section.

It is interesting to notice that as depicted in Figure 3.21, the installation of IGVs actually does not change the duct equivalent length L_c, and thus the Helmholtz frequency w. As a consequence, the application of three IGV types should not change the surge frequency. This is the reason for the finding that all three IGV types have very similar dynamic behaviors during the surge tests.

IGV = 20°

Figure 3.22: During the surge tests, at IGV = 20° a clear sound of rotating stall was detected at very early state as the operation point started to move to the left along the speedline. The recorded mass flow rate during the rotating stall is larger than any other surge limits. The distinct characteristics of rotating stall is best described by its power spectrum as shown in Figure 3.22-(b). In addition to the 25 Hz frequency belonging to the surge frequency, there is another frequency band around 165 Hz (section 40 even contains its 2nd order harmonics). The frequency magnitude is a typical rotating stall frequency at $\omega_{stall}/\omega_{speed} \approx 0.80$ (Frigne [34]). The correlation between stall frequency ω_{stall} and rotating speed frequency ω_{speed} suggests that the rotating stall involves the stall cells which are continuously propagating in the circumferential direction against the compressor rotation Japikse [55]. The difference between surge frequency (25 Hz) and rotating stall frequency (165 Hz) is consistent with the conclusion by Greitzer [40] that the surge frequency is typically one order of magnitude less than the rotating stall frequency. This is because compared to the rotating stall frequency, the surge frequency has to take into account the very large exit plenum as depicted in Figure 3.21, resulting in a larger V_p term in Equation 3.5. The concurrence of surge frequency and rotating stall frequency suggests that if the surge tests at IGV = 20° were not interrupted by the rotating stall, the compressor stage would eventually reach its surge limit at a lower mass flow rate.

In comparison to the surge at IGV = 60°, three major differences can be identified for the rotating stall at IGV = 20°:

- In the power spectrum, the rotating stall is characterized by another completely different frequency with one order higher than surge frequency.
- In the RMS plots, the amplitude of pressure oscillations increases in an intermittent manner, jumping stepwise from lower level to higher level. Instead, the amplitude of dynamic pressure signal for a surge process increases continuously.

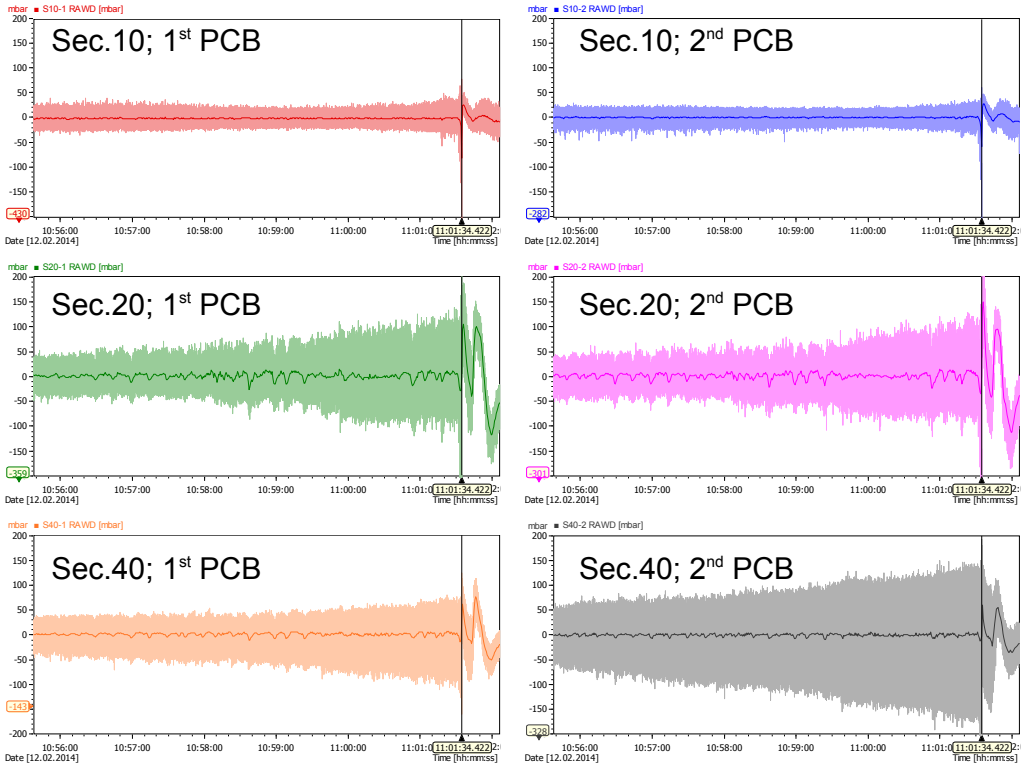

(a) Dynamic pressure raw signal in the time domain at IGV = 60°

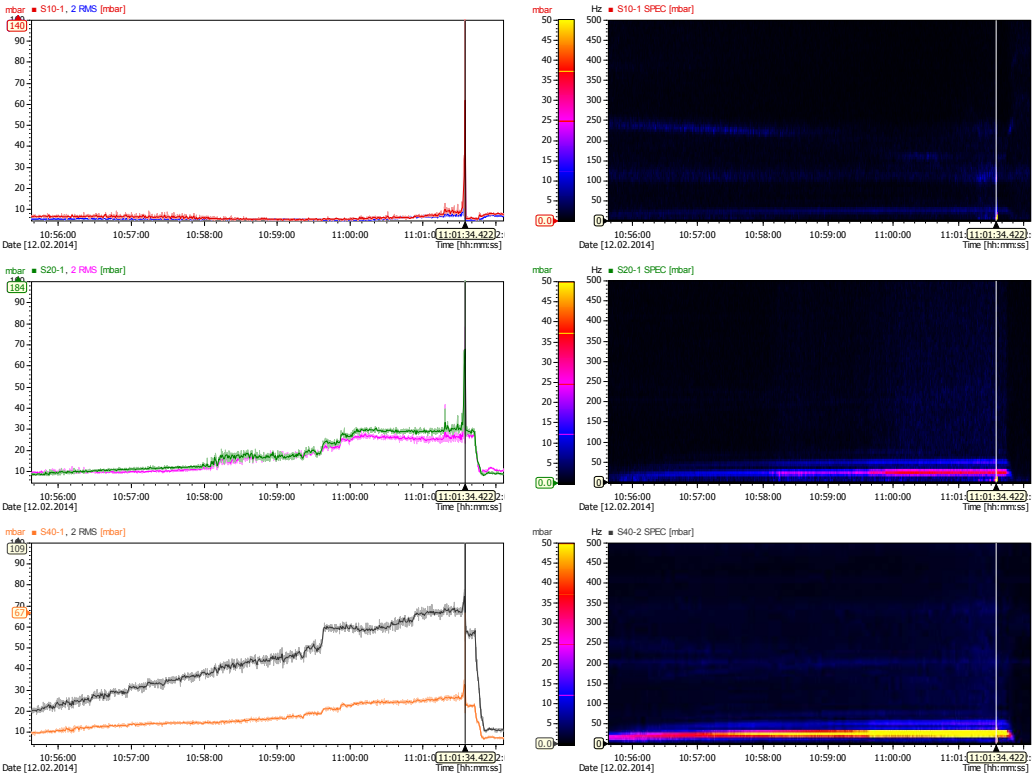

(b) Dynamic pressure as RMS signal (left) and power spectrum (right) at IGV = 60°

Figure 3.20: Dynamic pressure measured at section 10, 20 and 40 as raw time signal (a), RMS time signal and power spectrum (b), IGV = 60°

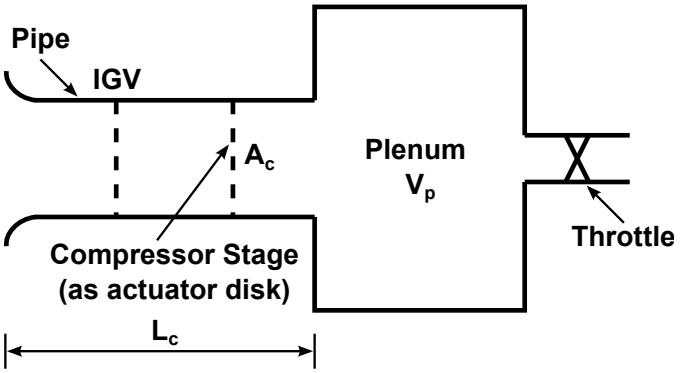

Figure 3.21: Equivalent compressor system as a Helmholtz resonator from Greitzer [39]

- Every time after the signal amplitude jumps to another higher level, the signal is able to stabilize at least for a certain time period at its new level. It suggests that rotating stall involves limited cycles established by the dynamic equilibrium between stable and instable factors.

IGV = 0°

Figure 3.23: The signals at IGV = 0° delivers a mixture of what has been detected separately at IGV = 60° and IGV = 20°. As the mass flow rates decreases, a weak stall frequency at 165 Hz similar to the test cases at IGV = 20° firstly shows up, but then disappears as the low frequency at 25 Hz similar to the cases at IGV = 60° becomes dominant. During the transition from stall to surge, the amplitude of dynamic pressure has a certain time period of settlement, suggesting that the tendency to stall is suppressed during the time progress.

IGV = -20°

Figure 3.24: The negative IGV setting angle at IGV = -20° causes the swirl generated by the IGVs (counter-swirl) rotates in the opposite direction to the impeller. The inlet distortion increases correspondingly due to the local flow instabilities stirred up by the two counter-rotations. This flow feature can be demonstrated by Figure 3.24-(a) for the first time in which the dynamic pressure signals at section 10 have large oscillations even earlier than section 20 and 40. The inlet flow instabilities can be also substantiated by the fluctuating RMS levels at section 10 long before the surge starts.

However, in the power spectrum plots although there are several intermittent frequency bands corresponding to the flow instabilities at section 10, the mostly dominant frequency is still the surge frequency around 25 Hz. The 25 Hz frequency is particularly strong at

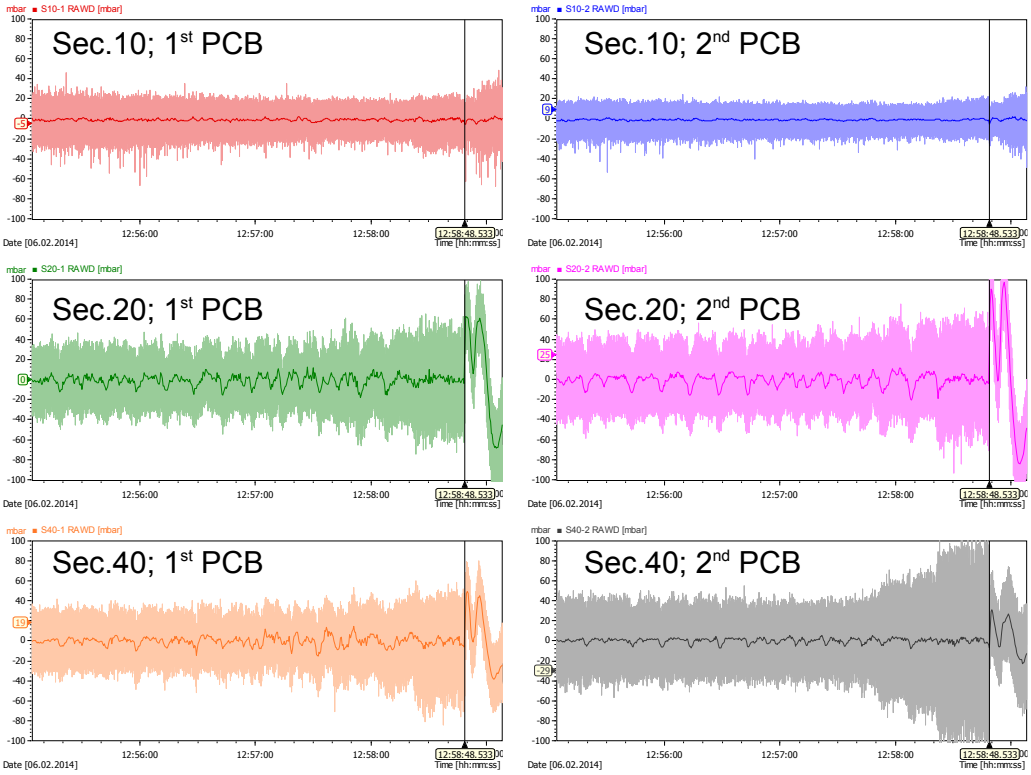

(a) Dynamic pressure raw signal in the time domain at IGV = 20°

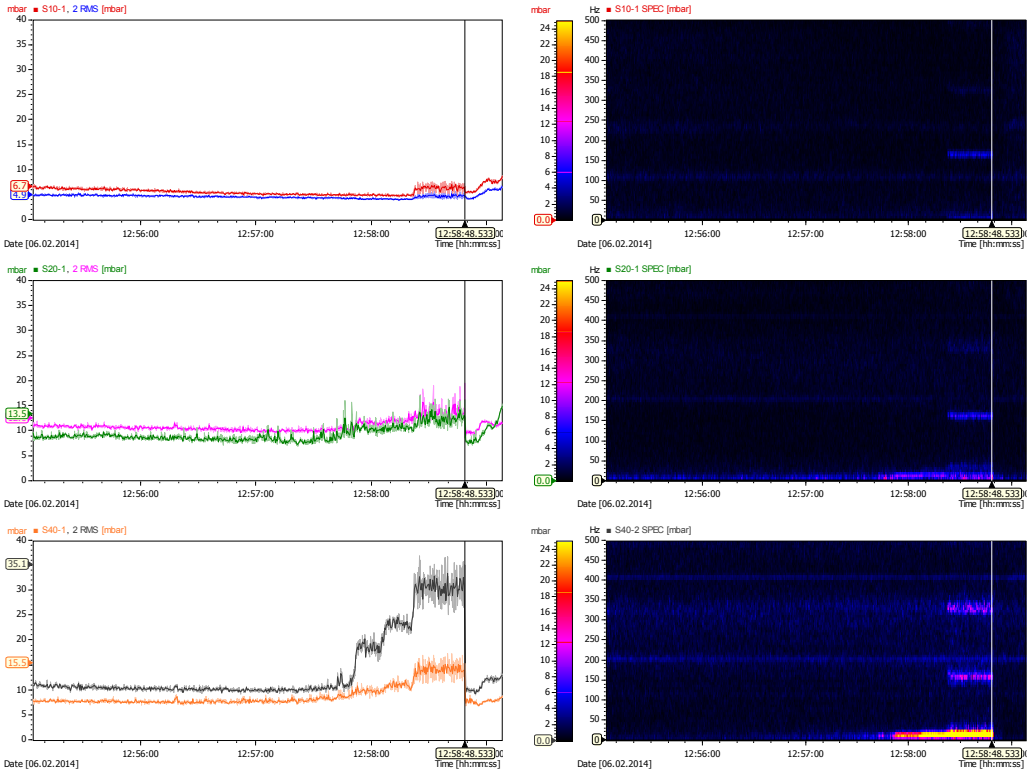

(b) Dynamic pressure as RMS signal (left) and power spectrum (right) at IGV = 20°

Figure 3.22: Dynamic pressure measured at section 10, 20 and 40 as raw time signal (a), RMS time signal and power spectrum (b), IGV = 20°

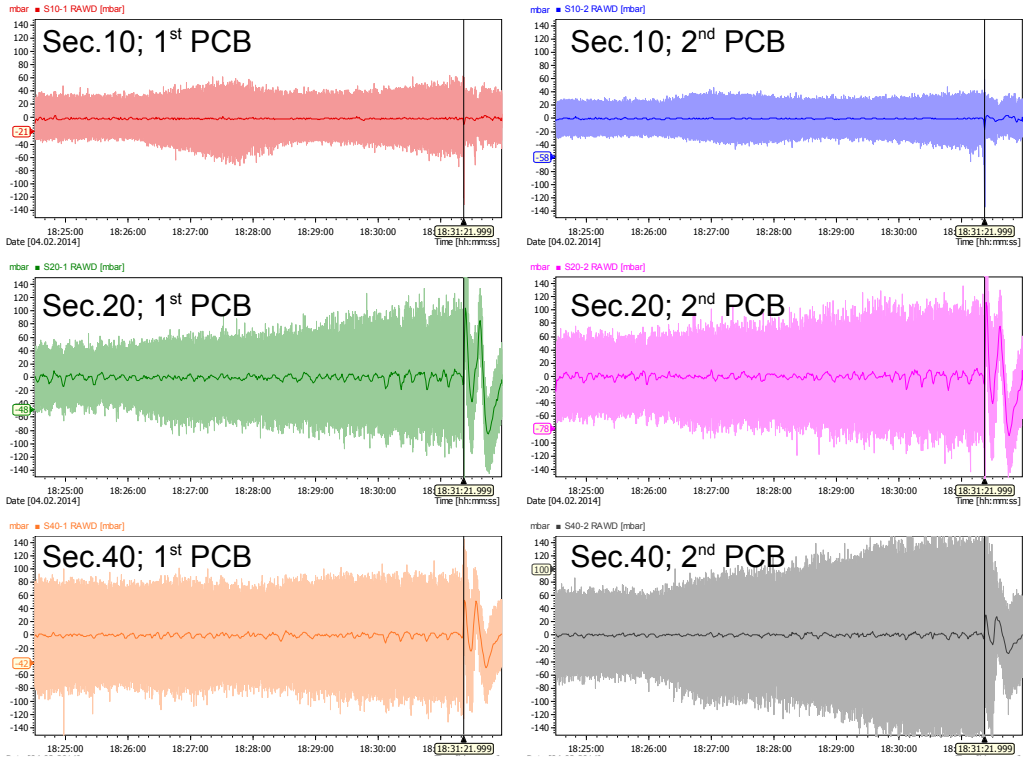

(a) Dynamic pressure raw signal in the time domain at IGV = 0°

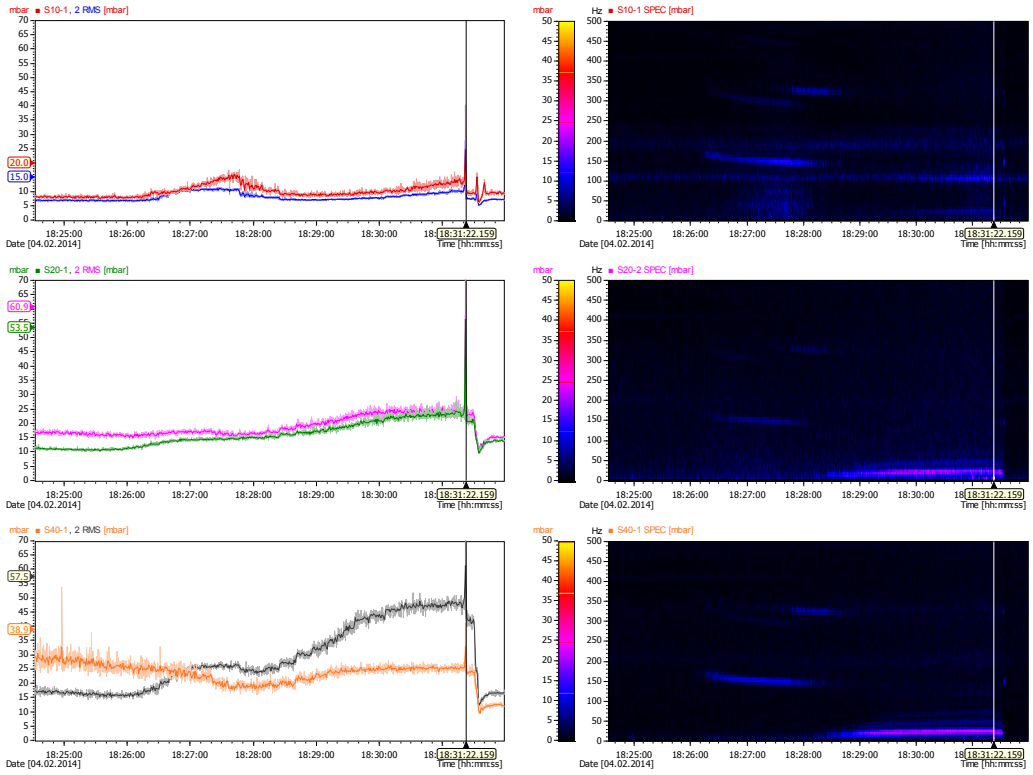

(b) Dynamic pressure as RMS signal (left) and power spectrum (right) at IGV = 0°

Figure 3.23: Dynamic pressure measured at section 10, 20 and 40 as raw time signal (a), RMS time signal and power spectrum (b), IGV = 0°

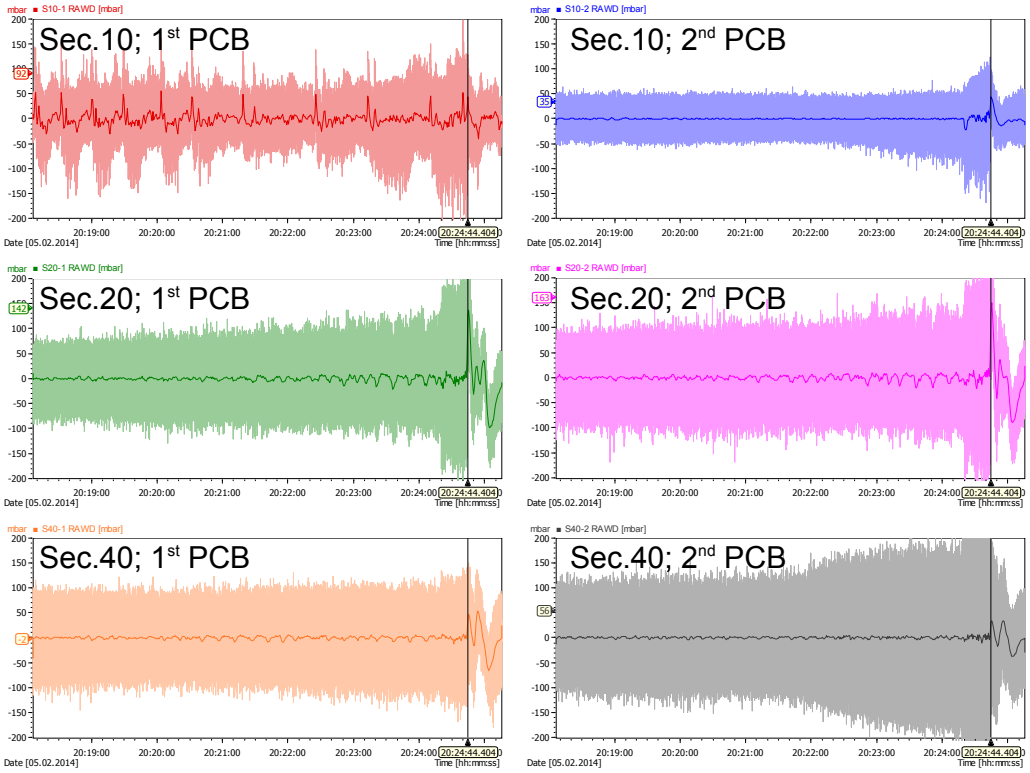

(a) Dynamic pressure raw signal in the time domain at IGV = -20°

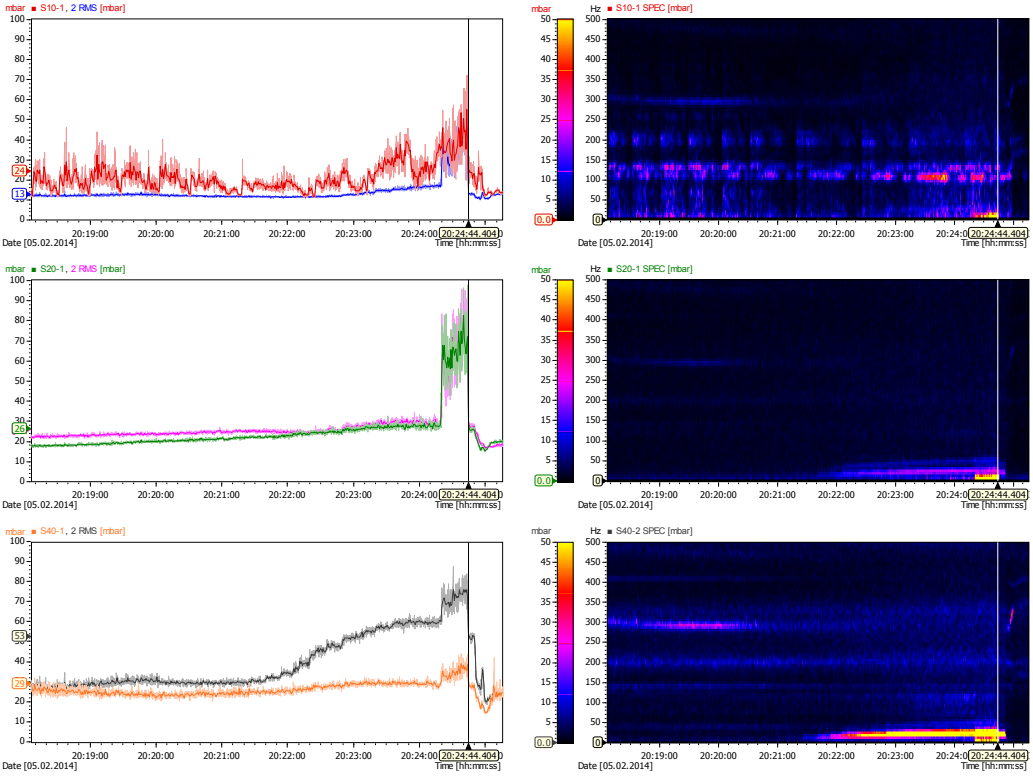

(b) Dynamic pressure as RMS signal (left) and power spectrum (right) at IGV = -20°

Figure 3.24: Dynamic pressure measured at section 10, 20 and 40 as raw time signal (a), RMS time signal and power spectrum (b), IGV = -20°

section 40, suggesting that the diffuser is always directly responsible for surge. In addition, when the surge starts, it is still the dynamic pressure signals at section 20 and 40 which firstly reach the anti-surge threshold, not the signals at section 10.

Based on the prevailing surge frequency of 25 Hz for all surge test cases at IGV = 60° , 20°, 0° and -20°, it can be concluded that the surge for this centrifugal compressor stage is merely dependent on the diffuser, not the IGVs. Although the two new IGV designs, type-B and type-C, are able to deliver improvements regarding inlet flow field and stage performance, their benefits can not surpass the flow instabilities caused by the diffuser stall. Therefore, type-B and type-C do not provide additional benefits in terms of surge margin expansion than what has been obtained by using type-A for the compressor stage.

3.8 Summary

This chapter illustrates the measurement results from the centrifugal compressor rotating test rig with the three different IGV configurations. The IGV rotating test campaign was carried out as a validation test for the unique cambered IGV and the multi-foil IGV compared their results to the baseline IGV. The measurement at the IGV plenum outlet shows that type-B and type-C are able to deliver more uniform flow fields for the impeller inlet section with less pressure losses at lower IGV setting angles, and more controlled swirl angle at higher IGV setting angles. The rotating test results are very consistent with the previous related static test and CFD prediction for the IGV plenum alone. While both new IGV configurations demonstrate clear improvement compared to the baseline, the multi-foil IGV (type-C) is found to be the best choice for keeping the largest reduction of pressure loss level, and the best linearity of swirl angle. The further investigation on the individual components at the impeller, diffuser, return channel and stage outlet shows that the initial benefits achieved by the unique cambered IGV and the multi-foil IGV can be preserved throughout the downstream components to the stage outlet, so that in combination a higher overall stage performance can be obtained. Especially for the test cases with the multi-foil IGV, the stage work coefficient and the stage polytropic efficiency can be increased by 2% at design point of IGV = 0°, which together contribute to an increase of 5% in the stage head coefficient. Regarding the off-design points at IGV = -20°, 20°, 40° and 60°, type-B and type-C also demonstrate significant potentials in delivering higher stage performance, although these benefits have to be mitigated in combination with the shifting effect of type-A at higher IGV setting angles due to its overturned flow. As the last part of rig result, the dynamic surge test is discussed based on the dynamic pressure measurement, from which all three IGV types are found to be nearly

identical in respect of their surge behaviors at IGV = -20°, 40° and 60° as well as rotating stall at IGV = 20°. The strong downstream disturbances, which can be detected by the dynamic pressure instabilities measured in the diffuser channel, suggests that the diffuser stall is the main cause for the surge of this centrifugal compressor stage. Therefore, the surge limit of the impeller stage cannot be directly influenced by the improved upstream flow fields provided by the two new IGV designs.

Chapter 4

CFD Simulations

In the previous chapter, the stage performance tests have shown that the two new IGVs, the unique-cambered IGV and the multi-foil IGV, are beneficial for the compressor stage performance improvements. After the rig test has been done, some questions still remain regarding the contributions of the new IGVs to the stage performance, for exmaple:

- What exactly are the flow mechanisms for the stage efficiency improvement?
- How does the inlet swirl/distortion interact with the impeller?
- How does the internal flow field in the compressor blade passages look like?

In order to find out the answer, in this chapter a series of CFD simulations are performed applying the experimental results from the previous test campaign. For the research and development of turbomachinery applications, the CFD simulation offers a quick way to look into the blade passages of a rotating machine, whereas from the experimental perspective it is often a tremendous effort to get access to the internal flow. On the other hand, the validation procedure by means of both experimental data and CFD prediction is often necessary for the optimization of CFD flow modeling. Specifically for the centrifugal compressor flow modeling, some relevant studies can be found in Hathaway [45][46], Menter [63], Smirnov [77], Yan [90], Zemp [93], Guidotti [43] and Funaba [35]. The synergism between experiment and CFD in the last decades has greatly accelerated the industrial development process and fundamental research of fluid mechanics.

This chapter of CFD study includes the simulation approach, the mesh model, the simulation setup and the CFD result discussion. As the study progresses, various simulation methods have been utilized as follows:

- Steady single-passage simulations;
- Steady full-annulus simulations;

- Transient full-annulus simulations;
- Transient blade row simulations.

These four different CFD techniques will be examined from simple to complex in order to examine different aspects of flow distortion, including inlet swirl direction, 360° non-uniformity and flow unsteadiness. Firstly, the steady single-passage simulation enables a quick turn-around of performance map reproduction. Secondly, the steady full-annulus model introduces the 360° flow non-uniformity to quantify the benefits of the flow uniformity contributed by the new IGVs for the centrifugal compressor. As a next step, the transient full-annulus simulations further take into account the flow unsteadiness along the circumferential direction, which best represents the compressor operation conditions in reality. Finally, the transient blade row simulations is considered as an attempt to check whether this new kind of "quasi-transient" method can spare the computation resource of the full 360° transient model.

4.1 Simulation Approach

The CFD simulations for this project were performed by ANSYS CFX® Version 15.0, which is a commercial CFD solver based on the finite-volume Reynolds Averaged Navier-Stokes equations (RANS). ANSYS CFX has been widely accepted as a commercial CFD solver in the applications of turbomachinery owing to its high robustness, computation efficiency, satisfying calculation accuracy and ability for parallelization.

For this numerical study, the two-equation $k-\omega$ model is chosen as the turbulence model used for all simulation cases studied. The reason for choosing the $k-\omega$ model is based on its robustness and wide acceptance by the industry. The modeling theory for the $k-\omega$ model is documented in Wilcox [87][88]. In addition, during the early phase of this CFD project a comparison was performed between the $k-\omega$ and SST model. It is found that both models yield comparable prediction results, and additionally the simulation with $k-\omega$ model is able to converge more quickly.

Figure 4.1 illustrates a sketch showing the simulation domain of the CFD computation. It starts from the impeller inlet section (section 10), extends further to the diffuser (section 20 and 40) and U-bend (section 41), and ends up at the position right before the return channel. In this way a very large mesh model including the IGV plenum with non-uniform IGVs inside, and the return channel with static vanes inside, can be spared.

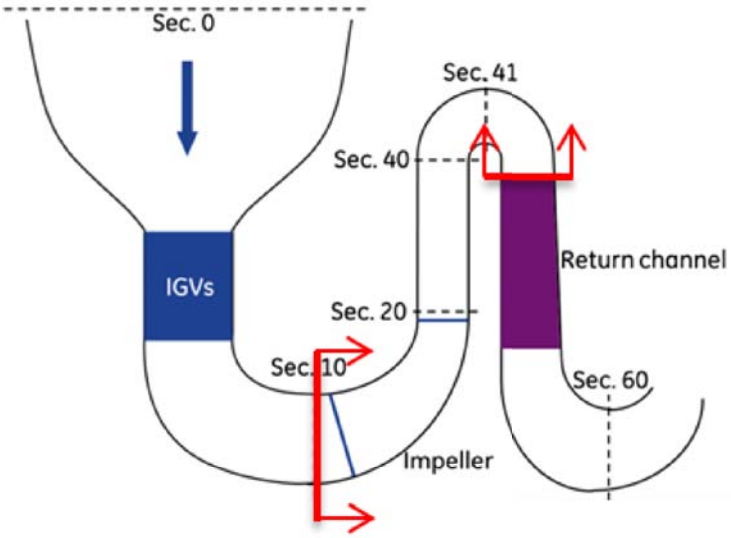

Figure 4.1: CFD simulation domain

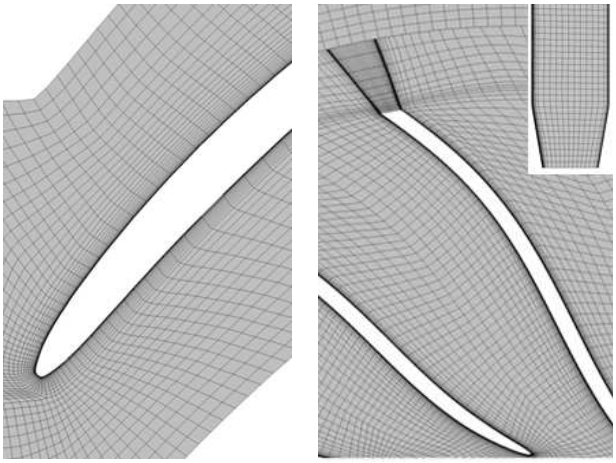

Figure 4.2: Midspan mesh fragments for the single-passage model (left) and the full-annulus model with exit contraction (right)

4.2 Mesh Model

Figure 4.2 presents the midspan fragments of the single-passage mesh model and the full-annulus mesh model. The exit area is imposed by an artificial contraction to avoid backflow, which is similar to the treatment in Smirnov [77]. The mesh grids for the impeller are generated by ANSYS TurboGrid® , which offers a quick mesh generation process for turbomachinery applications. The mesh grids for the diffuser and the U-bend are generated together as one block by ANSYS ICEM® .

Table 4.1 summarizes the main mesh statistics for the three mesh models (single-passage,

Table 4.1: Mesh statistics of CFD models (I: impeller; D: diffuser and U-bend as one block)

Type of Mesh Model	Mesh Size	Min. Orth. Angle [°]	y^+ [-]
Single-Passage (SP)	I: 1.1×10^6 D: 3.5×10^5	I: 27.9 D: 64.1	I: 1.5 D: 25
Full-Annulus (FA)	I: 4.3×10^6 D: 1.6×10^6	I: 33.0 D: 74.1	I: 4.5 D: 25
Transient Blade Row (FT-TBR)	I: 5.1×10^5 D: 1.8×10^5	I: 33.0 D: 74.1	I: 4.5 D: 25

full-annulus and transient blade row) adopted for the CFD study. A total of three different mesh models are applied for conducting the single-passage, full-annulus, and FT-TBR simulations throughout the CFD study. The single-passage model contains only one blade and one pitch width. The full-annulus model has an analogous topology, but coarser mesh grids per passage to keep a moderate total number of mesh grids. The transient blade row model requires only two blade passages instead of a full 360° full annulus while still taking into account the 360° inlet flow distortion and unsteadiness. The TBR model contains the identical mesh grids for each passage as the full-annulus model to be able to directly compare these two methods.

A mesh sensitivity study has been done to check the impacts of mesh size and resolution. During the sensitivity study, various single-passage models with different mesh number and y^+ level were tested. In addition, the full-annulus mesh model, which will be applied later, was also examined under the same boundary conditions. Figure 4.3 shows an example of the sensitivity result in the form of total pressure ratio. It can be seen that the coarse model with declined mesh size and y^+ results in a lower total pressure ratio, and the point for the last single-passage model with excessively coarse grids significantly deviates from the other cases. With consideration of convergence quality, prediction accuracy and

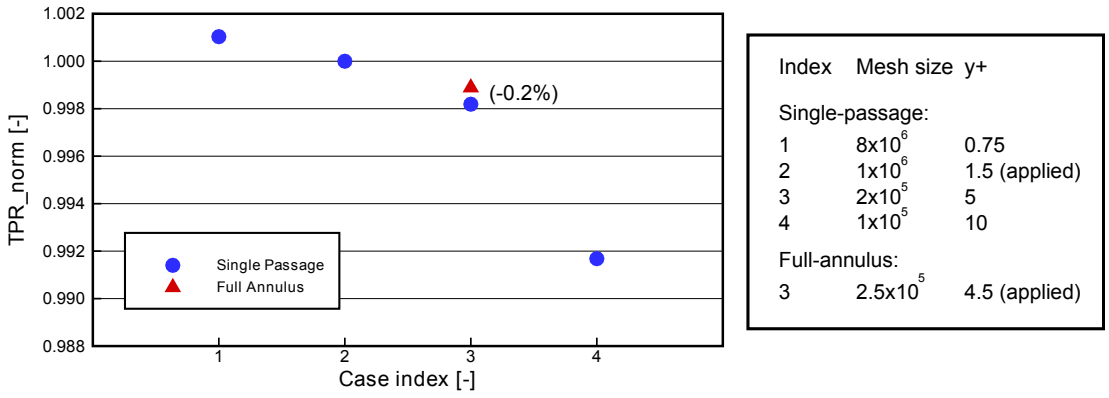

Figure 4.3: Mesh sensitivity study for the single-passage model and the full-annulus model

computation costs together, the single-passage mesh model with a size of about 1.1 million mesh grids and $y^+ = 1.5$ is chosen for this CFD study. For the full-annulus simulation, in order to keep the overall mesh size within a moderate range, the coarse model with the mesh size of 2.5×10^5 per passage and thus a total mesh size of 4.3×10^6 needs to be implemented. The sensitivity indicates that the impact of switching from the fine single-passage model to the coarse full-annulus model is about 0.2%.

4.3 Simulation Setup

This section introduces the simulation setup applied for the CFD study.

4.3.1 Single-Passage Model Setup

The $k-\omega$ model with automatic wall function is chosen as the turbulence model. The hub, shroud, and blade walls are defined as smooth, non-slip, and adiabatic walls. As required by the pitchwise periodicity of a single-passage model, the two side surfaces are defined as rotational periodical interfaces. Figure 4.4 shows the inlet boundary conditions for the single-passage model, including total pressure p_t, total temperature T_t and yaw angle. All inlet conditions are imposed in the form of 1-D profiles derived from the experimental data. Specifically, the 1-D inlet profiles are obtained by first averaging the measurement points at each radius along the 360° circumference and then interpolated in the radial direction. Since during the test campaign, all probe sensors at section 10 were distributed with equal-area distances, the 1-D profiles obtained by this way can be seen as "area-averaged" flow profiles. Due to the small distances between the probe sensors and the endwalls, the measured points do not contain the boundary layer flow in the vicinity of hub and shroud. To supplement the flow information in the boundary layer, two options might be considered. The first option is to insert an artificial boundary layer transition. This attempt was tested by Baumüller [8] yet associated with two drawbacks: (1) The CFD computation becomes very unstable due to strong tendency of flow separation on the inlet walls; (2) Requirement on the mesh density in the vicinity of endwalls is extremely high ($y^+ \approx 0.1$). The second option, which is adopted by this project, is to extrapolate the original interpolated profiles further up to the walls. The extrapolation is performed by the mathematic method "Piecewise Cubic Hermite Interpolating Polynomial (pchip)" in Matlab (more details can be found in Moler [65]). This yields very reasonable flow profiles at the inlet as indicated in Figure 4.4, and ensures a stable CFD computation.

To specify the turbulence level at the domain/impeller inlet, the turbulence intensity of

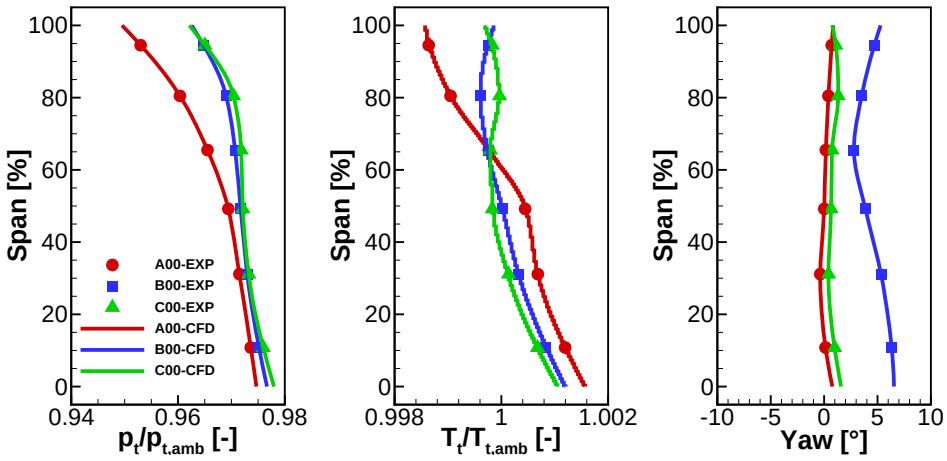

Figure 4.4: Inlet boundary conditions for the CFD simulation; shown are the measured flow profiles of total pressure, total temperature (both normalized by the ambient values), and yaw angle

$Tu = 7.7\%$ is applied as the level derived from the previous CFD prediction at section 10 with the IGV plenum alone. The turbulence intensity is defined as:

$$Tu = u^{'}/U \tag{4.1}$$

in which $u^{'}$ is the root-mean-square of the turbulence velocity fluctuations

$$u^{'} = \sqrt{\frac{1}{3}\left(u_x'^2 + u_y'^2 + u_z'^2\right)} \tag{4.2}$$

and U is the compound mean velocity

$$U = \sqrt{\left(U_x^2 + U_y^2 + U_z^2\right)} \tag{4.3}$$

The other turbulence parameter, the eddy viscosity ratio μ_t/μ at the impeller inlet, has to be estimated. It is set to 200 for this study based on the following estimation method.

In order to verify whether the combination of Tu and μ_t/μ is plausible, Figure 4.5 shows the database and the tendency curves of turbulence decay summarized by Bode [13] and the calculation points with $Tu = 7.7\%$ and three μ_t/μ options varying between 50 and 200. Only the value $\mu_t/\mu = 200$ matches with the measurement in Bode [13] when the inlet velocity ≈ 90 m/s, which is the case for the impeller operating at its design point. Therefore, the combination of $Tu = 7.7\%$ and $\mu_t/\mu = 200$ is applied.

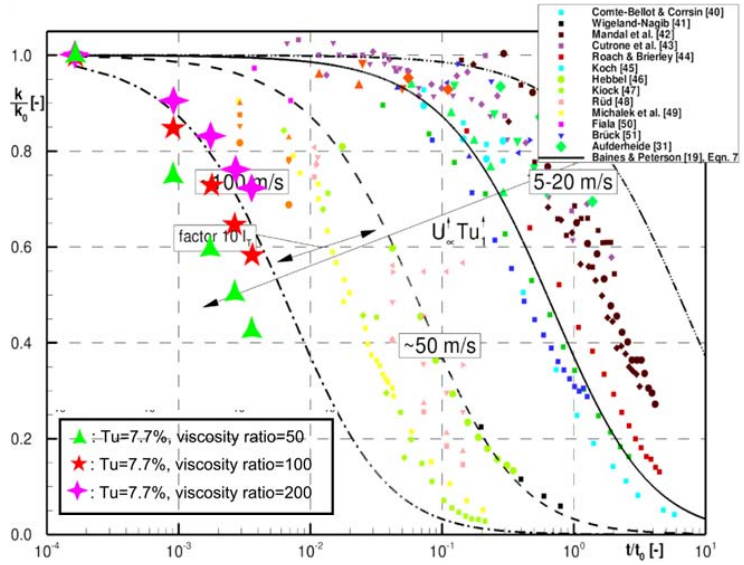

Figure 4.5: Turbulence decay of $Tu = 7.7\%$ and μ_t/μ from 50 up to 200 together with the experimental database from Bode [13]

For the single-passage model, the domain outlet is specified with the same mass flow value as previously measured.

4.3.2 Full-Annulus Model Setup

The full-annulus model is able to be specified with the complete 360° inlet flow conditions. The full-annulus model can be seen as a replica of each single blade passage by the blade number. Consequently, no rotational periodicity has to be defined across the neighboring blade passages. Figure 4.6 illustrates an example of inlet boundary conditions of total pressure (normalized) and yaw angle at design point. Since the diffuser is a vaneless channel, the rotor and stator can be combined together as one single domain by specifying the stator as "rotating", so that a rotor-stator interface can be avoided. Subsequently, the hub and shroud walls have to be specified as counter-rotating wall to be consistent with the movement of static parts in the rotating domain.

At the domain outlet, in contrast to the single-passage steady simulations, the mass flow rate at domain outlet as boundary condition was found to be unstable for the full-annulus model. To solve this problem, the outlet mass flow rate was substituted by the static pressure. In order to ensure the same mass flow rates, a proportional p_s controller has been created at the domain outlet in the form:

$$p_s^* = p_s + \Delta p_s = p_s + k \cdot (\dot{m} - \dot{m}_{\mathrm{EXP}}) \tag{4.4}$$

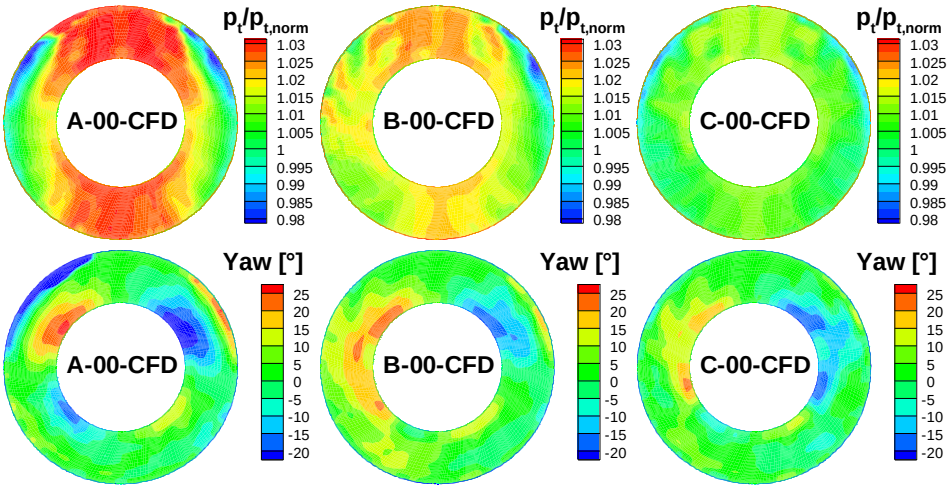

Figure 4.6: Example of 360° flow fields at domain inlet for the full-annulus model

in which the proportional ratio k is set to 5000 Pa/(kg/s) for the fine-tunning of setting static pressure. During the CFD computation for steady full-annulus cases, the adjustment is performed after each iteration by comparing the difference between the measured mass flow $\dot{m}_{\mathrm{EXP}}$ and the calculated mass flow $\dot{m}$. The adjustment continuous until the two values match, which can be reached mostly after 1/2 of the whole iteration steps. Later on, the static pressure value obtained from the steady full-annulus simulations can be further directly used without the controller for the transient and the TBR simulations.

For the later transient simulation with the full-annulus model, a constant time of 1/24 blade passing period (BP) is set as the time step. A first study on the time step was conducted with 1/12, 1/24 and 1/48 BP to monitor the time-varied signals. As an example, Figure 4.7 presents the transient total pressure signals at the monitoring points near the impeller leading edge and trailing edge in two periods after the time periodicity for each case is reached. It can be seen that the time step of 1/24 BP is able to deliver adequate time resolution.

4.3.3 Preliminary Check

A preliminary check has been performed in order to firstly validate the CFD setup before starting simulating the CFD cases for this project.

Objective of Preliminary Check

The objective for the preliminary check before starting the CFD simulations is to validate the CFD techniques applied for this study. The check has been done mainly for section

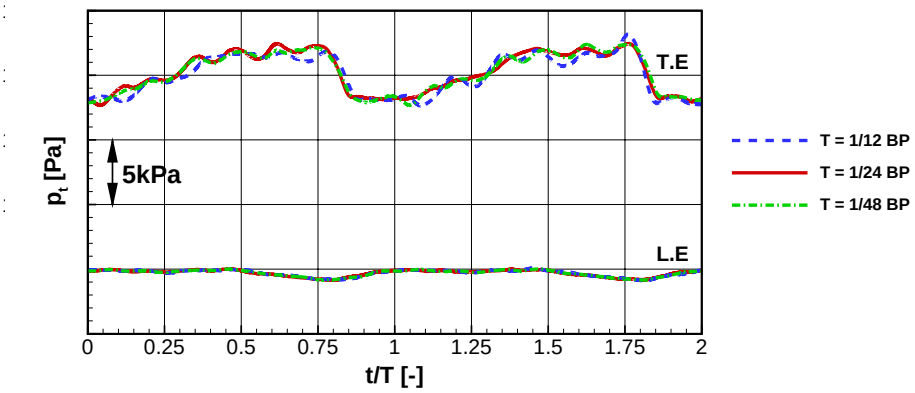

Figure 4.7: Total pressure at the Monitoring points near the impeller leading edge (below) and trailing edge (above) with comparison between the different time steps

10, which involves comparing the measured profiles collected at section 10 with the CFD results extracted at the location shortly downstream. Because the CFD results directly at section 10 would be exactly identical as the imposed inlet profiles, the area for extracting the CFD data is chosen to be located 2mm downstream from section 10, where the fluid has already passed the first layer of inlet mesh grids, so that the CFD response to the imposed inlet boundary conditions can be identified.

Check Procedure

The check procedure is conducted for the steady, single-passage model, the steady full-annulus model, and the transient full-annulus model at IGV = 0°, 20°, 40° and 60°. By performing the preliminary check it is found that for the same full-annulus model, the steady and unsteady CFD results regarding the flow fields at section 10 and 20 are nearly identical. Therefore for the later discussions, the flow fields from the steady full-annulus CFD results will be presented as the representatives for both steady and transient results. In addition, after the check on the sing-passage model it is found that two remedies (regarding the added pitch angle and yaw angle correction) must be made to improve simulation accuracy. To clearly demonstrate the improvements after adapting the remedies, the single-passage results (dashed lines in Figure 4.8) still use the original simulation setup, while the full-annulus results (full lines in Figure 4.8) are the results after the two corrections were made.

Preliminary Check Result

Figure 4.8 presents the results as the preliminary check of the averaged 2D flow profiles for the single-passage and full-annulus models near the domain inlet, for example at IGV = 0° and 60°. The CFD profiles are put together with the previous measurement points collected from the IGV rotating test campaign. The profiles include total pressure p_t, total temperature T_t, and yaw angle to be compared the direct sensor measurement, as well as static pressure p_s, absolute velocity c_{abs}, and circumferential velocity c_u to be compared with indirect data after post-processing of sensor readings. The measurement points of p_t, T_t, yaw angle and p_s were measured by the Kiel, TC and 3-hole probes, while p_s contains additional points from static pressure taps on the hub and shroud. As during the test campaign all probe heads were traversed to obtain a full 360° flow mapping, all measurement points as 2D profiles shown in Figure 4.8 are the points after a circumferential averaging.

Two important findings are discovered by the preliminary check. Firstly, it is found that the yaw angle alone is not enough for setting up the inlet flow direction, and must be combined with an additional pitch angle. Although the centrifugal compressor stage adopted by this project merely has an axial inlet at section 10 and thus the pitch angle at section 10 should be very small, it has still a clear impact on the CFD simulation. The reason can be explained by the sketch in Figure 4.9. The axial inlet of the real stage contains two slightly inclined angles γ_{hub} and γ_{shr} on the hub and shroud walls. This feature is maintained in the mesh model at the impeller inlet, so that the inlet section of the CFD model is not exactly perpendicular the machine axis. Therefore, if there is no pitch angle defined at the inlet, the oncoming flow, which is parallel to the machine axis, would impinge on the hub wall surface, and thus would cause a reverse flow region near the shroud wall. The negative impact can be identified by the static pressure profiles p_s at IGV = 0° in Figure 4.8, in which the dash curves have implausible "S-shaped" profiles near the hub and shroud walls for type-B and type-C. In order to correct this, the pitch angle has to be added as part of the definition of inlet flow direction. Since during the experimental test only 3-hole probes were applied at section 10, the pitch angle γ for the CFD simulation has to be assumed. For this CFD study it is assumed as a linear relationship to the radius r:

$$\gamma = \gamma_{hub} + (\gamma_{shr} - \gamma_{hub}) \cdot \frac{r - r_{hub}}{r_{shr} - r_{hub}} \tag{4.5}$$

Subsequently, the axial, radial and circumferential flow velocity components c_{ax}, c_r and c_u have to be recalculated based on the measured total temperature T_t, total pressure p_t

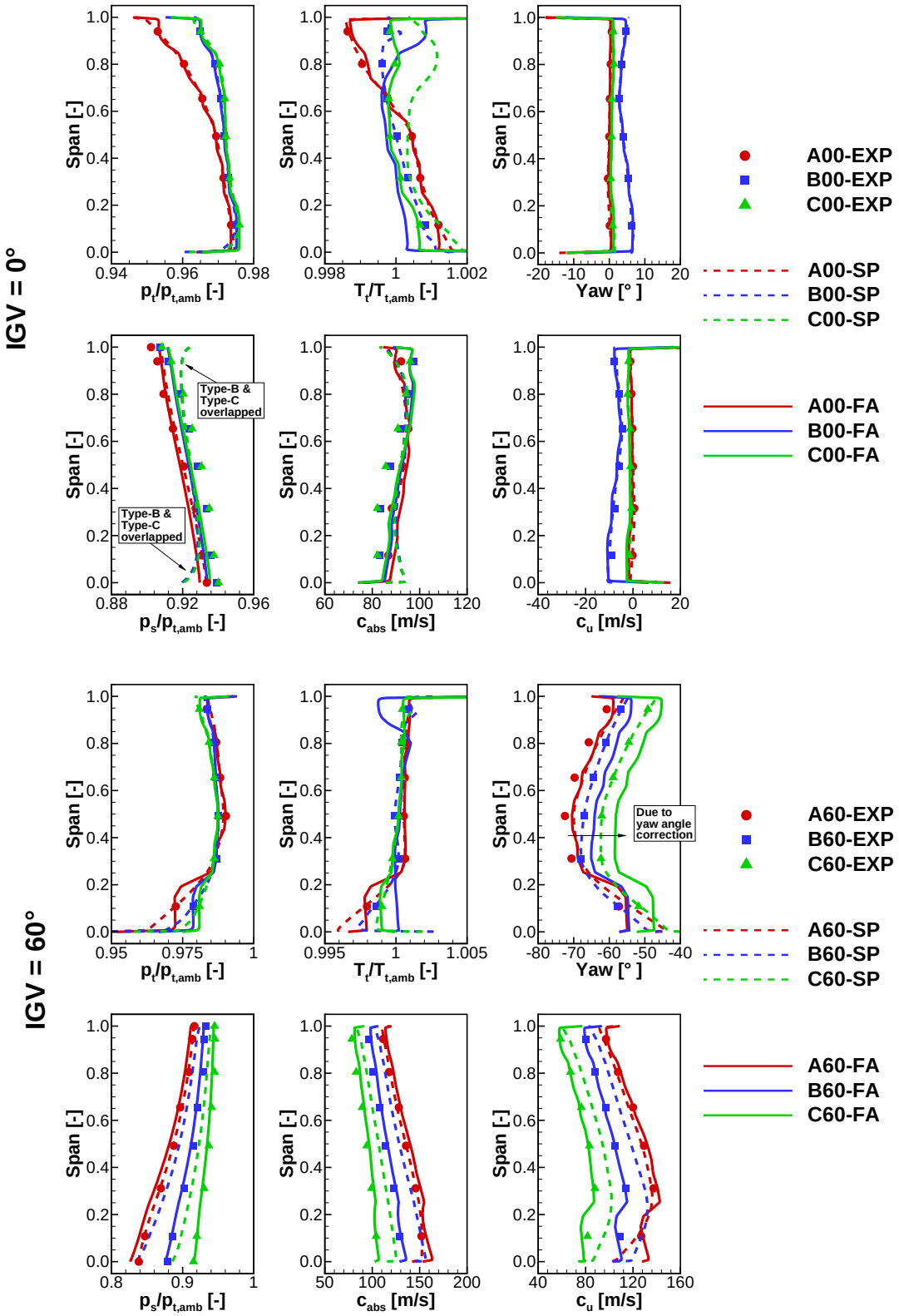

Figure 4.8: Preliminary check of the 2D flow profiles near domain inlet at IGV = 0° and 60°; shown are the experimental points (EXP), and the CFD profiles using single-passage (SP) and full-annulus (FA) model

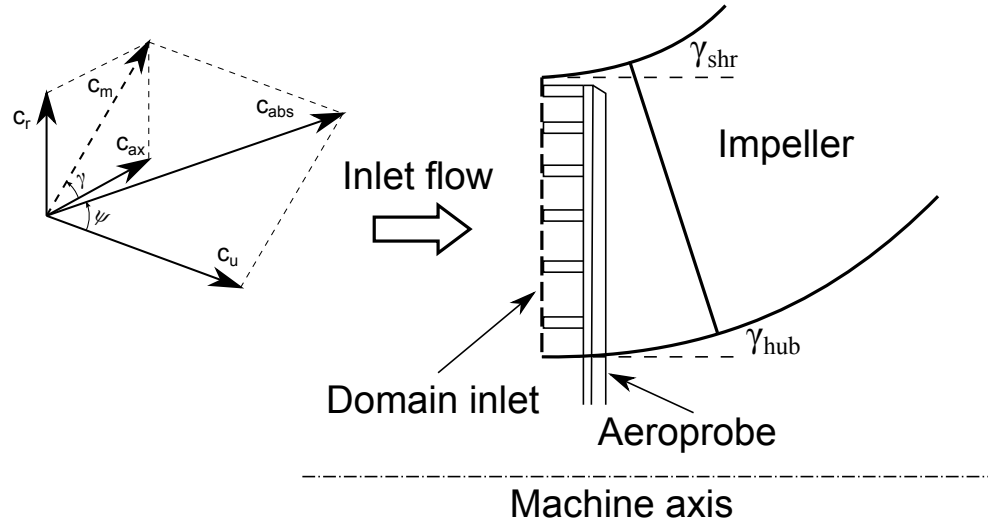

Figure 4.9: Velocity triangle as the inlet flow direction of CFD boundary conditions (left), together with the sketch of the impeller inlet section; γ: pitch angle; ψ: yaw angle

and static pressure p_s, as well as the pitch angle γ and yaw angle ψ as:

$$T_s = T_t / \left(\frac{p_t}{p_s}\right)^{\frac{\kappa-1}{\kappa}} \tag{4.6}$$

$$Ma = \sqrt{\frac{2}{\kappa - 1} \cdot \left(\frac{T_t}{T_s}\right) - 1} \tag{4.7}$$

$$c_{abs} = Ma \cdot \sqrt{\kappa R T_s} \tag{4.8}$$

$$c_{ax} = c_{abs} \cdot \cos\psi \cdot \cos\gamma \tag{4.9}$$

$$c_r = c_{abs} \cdot \cos\psi \cdot \sin\gamma \tag{4.10}$$

$$c_u = c_{abs} \cdot \sin\psi \tag{4.11}$$

The second finding is that at the higher IGV setting angles at IGV = 40° and 60°, the absolute level of yaw angle measurement at section 10, which was previously documented in Chapter 3, was not accurate up to a maximum deviation of 4° or $\Delta = 6.7\%$ at IGV = 60°. The reason for the inaccuracy is that during the rig test preparation, all 3-hole probes were turned facing to the presumed oncoming flow direction, not the real flow direction. For example at IGV = 60°, all the probes were turned to be 60° offset from the axial direction. If the actual swirl angle does not stay within a certain range around 60°, the measurement accuracy would be deteriorated due to the less accurate extraplolation of calibration. The existence of such an inaccuracy can be proved by the recalculation of mass flow rate at section 10 based on the yaw angle measured, and then comparing the

value with the total mass flow rate measured by the inlet venturi. The latter value has high degree of accuracy ($\Delta = 1\%$) based on the certified calibration. By this method an offset of yaw angle up to 4° at IGV = 60° can be detected. Therefore, the yaw angle at higher IGV setting angles must be corrected by a counter offset value. After the yaw angle is properly corrected, the CFD simulations are able to yield significantly improved static pressure p_s and velocity predictions (c_{abs} and c_u). As illustrated in Figure 4.8, these improvements can be demonstrated by the close agreements between the full lines and the measurement points in Figure 4.8 at IGV = 60°.

These preliminary check results show that the CFD simulation can be successfully performed only by incorporating these two remedies (pitch angle and the yaw angle offset), so that the predicted flow profiles are in line with the prescribed inlet conditions.

4.4 Numerical Simulation Result

This session covers the CFD simulation results for the three IGV groups.

4.4.1 Steady Single-Passage Simulation Result

Figure 4.10 presents the impeller performance parameters predicted by the steady single-passage model, which includes: (a) impeller total pressure ratio Π_t; (b) impeller work coefficient τ; (c) impeller polytropic efficiency η; and (d) impeller head coefficient h. The parameters of Π_t, τ, η, h and the flow coefficient ϕ are defined by Equation 2.9, 2.12, 2.10, 2.13 and 2.16. In the early phase of the CFD study, it was found that the simulations at IGV = -20° failed to converge due to large flow instability imposed by the counter-rotating swirl working against the impeller rotating direction. In addition, the simulations at the last near-surge operation points failed to converge due to the early surge predicted by CFD. Therefore, Figure 4.10 contains the CFD results at IGV = 0°, 20°, 40° and 60° while omitting these instable conditions.

Impeller Total Pressure Ratio

Figure 4.10-(a) shows that the CFD results generally agree with the measurement well in respect of the predicted total pressure ratios. At IGV = 0° the CFD results have only a minor over-prediction by $\Delta = 1.3\%$. This small over-prediction probably results from the neglected loss effects due to the simplification of the CFD modelling and the steady-state conditions. Starting from IGV = 0° up to 60°, the over-prediction gradually

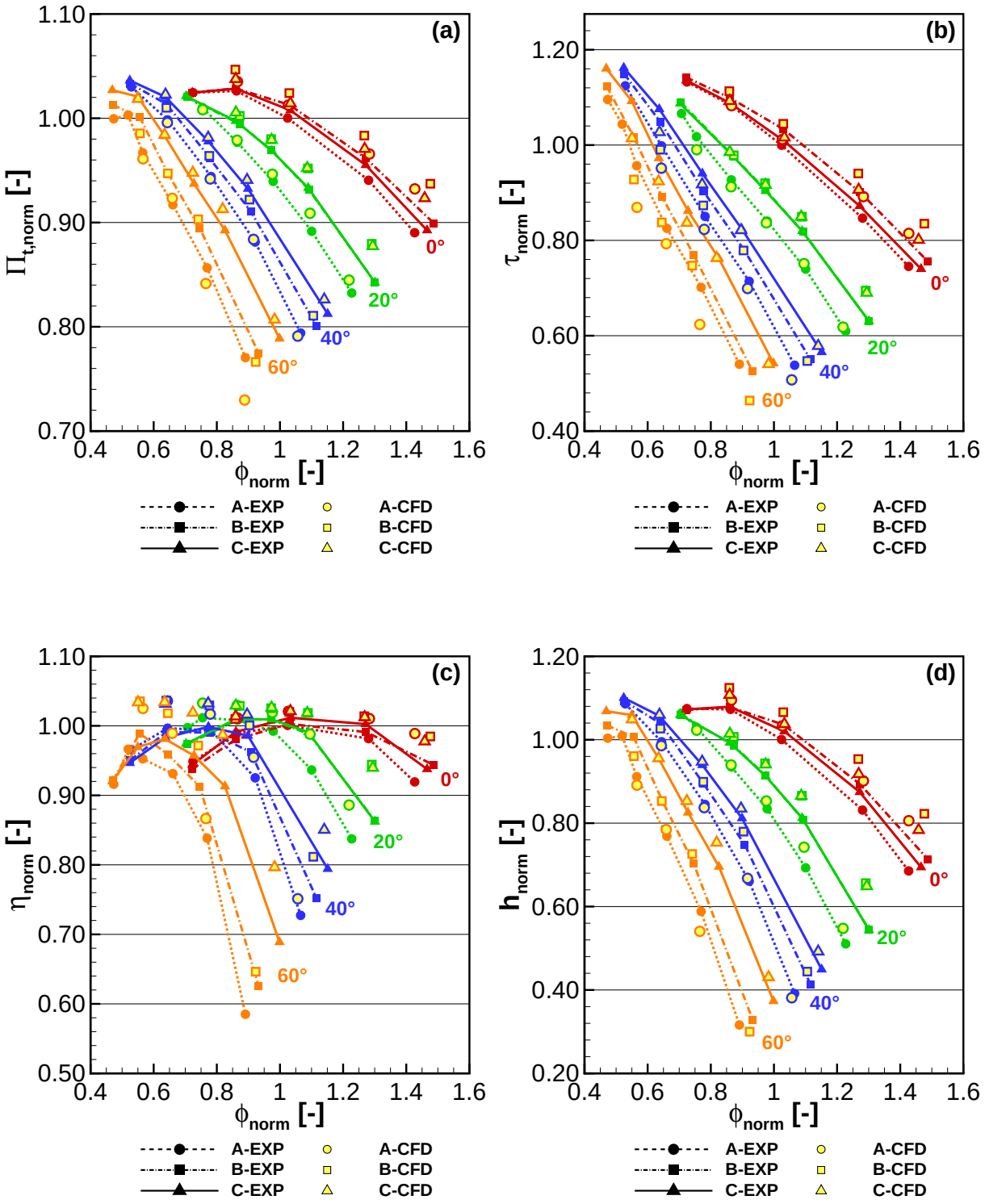

Figure 4.10: Impeller performance predicted by the steady, single-passage simulation; shown are: total pressure ratio Π_t, work coefficient τ, polytropic efficiency η and head coefficient h. All values are normalized by the design point for type-A at IGV = 0°

decreases until at IGV = 60° the CFD results almost overlapp the measurement points. It indicates that at larger IGV setting angles where the inlet flow incidence largely deviates from the optimal direction for the impeller blades, the incidence deviation causes the CFD simulation to response very sensitively. This is comparable to the previous finding that the CFD simulations failed to converge at near-surge conditions. At off-design points, the quality of CFD prediction is deteriorated due to even-worse inlet flow conditions.

In addition, it can be seen from Figure 4.10-(a) that at most simulation cases including all the speedlines at IGV = 20°, 40° and 60°, CFD is capable of predicting correct relative levels of total pressure ratios for the three IGV types. Only at IGV = 0°, the slight changes of less than 1% between type-A and type-B can not be clearly distinguished by CFD, suggesting that the minor improvements created by type-B at IGV = 0° are still within the precision range due to measurement inaccuracy and simulation inaccuracy.

Impeller Work coefficient

Figure 4.10-(b) shows the predictions of the impeller work coefficients. At IGV = 0° and 20°, the CFD results match up with the experiment well ($\Delta = 0.8\%$ at IGV = 0° and $\Delta = 1.6\%$ at IGV = 20°). However at IGV = 40° and 60°, the CFD results have clear under-predictions of work coefficient levels (e.g. $\Delta = 6\%$ at the nominal point, IGV = 60°). The under-predictions may due to two reasons: Firstly, the simplified CFD model does not contain cavity flow, flow leakage and friction between the impeller and the rotating shaft. This would cause the energy consumption for the compression process to be under-estimated than the reality Guidotti [42]; Secondly, the side-walls of the CFD model are defined as adiabatic walls, however, in practice the real stage still contains certain heat losses mainly in the form of heat conduction from the hotter compressor to the colder environment. Therefore, the CFD calculations are based on the flow conditions with less energy consumption and without heat conduction losses, which would lead to the under-predicted work coefficient level. Due to the increased loss and dissipation effects at off-design points and higher IGV setting angles, the differences of work coefficients between CFD and experiment become more pronounced at these conditions.

Impeller Polytropic efficiency

Due to the over-prediction of total pressure ratio Π_t and the under-prediction of work coefficient τ as discussed before, the polytropic efficiency η is expected to be largely over-predicted as depicted in Figure 4.10-(c). This is because the total pressure ratio is the scale for the compression capability (output), while the work coefficient is the scale for

the energy consumption (input). By combining the two aspects, the output-input ratio η describes how efficient a compressor can work. The over-prediction is particularly large at the near-surge locations and higher IGV setting angles where the polytropic efficiency levels are unreasonably high due to very low work coefficient values.

Impeller Head Coefficient

In Figure 4.10-(d), the head coefficients h generally reach good agreements with the measurement points (e.g. $\Delta = 3.5\%$ at IGV = 0° and $\Delta = 1.3\%$ at IGV = 60°). This is mainly contributed by the cancel-out effects between the over-predicted polytropic efficiency η and the under-predicted work coefficient τ especially at higher IGV setting angles, which are combined as the head coefficient $h = \tau \cdot \eta$.

Prediction at Off-Design Points

Due to the introduction of adjustable IGVs, the conventional terms of "design point" and "off-design point" have been mixed together since variable IGVs are able to shift the operation range completely to the left or to the right by imposing pre- or counter-swirl. The fact that type-A, type-B and type-C have their own individual "new design points" (defined as nominal points) at the same higher IGV setting angles, which were detected from the experiment in the previous chapter, makes a comparison between the three IGV types more complicated. Therefore, this session gives an explanation about the function of IGVs for the operation range expansion, and shows several relating flow fields at design and off-design points obtained by the single-passage CFD simulations.

To illustrate the process, Figure 4.11 shows a sketch to explain the function of using variable IGVs to recover the impeller performance at off-design points. In this simple sketch the labels for type-C stand for both IGV types type-B and type-C. Initially at IGV = 0°, the operation range of the compressor stage is constrained by a single speedline at IGV = 0°. Because at 0° IGV setting angle there is still no pre-swirl effect existed, the major differences in the stage performance should origin from the different levels of flow uniformity. The improved flow uniformity realized by type-B and type-C is the contributor for the efficiency increase at design point, as shown in Figure 4.11-(a) as C_{DP} vs. A_{DP}. Subsequently, as the mass flow rate decreases, the operation point moves to the left along the speedline, until it reaches its left limit at near-surge condition (Figure 4.11-(b)). At the left limit, the deviation of inlet flow incidence due to the decrease in the mass flow rate becomes so large that a large suction-side flow separation has to occur, as shown previously in Figure 2.3. As a consequence, the compressor stage will reach its

left limit near surge A_{LL} vs. A_{DP} in Figure 4.11-(b). After the IGV stage is installed, an appropriate incidence angle at lower mass flow rates can be obtained to generate optimum stage performance again, so that the speedline can be further shifted to the left region. From the previous experimental results, it is already known that the actual level of flow turning is not identical to the level of IGV setting angle, and type-A has an over-turned level of swirl angle. This leads to the real optimal operation point of type-A at IGV = 40° and 60° to be shifted more to the left than type-B and type-C. Therefore, it is an inappropriate comparison between type-A and other two IGV types due to the shifting effect at higher IGV setting angle. Figure 4.11-(c) indicates the operation range expansion of the stage obtained by the IGVs as A_{LL} vs. C_{NP}.

The function of IGVs for correcting the flow incidence can be visualized by Figure 4.12, in which the midspan contours and the streamwise velocities are shown for the conditions discussed above. From the left two plots Figure 4.12-(a) and (b), it can be seen that at IGV = 0°, the flow conditions for type-A and type-C are very similar. In both cases the inlet flow incidence is able to stay in line with the camber line of the impeller blade at the leading edge. After the mass flow rate decreases as shown in Figure 4.12-(b), the incidence deviates from the designed direction to be inclined towards the blade pressure side, which yields a likelihood for a flow separation on the blade suction side (Figure 4.12-(c)). This off-design behavior can be corrected by using IGVs, e.g. type-C with a setting angle of 40° as shown in Figure 4.12-(d). In this way the suction-side flow separation is suppressed, and thus the compressor performance is recovered.

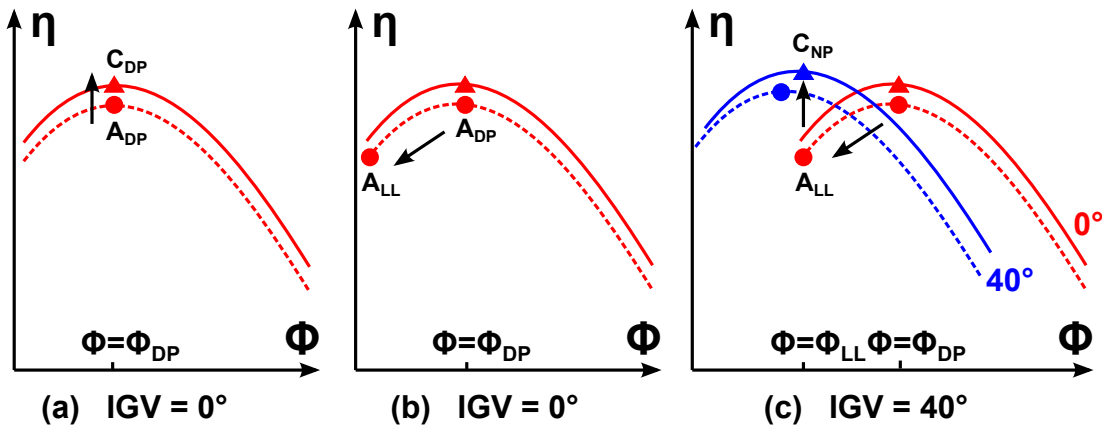

Figure 4.11: Analysis of the IGV impact by comparison of: (a)type-A and type-C at DP, IGV = 0°; (b) type-A at DP and type-A at last left point (LL), IGV = 0°; (c) type-A at last left point (LL), IGV = 0° and type-C at IGV = 40°

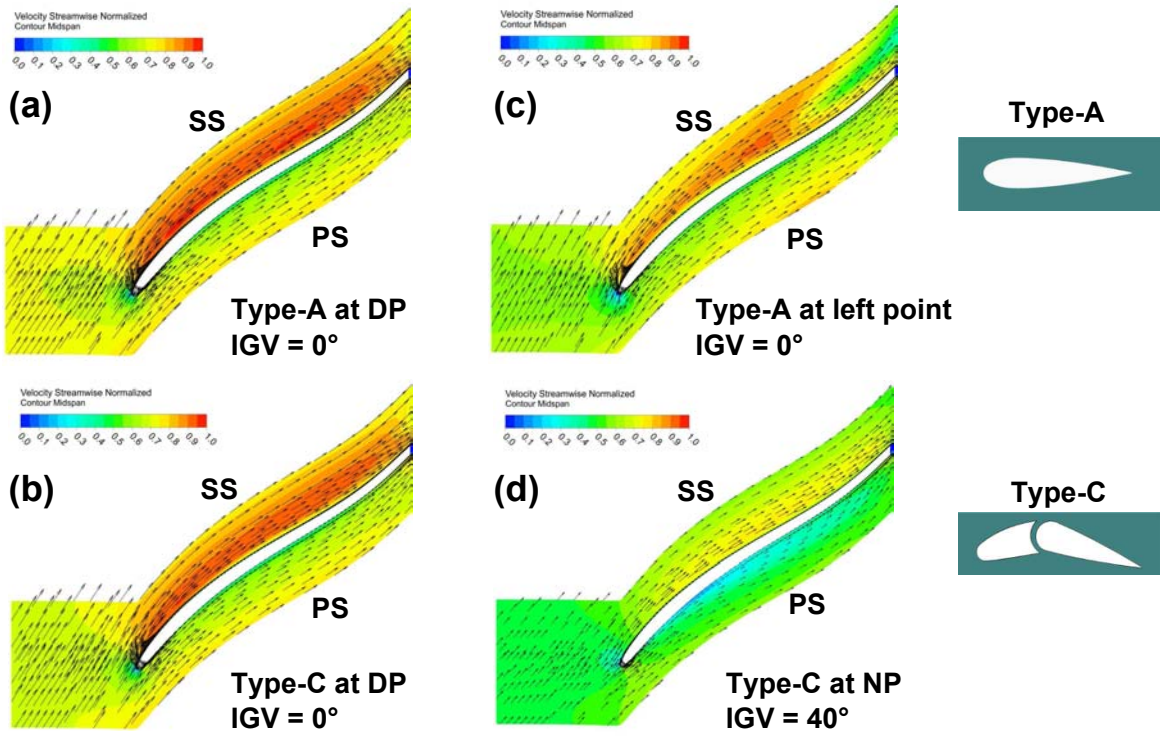

Figure 4.12: Midspan contours and vectors of streamwise velocity (normalized) for type-A and type-C; shown are the CFD results for type-A and type-C at design point and IGV = 0°, type-A at the left limit and IGV = 0°, as well as type-C at the nominal point and IGV = 40°

4.4.2 Steady Full-Annulus Simulation Result

The full-annulus CFD simulations offer an improved simulation method to use the complete 360° non-uniform flow field as the inlet boundary conditions. Consequently, the impact of flow non-uniformity can be quantified by the change of impeller performance parameters compared to the single-passage results.

Impeller Overall Performance

Figure 4.13 shows the impeller total pressure ratio Π_t and the impeller work coefficient τ as the full-annulus CFD results together with measurement and the single-passage CFD results. In Figure 4.13-(a), the levels of full-annulus total pressure ratios are noticeably lower than the predictions made by the single-passage model. In addition to the changes due to the new mesh model (0.2%), the extra differences is expected to origin from the 360° flow non-uniformity at the impeller inlet, which would induce further inhomogeneous flow fields in the blade passages and thus deteriorate the impeller performance. In Figure 4.13-(b), the work coefficient levels are nearly the same as the single-passage results at lower IGV setting angles. Only at IGV = 60° , the type-A case has a large deviation

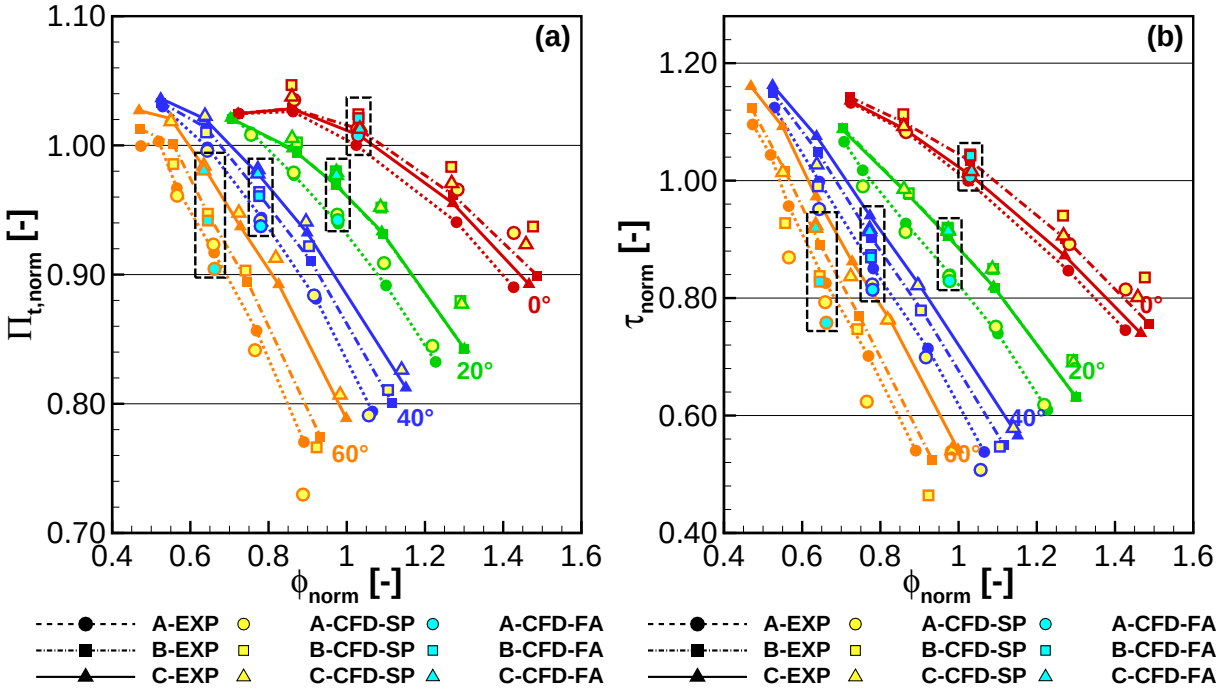

Figure 4.13: CFD results of impeller total pressure ratio and work coefficient (normalized); shown are the results predicted by the single-passage (SP) and full-annulus (FA) models in comparison with experimental points

between the single-passage and full-annulus CFD results, which indicates that under the large over-turned inlet flow angle, the impeller performance is even more sensitive to the 360° flow distortion existing in the largely non-uniform inlet flow.

To examine the impact of 360° flow non-uniformity more clearly, Figure 4.14 focuses on the impeller performance at design point of the three IGV types. Since at the design point all three IGV types have comparable magnitude of flow turning, the predicted differences in impeller total pressure ratio, impeller work coefficient and impeller polytropic efficiency are mainly associated with the 360° flow non-uniformity. For all three IGV types, the full-annulus CFD results always have lower predicted levels than the single-passage results, and thus are closer to the experimental results. It can be additionally seen that the differences for type-A are larger than type-B and type-C, which is consistent with the previous finding that the flow field at section 10 for type-A at IGV = 0° has the largest level of flow non-uniformity. In order to quantify the impact of flow non-uniformity, Table 4.2 summaries the relative values of impeller performance parameters $\Pi_{t,\mathrm{norm}}$, τ_{norm} and η_{norm}. It is clear that for all performance parameters, the group of full-annulus simulations has uniformly lower levels compared to the group of single-passage simulations. The levels of performance decline are beyond the range caused by the switch of mesh models (0.2%),

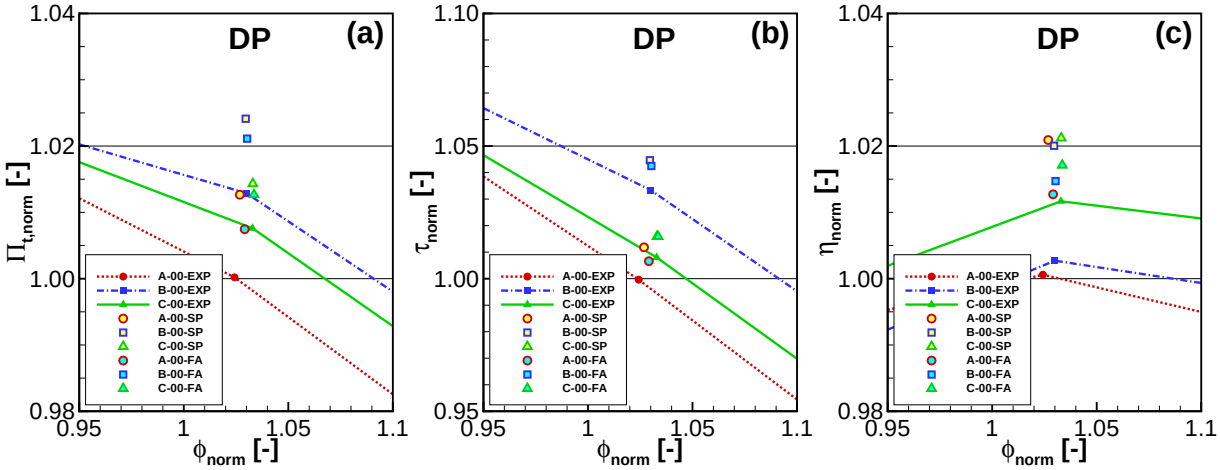

Figure 4.14: Comparison between experiment, single-passage and full-annulus CFD results at design point; shown are impeller total pressure ratio (a), impeller work coefficient (b) and impeller polytropic efficiency (c)

Table 4.2: Comparison of impeller performance parameters between single-passage and full-annulus CFD results at design point

	$\Pi_{t,\mathrm{norm}}$		τ_{norm}		η_{norm}	
A00-SP	1.0127		1.0119		1.0209	
A00-FA	1.0072	(-0.55%)	1.0064	(-0.45%)	1.0128	(-0.81%)
B00-SP	1.0241		1.0447		1.0200	
B00-FA	1.0212	(-0.29%)	1.0425	(-0.22%)	1.0147	(-0.53%)
C00-SP	1.0144		1.0162		1.0212	
C00-FA	1.0124	(-0.20%)	1.0162	(0%)	1.0172	(-0.40%)
Experiment	1.0000		1.0000		1.0000	

and thus reflect the additional effects of 360° inlet flow non-uniformity. Specifically for type-A, the total pressure ratio Π_t decreases by 0.55%, the work coefficient τ drops by 0.45% and the polytropic efficiency η by 0.8%, while for type-B and type-C, the Π_t ratios have less decreases by 0.2% to 0.29%, the τ levels decrease up to 0.22%, and the efficiencies η by 0.53% and 0.4%. The less decreases for type-B and type-C are likely ascribed to the more homogenious flow fields they have created, so that the differences between single-passage and full-annulus model are not as profound as type-A.

Therefore, the steady full-annulus simulation results show that the predicted performance is closer to the experiment, yet the levels of performance parameters are still over-predicted. As a consequence, it would be valuable to further investigate the unsteady effects using the transient simulations.

Impeller Flow Development

Figure 4.15 to 4.18 present the contour plots of the full annulus simulation results at the midspan section for the CFD cases at IGV = 0° and 60°. To save space the contour plots are limited to one quarter of the full annulus area, from which the circumferential variations can be already identified. A total of three physical parameters are included: the total pressure ratio (TPR), the streamwise velocity, and the specific entropy s. The total pressure ratio quantifies the rise of total pressure from the impeller inlet to the outlet. The streamwise velocity contours describe the flow patterns of the internal flow in the blade passages. The specific entropy can be used to identify the generation of losses due to dissipation.

IGV = 0° (Figure 4.15): The three IGV types show very little differences in the development of total pressure ratios. Only type-A shows a slightly delayed compression located in the upper blade passage. This is consistent with the "hot spots" in the following contours of streamwise velocity and static entropy. Especially in the entropy plots, only type-A contains two spots of high levels, indicating the suction-side flow is more energized than the test cases for type-B and type-C. Since all the three IGV types have very similar levels of averaged yaw angle, the improvements are ascribed to the improved flow uniformity provided by type-B and type-C.

IGV = 20° (Figure 4.16): Type-B and type-C begin to demonstrate certain benefits in achieving higher total pressure ratios. At IGV = 20°, they have almost the same flow field inside the blade passages due to their similar inlet conditions. This is consistent with the previous finding that the 20° speedlines for type-B and type-C almost completely overlap

with each other. For type-A, its reduced total pressure level is associated with its large flow non-uniformity in the circumferential direction across the adjacent blade passages, which further leads to large velocity variations. Especially one of the blade passages on the top reveals an almost negligible flow increase on the suction side, which indicates the impeller does not have an uniform compression along the circumference.

IGV = 40° (Figure 4.17): While at 0° and 20° the three IGV types have similar performance, they begin to deviate at IGV = 40° regarding the compression. For the first time, type-C delivers a clearly higher total pressure ratio than type-B. Compared to the previous results at IGV = 0° and 20°, the influence of incidence deviation on the impeller at the leading edge becomes evident. For type-A since the inlet flow is deviated, the flow separation firstly occurs on the pressure side. For type-B and type-C, such a pressure-side separation is prevented by a corrected inlet flow direction, which facilitates a continuous total pressure development in the blade passages downstream. The static entropy contours confirm the pressure-side separation for type-A, and the stepwise improvements generated by type-B and type-C. IGV = 40° cases can be seen as the starting point where the deviations in the flow incidence for type-A lead to a declined impeller performance.

IGV = 60° (Figure 4.18): The deviations of the three IGV types further amplify at IGV = 60°. For type-A, the deviations are reflected by a large delay of total pressure rise, strong flow deceleration, local flow separation and intense entropy generation. This pressure-side flow separation can be significantly suppressed by type-B, and even completely eliminated by type-C.

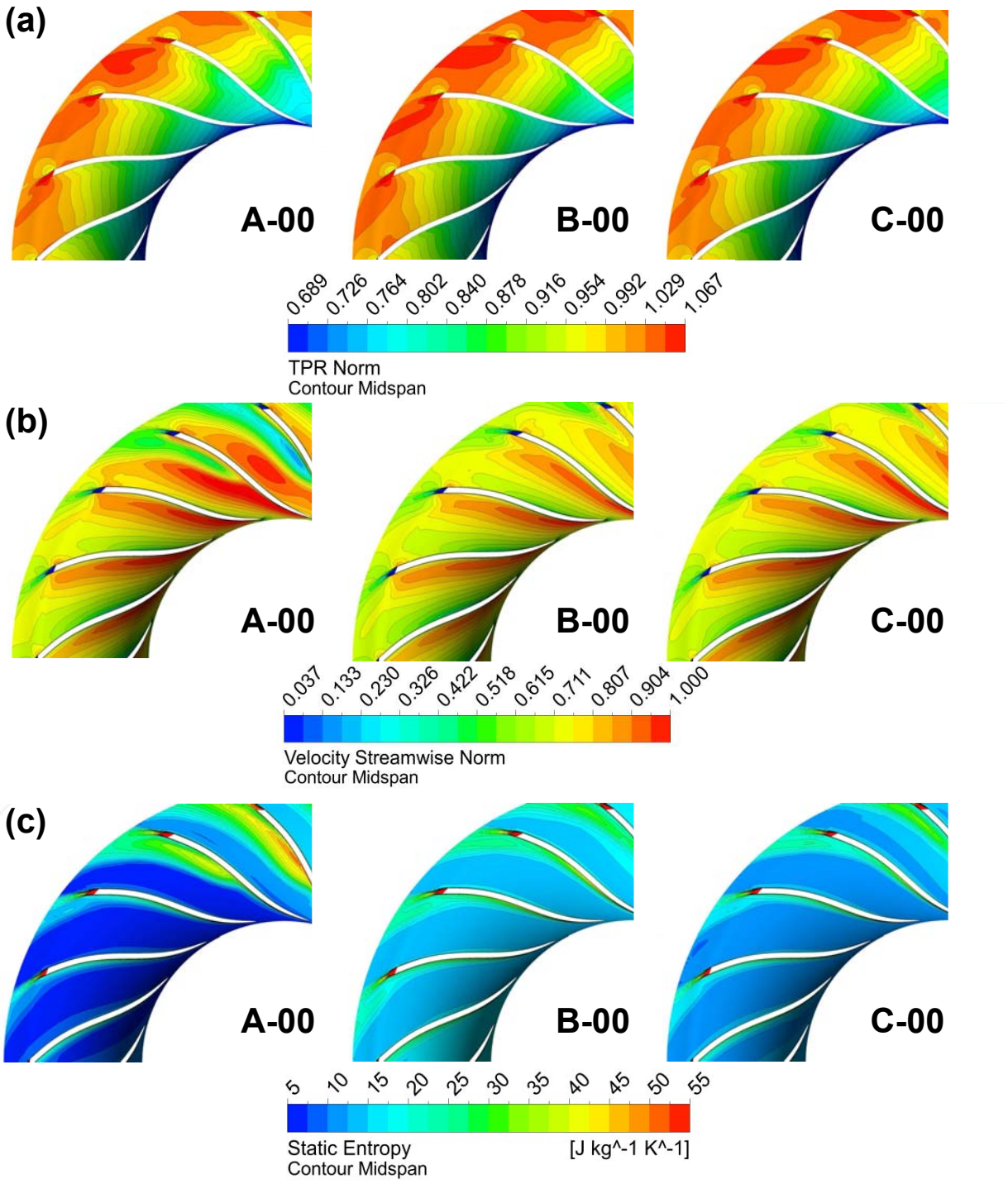

Figure 4.15: Full-annulus simulation results at midspan section: Contours of total pressure, streamwise velocity and static entropy at IGV = 0°

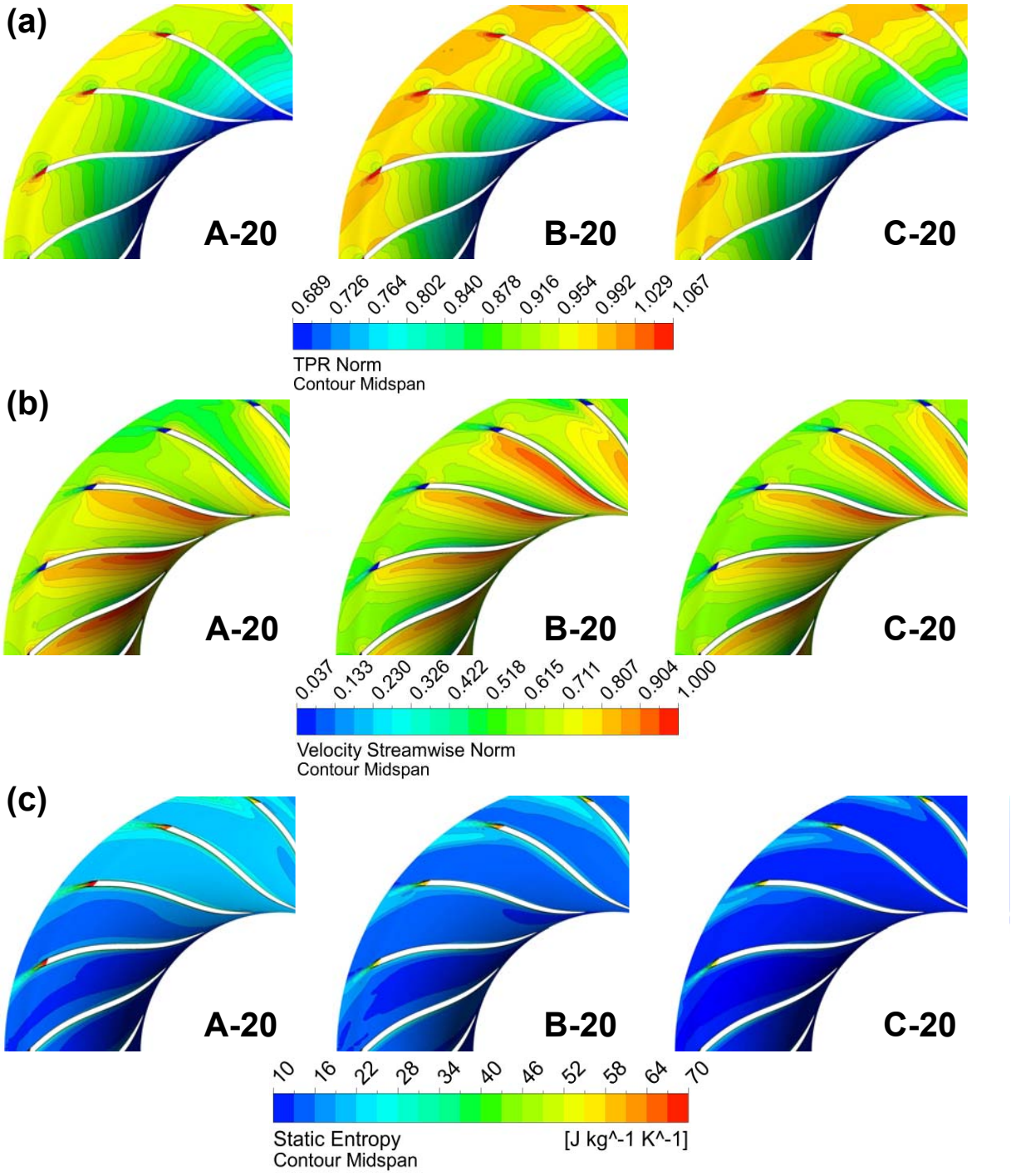

Figure 4.16: Full-annulus simulation results at midspan section: Contours of total pressure, streamwise velocity and static entropy at IGV = 20°

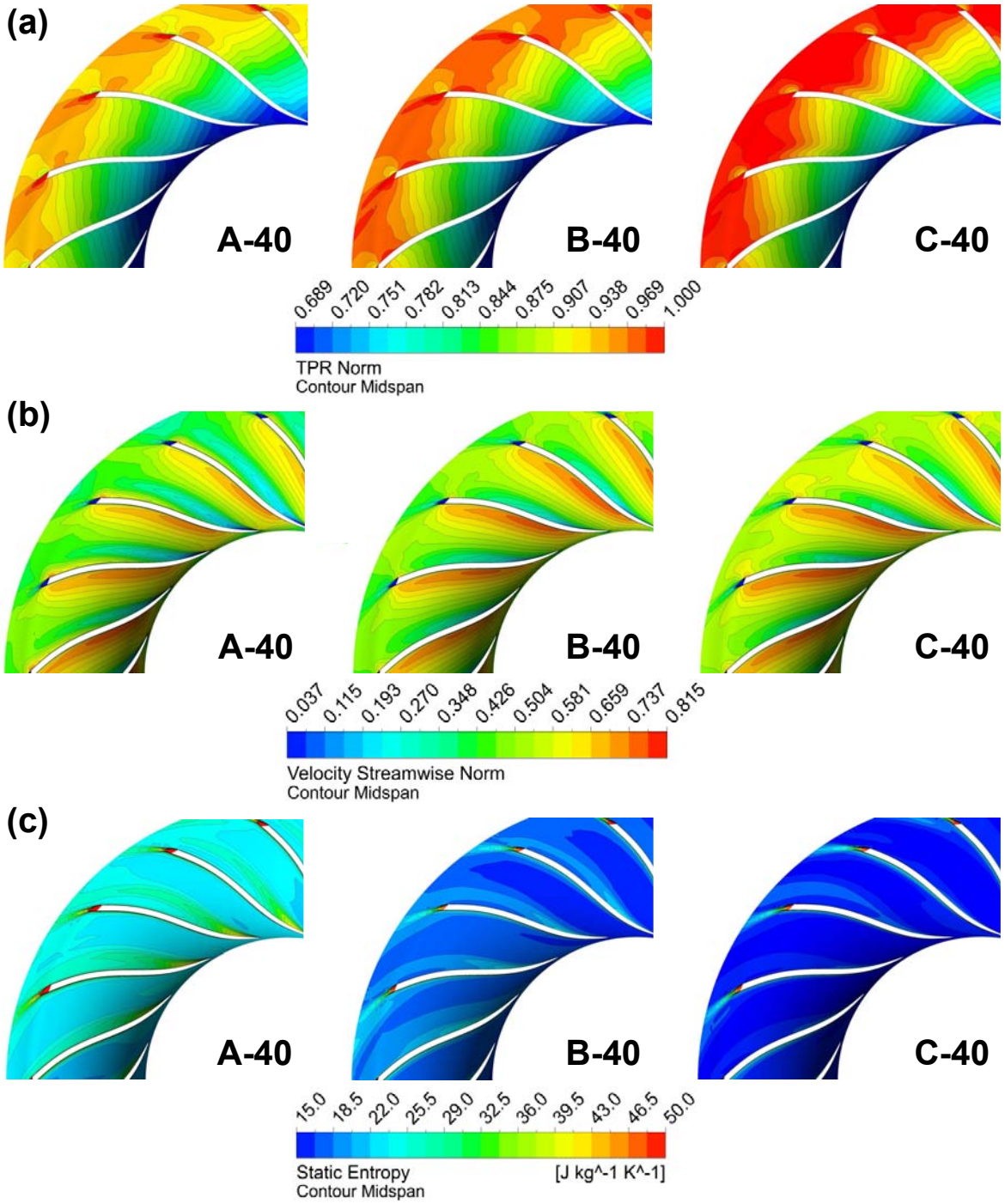

Figure 4.17: Full-annulus simulation results at midspan section: Contours of total pressure, streamwise velocity and static entropy at IGV = 40°

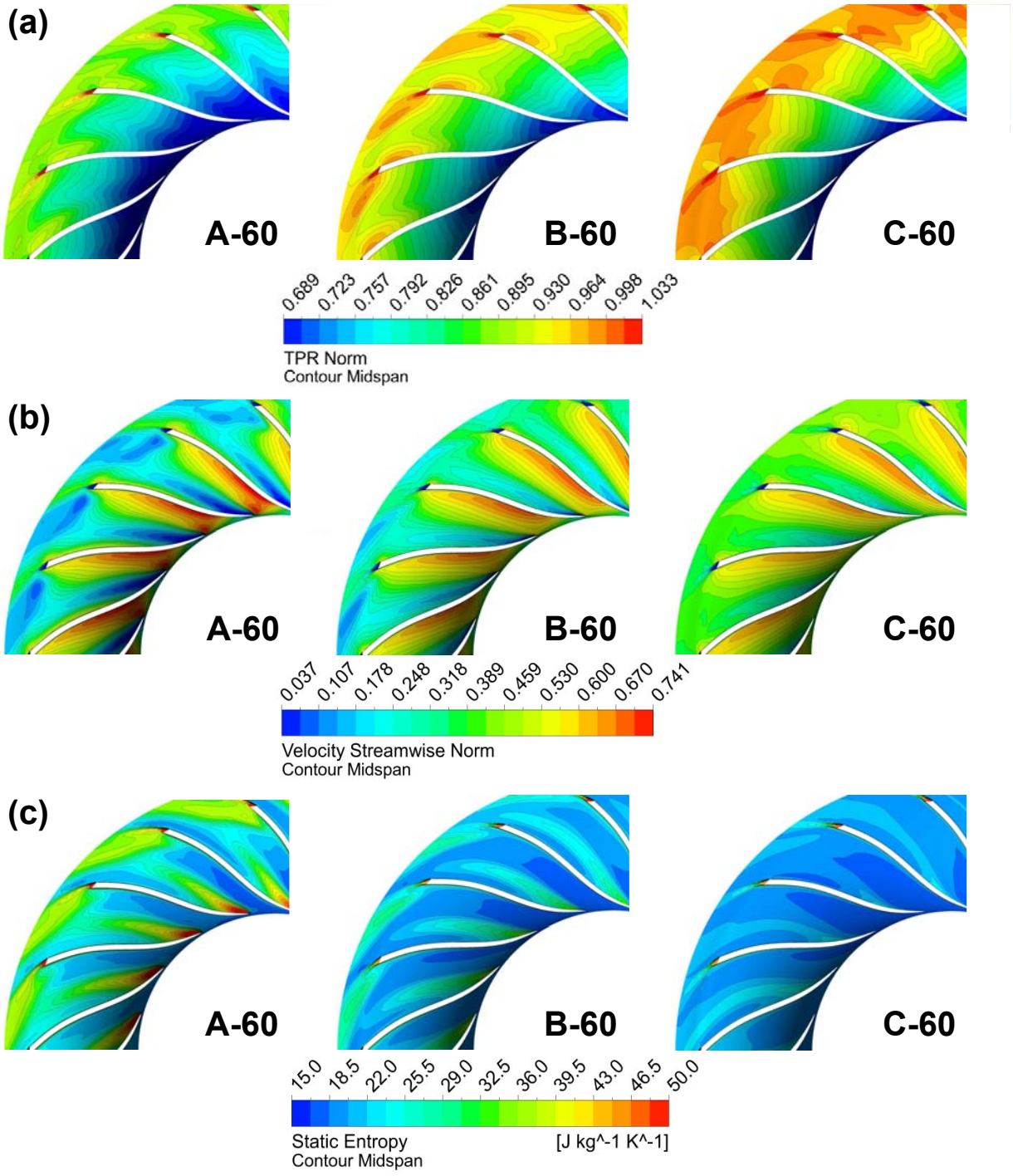

Figure 4.18: Full-annulus simulation results at midspan section: Contours of total pressure, streamwise velocity and static entropy at IGV = 60°

4.4.3 Transient Simulation Result

After the steady full-annulus simulation results have been obtained, they can be applied as initial conditions for conducting a transient full-annulus simulation study. For each transient CFD case, the computation lasts until the time periodicity is reached, which usually takes at least 5 full revolutions. The time periodicity can be manifested by monitoring the critical signals such as p_t, p_s, T_t, T_s, c and $\dot{m}$. For example Figure 4.19 shows the time progress of the mass flow rates during a transient simulation. It includes the last part of steady simulation during the computation as its initial condition. As previously discussed in the full-annulus model setup, at the domain outlet a static pressure controller has been adopted as defined by Equation 4.4. Therefore, the mass flow rate follows a damping process in accordance with the controller. After the mass flow rate reaches the desired value, it fluctuates around the desired value with only small fluctuations around 0.002 kg/s ($< 1\%$), showing a good agreement between transient and steady simulation.

The transient simulations consume significant computation time ($\approx$ 50 CPU hours) and resource (48 cores). Therefore, only the design points at IGV = 0° and nominal points at IGV = 60° are performed. Figure 4.20 shows an example of the total pressure ratio Π_t predicted by the transient simulations, including the time-averaged value (left) and its variations within one time period (right). Firstly, on the left the transient results

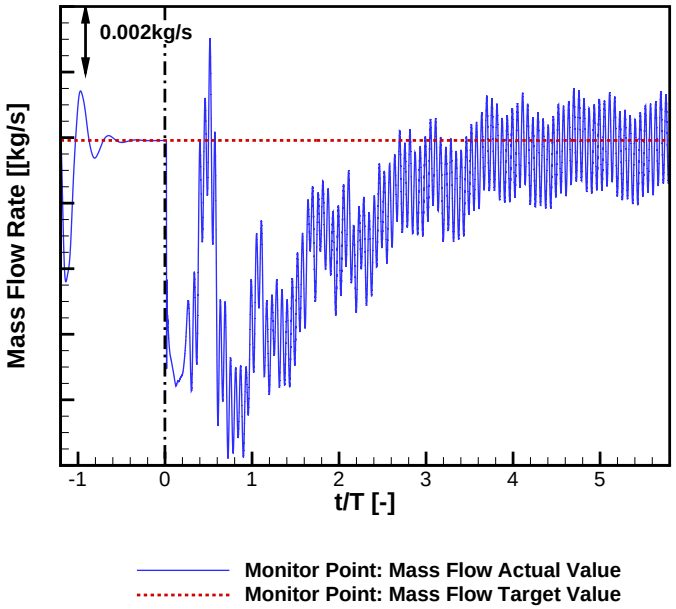

Figure 4.19: Time progress of the mass flow rates during a transient simulation

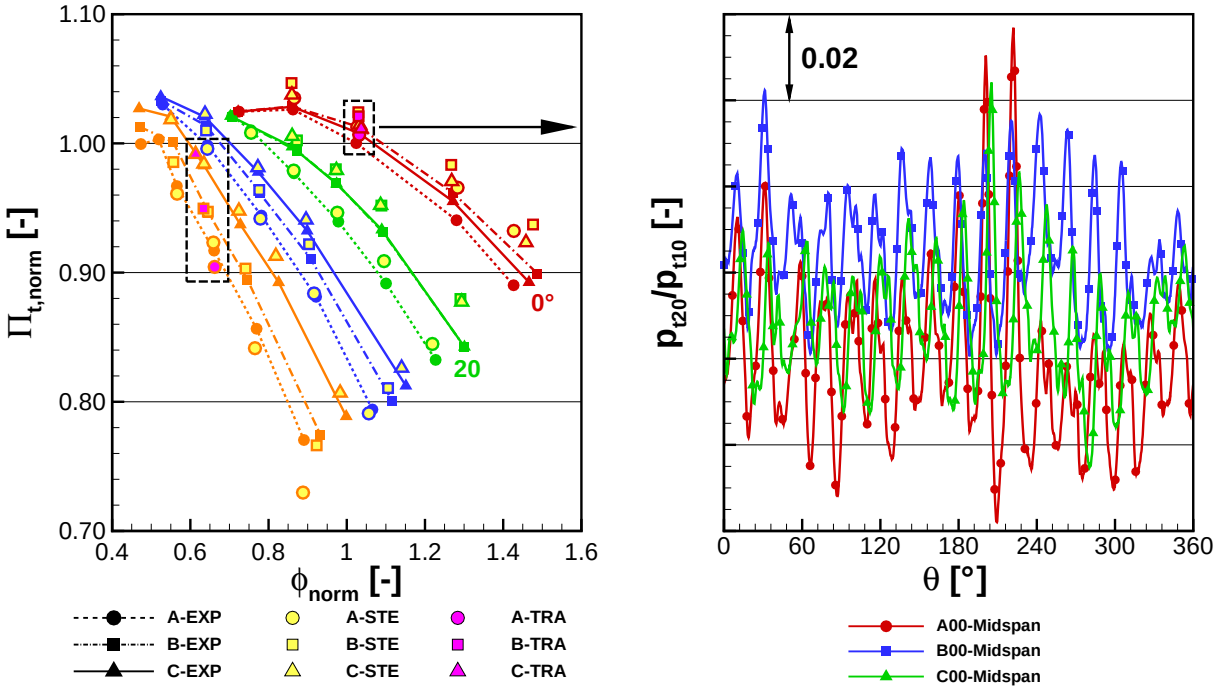

Figure 4.20: Total pressure ratio predicted by the full-annulus transient CFD simulation at IGV = 0° and 60° (left) and total pressure at section 20 (normalized by the value at section 10) on the midspan section at IGV = 0° (right) for the three IGV types

stay close to the steady full-annulus simulation results. Only the case for type-A at 60° predicts even lower levels of total pressure ratio and work coefficient, indicating that the incidence deviation has a greater negative effect during transient calculation, emphasizing the flow unsteadiness between the flow incidence and the impeller leading edge. Secondly, on the right a further comparison of total pressure ratios between the three IGV types is shown. It demonstrates that type-B and type-C (especially type-C) are able to reduce the pressure fluctuations along the 360° circumference. While type-A contains the largest total pressure fluctuations between 180° and 240° up to 12%, type-B and type-C are able to suppress these fluctuations levels down to 6%. Therefore, the transient CFD results indicate that the more homogeneous flow fields created by type-B and type-C can reduce the flow unsteadiness related pressure fluctuations at the impeller outlet (section 20) to the extend of as much as 50%.

In order to analyze the transient CFD prediction at design point for the overall impeller performance more clearly, Figure 4.21 shows the overall parameters predicted by the transient simulations together with the previous steady single-passage, steady full-annulus as well as experimental results (at design point only). For type-B the previous steady full-annulus points can be hardly seen since they are overlapped by the new transient points.

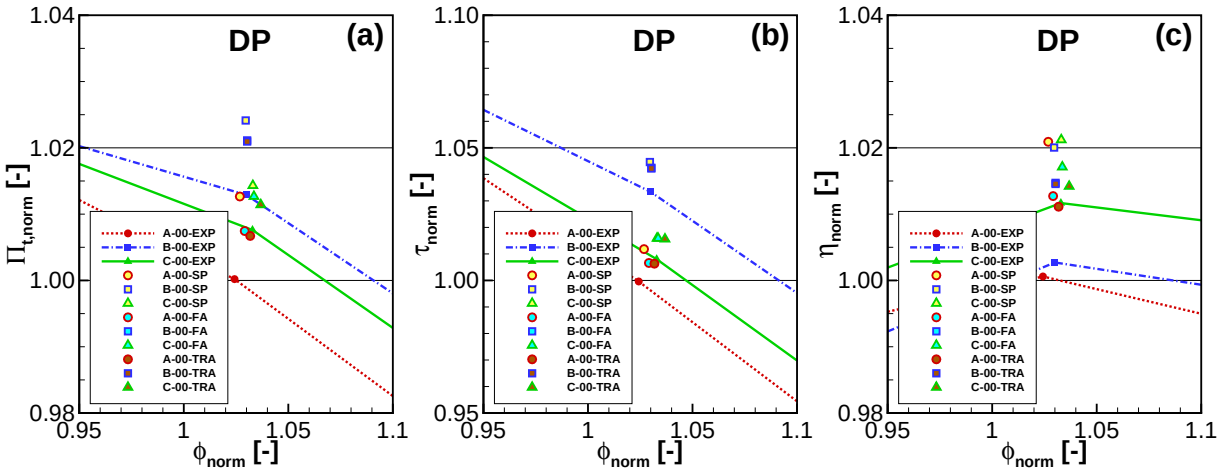

Figure 4.21: Comparison between experiment, steady single-passage, steady full-annulus and transient CFD results at design point; shown are impeller total pressure ratio Π_t (a), impeller work coefficient τ (b) and impeller polytropic efficiency η (c)

The transient points are generated by the time-averaging of one full revolution running after the time periodicity has been reached. For the total pressure ratio and the work coefficient, the overall performance predicted by the transient CFD moves further closer to the experimental results. This indicates that taking flow unsteadiness into account, the simulation accuracy is slightly improved. However, the transient results are still very close to the steady full-annulus points, which proves that compared to the inlet swirl angle set by the IGV, the impact of inlet unsteadiness are only of secondary order.

Similar to the previous session, Table 4.3 presents the relative changes of total pressure ratio Π_t, work coefficient τ and polytropic efficiency η obtained by the transient CFD together with previous results. It can be concluded that transient CFD provides the highest simulation accuracy. However, concerning the computation costs the steady full-annulus CFD is already able to capture the impact of inlet swirl and 360° flow uniformity. Since the transient and steady full-annulus simulations are very closed, the impact of flow unsteadiness on the time-averaged performance is extremely small. In addition, even if the transient, full-annulus simulation has been applied, the CFD results still have an overprediction of impeller performance. It indicates that there must be some other negative factors still unconsidered, such as flow unsteadiness caused by the cavity flow at the impeller inlet and outlet, heat conduction through the impeller walls, etc. Therefore, a more sophisticated modeling might be necessary which is beyond the scope of this study.

In order to examine the local unsteady flow structure predicted by the transient CFD simulation, Figure 4.22 and 4.23 show the total pressure as contour plots at midspan section obtained from the transient CFD at IGV = 0° and 60°. To save space the contour plots

Table 4.3: Comparison of impeller performance parameters between steady single-passage, steady full-annulus and transient full-annulus CFD results at design point

	$\Pi_{t,\mathrm{norm}}$		τ_{norm}		η_{norm}	
A00-SP	1.0127		1.0119		1.0209	
A00-FA-STE	1.0072	(−0.55%)	1.0064	(−0.45%)	1.0128	(−0.81%)
A00-FA-TRA	1.0067	(−0.06%)	1.0063	(−0.01%)	1.0112	(−0.16%)
B00-SP	1.0241		1.0447		1.0200	
B00-FA-STE	1.0212	(−0.29%)	1.0425	(−0.22%)	1.0147	(−0.53%)
B00-FA-TRA	1.0210	(−0.02%)	1.0424	(−0.01%)	1.0146	(−0.01%)
C00-SP	1.0144		1.0162		1.0212	
C00-FA-STE	1.0124	(−0.20%)	1.0162	(0%)	1.0172	(−0.40%)
C00-FA-TRA	1.0112	(−0.12%)	1.0157	(−0.05%)	1.0144	(−0.28%)
Experiment	1.0000		1.0000		1.0000	

only cover 1/4 of the full 360° annulus. In addition, the contour plots contain a record of one full blade passage period (1 BPP = 24 time steps). A total of four time steps within 1 BPP are presented, each with a distance of 1/4 BPP (= 6 time steps). The rotational direction is denoted by a black arrow, which is fixed with the same blade passage during one whole blade passage period. The total pressure is normalized by the same value for all the cases. Since at IGV = 60° an identical scale for total pressure of all three IGV cases is unpractical for that each IGV case has its own total pressure range, in order to focus on the transient flow behavior in the time progress of each IGV type, different color codes need to be applied.

Firstly, Figure 4.22 shows that at IGV = 0° all three IGVs have very homogeneous, repeating flow patterns in the circumferential direction. The compression is done in a smooth and continuous manner as the flow passes through the blade passages. The total pressure levels at the impeller outlet are almost the same.

Compared to the CFD cases at IGV = 0°, Figure 4.23 shows that at IGV = 60° the flow patterns for all three IGVs contain larger levels of flow unsteadiness. These can be substantiated by the findings such as high total pressure regions become scattered, flow non-uniformity between the adjacent blade passages become larger, and the changes of flow patterns during the time progress appear more frequently. In addition, while for type-A the compression is severely interrupted by the pressure-side flow separation, the flow fields of type-B and type-C have significantly recovered. Especially for type-C, the pressure-side flow separation completely disappears. In addition, the flow non-uniformity

across the blade passages is gradually improved for type-B and type-C, for example in the plots for type-C the region near the impeller trailing edge is completely filled with the highest total pressure regions (red spots), and these regions are mostly repeatable throughout the blade passages.

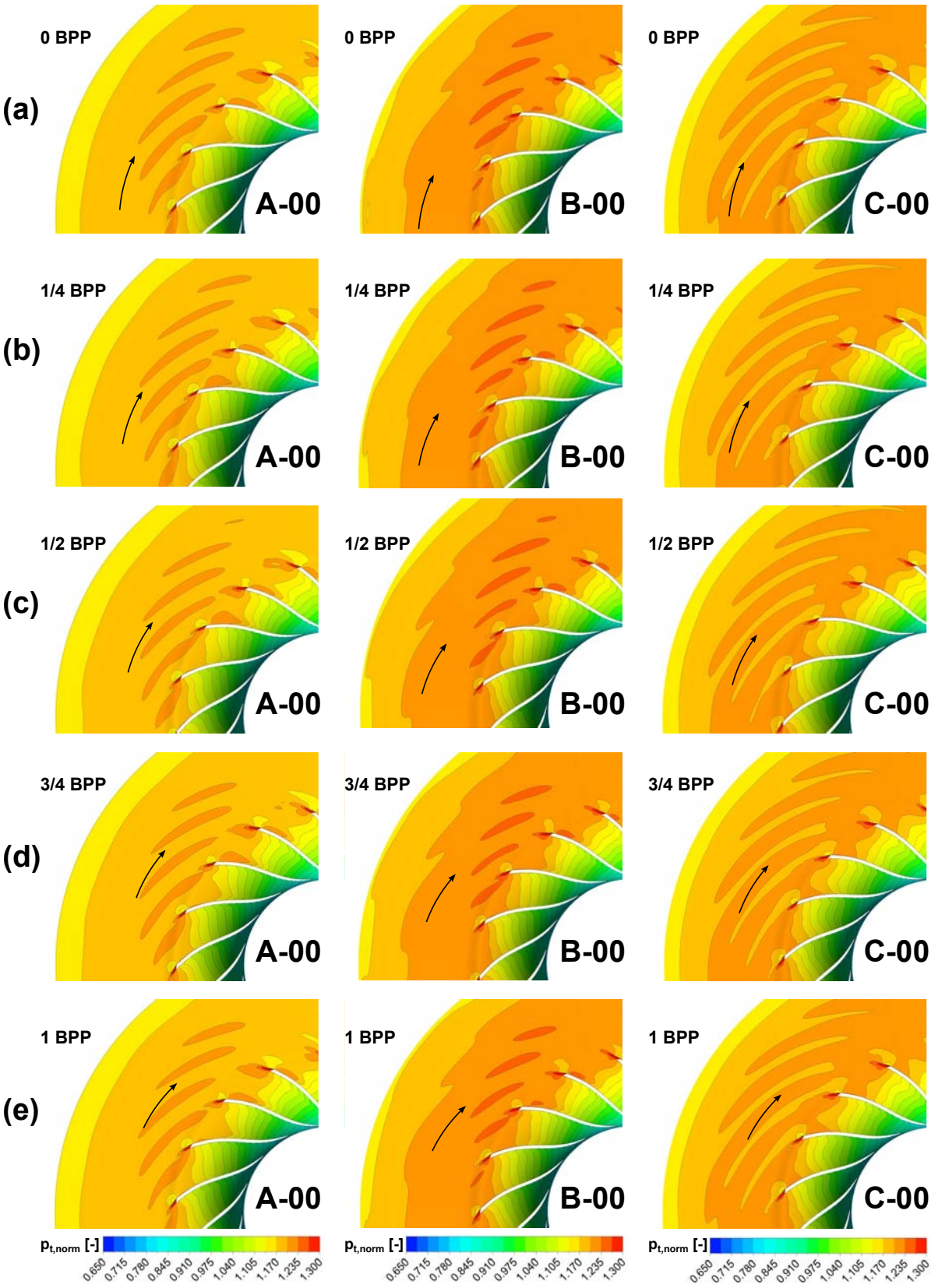

Figure 4.22: Total pressure on the midspan section from transient CFD at IGV = 0°

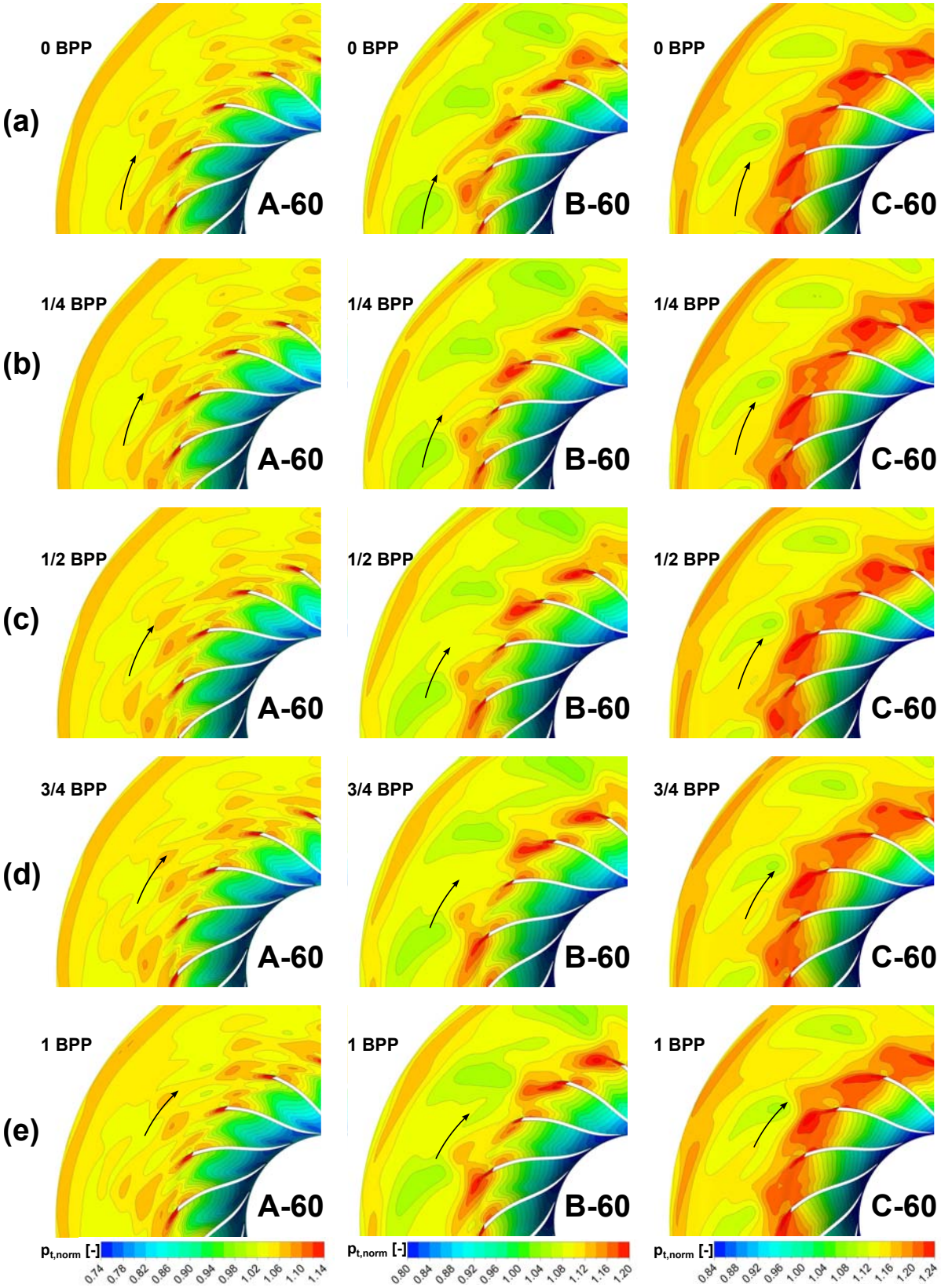

Figure 4.23: Total pressure on the midspan section from transient CFD at IGV = 60°

4.4.4 Internal Flow Structures and Secondary Effects

The previous sections have explained the reasons for the overall stage performance improvement of two new IGV types from the various types of numerical simulations. In this section, the study focus is shifted to investigate the local, detailed flow mechanism to have an in-depth analysis of the internal impeller flow including secondary flow effects. The observation of internal flow phenomena inside of a centrifugal compressor is often difficult to be obtained by conventional experimental methods. It involves sophisticated measurement techniques such as Laser Doppler Anemometry (LDA), Particle Image Velocimetry (PIV) or flow visualization methods via ammonia ozalid, fluorescing oil or liquid crystal sheets. During the IGV test campaign to save time and cost these techniques were not applied. On the other hand, the regular experimental methods (pressure, temperature, etc.) were already enough to validate the stage performance. Therefore, the CFD results conducted in this section serve as a valuable supplement to the experiment.

Figure 4.24 shows the total pressure development on the meridional section of the impeller and diffuser regions, which illustrates the gradual change of compressor flow as the mass flow rates continuously decreases from the design point at IGV = 0° down to the left nominal point at IGV = 60°. Because the tendency in respect to the mass flow decrease is the same for all three IGV types, only the cases for type-A are shown here. The total pressure is normalized by the total pressure at the inlet as the form of total pressure ratio, and at the same time circumferentially averaged on the meridional section. At IGV = 0°, the continuous compression by the impeller can be characterized by its regular distribution of total pressure levels, particularly in the first 2/3 of blade passages. Downstream near the impeller outlet, although the total pressure near the shroud side has a delay of flow acceleration due to the wall contraction between the impeller and the diffuser, the total pressure near to the hub side still grows continuously, which leads to a hub-strong profile at section 20. At IGV = 20°, the impeller can still work normally in the first 2/3 of blade passages. However, when the flow approaches the impeller outlet, the total pressure growth in the core region becomes weaker and slower than the case at IGV = 0°. The weak growth of total pressure particularly affects the profiles near the hub side, since the total pressure near the shroud side is still dominated by the stagnation caused by the wall contraction. In response, the total pressure at section 20 tends to change from a hub-strong to a shroud-strong profile. At IGV = 60°, the unfavorable inlet conditions begin to deteriorate the first 2/3 of impeller, leading to a long delayed total pressure increase. In the last 1/3 of blade passages, the total pressure growth by compression almost comes to an end. Only the shroud-side wall contraction facilitates the local flow a little

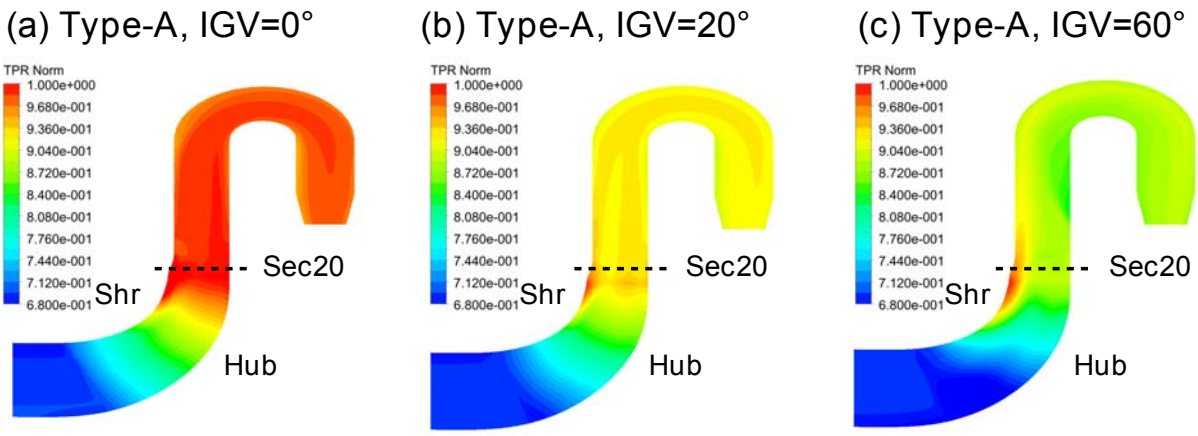

Figure 4.24: Meridional view of contours of total pressure ratio from single-passage CFD simulations; shown are the CFD cases for type-A at IGV = 0°, 20° and 60°

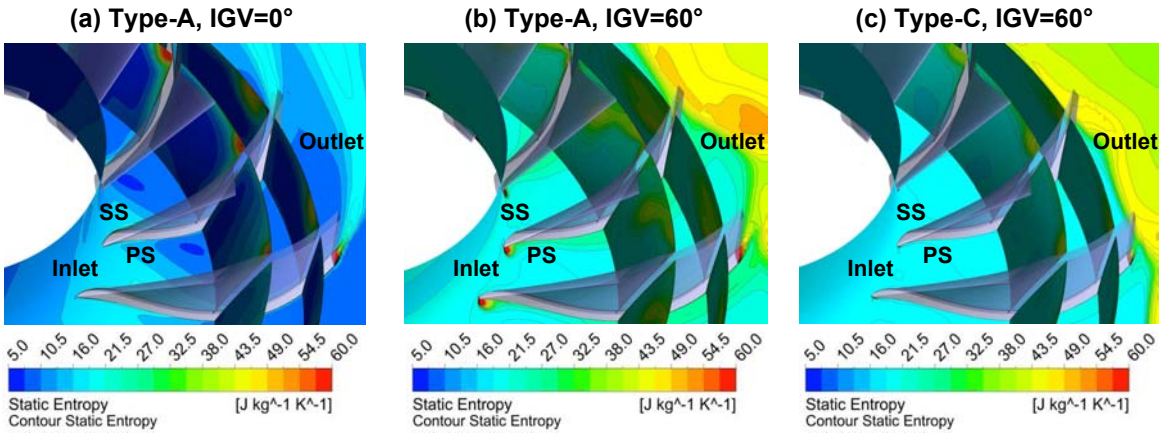

Figure 4.25: Contour of static entropy from transient full-annulus CFD Simulations, shown are two streamwise sections located in the downstream blade passages, and the spanwise section located near the hub wall for type-A (0° and 60°) and type-C (60°)

to reach higher levels. As a consequence, the total pressure at section 20 inevitably has a shroud-strong profile. This shift from hub-strong to shroud-strong profiles as the mass flow rate decreases is quite universal for this type of centrifugal compressor; see the total pressure profiles measured before in Figure 3.16.

In order to evaluate the flow losses in the impeller blade passages, Figure 4.25 visualizes the contours of static entropy on two streamwise sections and one near-hub spanwise section for the cases for type-A at IGV = 0° and 60°, and type-C at IGV = 60°. Type-C at IGV = 0° appears to be very similar to type-A at IGV = 0°, and thus is not shown here. At IGV = 0°, the jet-wake flow structure, which is typical for a normal functioning centrifugal compressor, can be clearly identified by the high region of entropy on the suction side of blade passages near the shroud. The flow losses are firstly accumulated at the

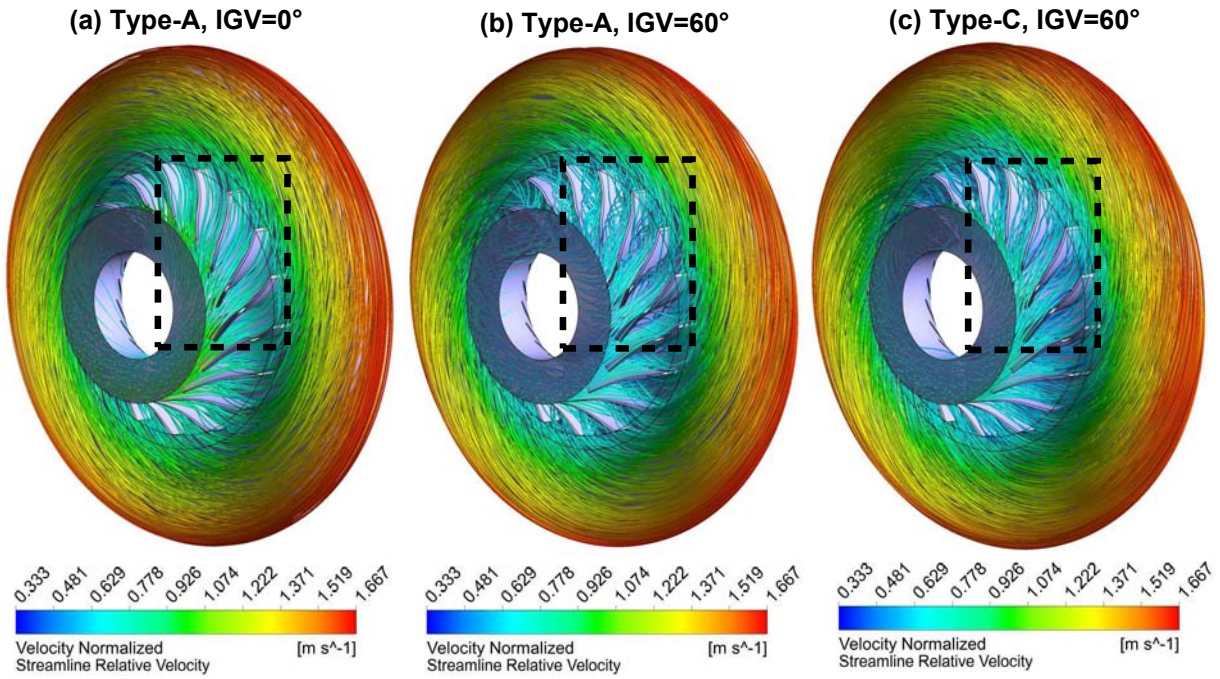

Figure 4.26: Streamlines of velocity from transient full-annulus CFD simulations; shown are the CFD cases for type-A (0° and 60°) and type-C (60°)

suction-side shroud corner, and then relieved by mixing out in the secondary section. This is very consistent with the typical jet-wake flow structure introduced in Chapter 2. For type-A at IGV = 60°, induced by the overturned inlet flow direction, the largest flow losses are located on the pressure-side blade surface at the impeller leading edge, as indicated by the contours of static entropy on the spanwise section. On the streamwise sections, the jet-wake pattern is largely destroyed by another high-loss region on the pressure side near shroud. This region can be associated with the pressure-side flow separation and related secondary flow phenomena such as passage vortices, which can be proved later in Figure 4.26 and 4.27. For type-C at IGV = 60°, the overturned inlet flow direction is recovered back to normal. Correspondingly, the two regions of high losses, one at the pressure-side leading edge and the other on the downstream pressure side near shroud as shown by type-A, are completely disappeared. The typical jet-wake pattern appears again at the suction-side shroud corner, which indicates that the impeller is back to its normal operation.

Figure 4.26 illustrates the velocity streamlines in the impeller and diffuser domain for the cases for type-A at IGV = 0° and 60°, and type-C at IGV = 60°. Due to the similar flow fields for type-A and type-C at IGV = 0°, the case type-C at IGV = 0° is omitted here. The streamlines describe the velocity direction, whereas the scale of streamlines is chosen to be the absolute velocity in order to correctly denote the velocity magnitude in the im-

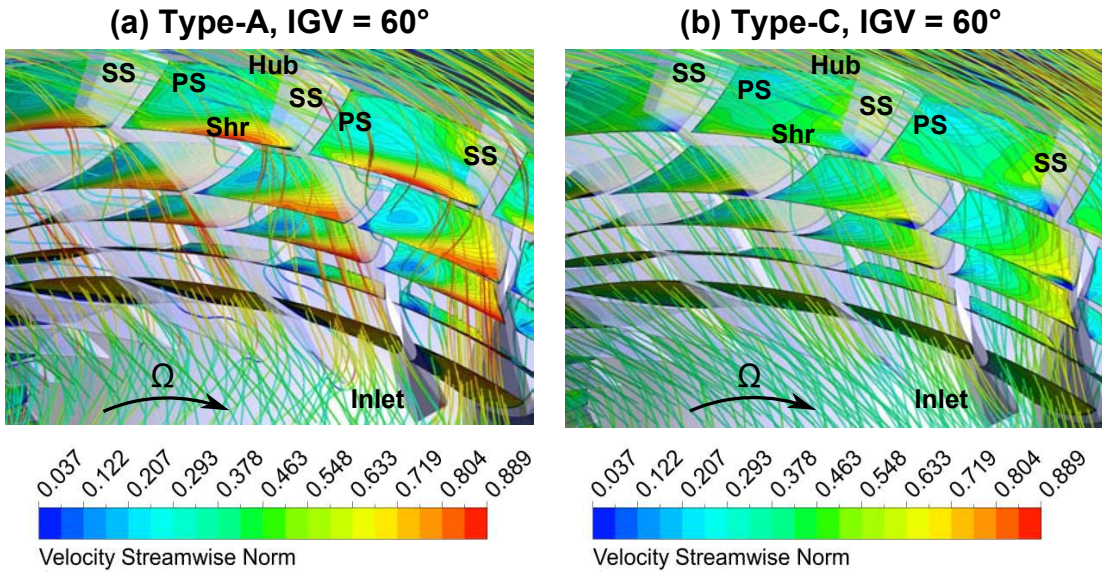

Figure 4.27: Secondary flow from transient full-annulus CFD simulations; shown are the contours of meridional velocity located in the downstream blade passages, and streamlines for type-A at IGV = 60° and type-C at IGV = 60°

peller and diffuser domain. For type-A at IGV = 0°, the streamlines are quite uniform and parallel, indicating a normal and stable operation of the impeller. At IGV = 60°, however, due to the pressure-side separation caused by the unfavorable inlet conditions for type-A, several strong vortices begin to appear, following the occurrence of one vortex per blade passage. The vortices tend to push the flow from the pressure side to the suction side. As the vortex tails travel from the pressure side towards the suction side, the vortices grow rapidly and eventually occupy the full blade passages. In the downstream blade passages, the impeller flow is severely distorted by the vortices. Even the flow part which originally follows the suction-side blade surface is entangled by the vortices reaching the suction side. The disturbances caused by the pressure-side flow separation and its associated vortices are the main reasons to stop the compression downstream, which can be indicated by Figure 4.24-(c). For type-C at IGV = 60°, the impeller flow is largely recovered by the improved inlet conditions. Only a small portion of streamlines on the top of impeller tends to leave the suction-side blade surface at the leading edge. Therefore, despite of largely recovered inlet flow, the type-C at IGV = 60° is still less stable compared to the design point at IGV = 0°.

Finally, Figure 4.27 illustrates the impact of vortices on the local secondary flow, in which the streamlines are plotted together with the contours of streamwise velocity in the blade passages on the streamwise sections for type-A and type-C at IGV = 60°. On the left for type-A at IGV = 60°, the passage vortices near the upstream pressure-side blades cause

the local flow to stagnate, leaving a low velocity region propagating downstream on all streamwise sections. Meanwhile at the leading edge, the pressure-side flow separation leads to a smaller effective flow area in the blade passage, which forces the suction-side flow to accelerate more quickly. The suction-side flow acceleration is particularly strong near the shroud-side blades. Later downstream, the developed passage vortices are moving towards the shroud corner of the suction-side blades, and eventually prevents the suction-side flow acceleration. On the right for type-C at IGV = 60°, the streamlines are recovered back to normal. The impeller flow is subjected to neither pressure-side separation nor passage vortices. As a consequence, the typical jet-wake secondary flow pattern, similar to the IGV = 0° case shown in Figure 4.25-(a), appears again, which is characterized by a low-velocity region at the suction-side shroud corner.

From the CFD results it becomes clear that under its normal operation at the design point, the impeller applied by this project contains a typical jet-wake flow at the suction-side shroud corner in the downstream blade passages on the streamwise section, as well as a hub-strong flow profile at the impeller outlet on the meridional section. As the IGV setting angle increases from 0° to 60°, the mass flow rate is continuously reduced, which shifts the hub-strong profile into a shroud-strong profile at the impeller outlet. For type-A, the over-turned inlet flow direction leads to a pressure-side flow separation at the impeller leading edge, which further initiates strong passage vortices propagating from the pressure-side towards the suction-side blade walls. Consequently, the original jet-wake pattern in the blade passages is completely distorted by the flow separation and passage vortices. After the inlet flow is recovered by type-B and type-C, the pressure-side separation and vortices are successfully prevented.

4.5 Transient Blade Row Simulation

In the previous sections, the full-annulus model is applied to be imposed with the IGV induced 360° flow distortion as inlet boundary conditions. As an alternative to the need for a full-annulus model, the transient blade row (TBR) method, which has been incorporated into ANSYS CFX Version 15.0, may offer a possibility to spare the large computation cost by using a two-passage model instead of modeling the full annulus. Especially the new TBR method using Fourier Transformation (TBR-FT) can handle the inlet distortion with large pitch ratios to the blade passage. It may be useful for the practical applications similar to this IGV project. However, in the literature the TBR-FT method has been only tested with simplified inlet distortion, such as in Sharma [72] which contains a cosine wave of total pressure to represent the inlet fan distortion with one period per revolution. So

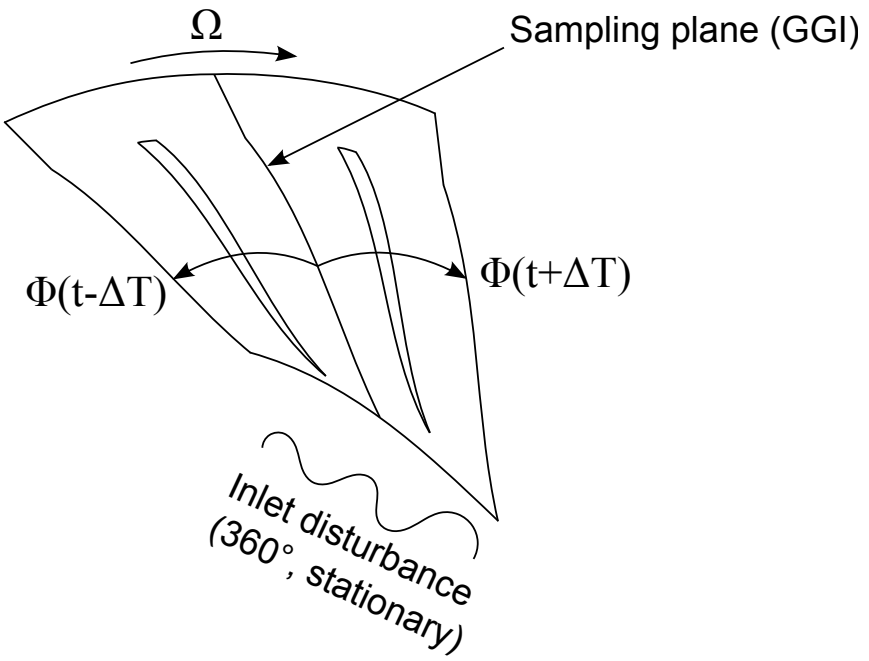

Figure 4.28: Sketch of the two-passage model for the TBR-FT simulation

far the TBR-FT method is rarely applied for analyzing real inlet distortion. Given that the TBR-FT method may have a potential usage for this project, this section includes a simulation study using the TBR-FT method, and for the first time the quality of TBR-FT results obtained by imposing the real inlet distortion induced by the IGVs to the impeller.

4.5.1 Theoretical Background

The TBR method has been incorporated into ANSYS CFX Version 15 with three optional approaches: profile transformation (ANSYS [4] and Erdos [31]), time transformation (Giles [38] and Biesinger [10]) and Fourier transformation (He [47] and Sharma [72]). For this study, the inlet distortion induced by the three IGV designs are quite non-uniform both in the radial and circumferential directions, and thus can only be reproduced by a 360° flow field. As a consequence, the pitch ratio between the IGV outlet section and the impeller inlet section is much higher than one. Therefore, only the Fourier transformation (FT) method is a suitable approach for the transient blade row simulation.

The Fourier transformation (FT) method, which is based on the transformation between time domain and frequency domain, takes advantage of a two-passage model (Figure 4.28) to reach quick convergence with less data storage. It stores the flow fields in history by using Fourier series at the blade-passing frequency (BPF) and its higher harmonics by using the following equations ANSYS [4]:

- At the pitchwise boundary:

$$\phi(t) = \sum_{m=-M}^{M} A_m e^{-j\omega m t}; \quad T_{BP} = \frac{2\pi}{\omega} \tag{4.12}$$

- At the rotor/stator interface:

$$\phi(t,\theta) = \sum_{n=-N}^{N} \sum_{m=-M}^{M} A_{n,m} e^{-j(\omega m t + n\theta)} \tag{4.13}$$

The two-passage model allows extracting the signals from the sampling interface between the adjacent passages, and reconstructing these signals to the two side boundaries with phase-shift. The similar strategy is used for the rotor-stator interface by using double Fourier series including the flow history in both time and azimuthal direction. The advantages of using the FT method, according to Blumenthal [12], are as follows:

- It is capable for all rotor speeds;
- Large pitch ratios are allowed;
- It is possible for multi-stage configurations.

Based on the steady and transient CFD results done in the previous part, this section presents the unsteady simulation results using TBR-FT method by comparing them with the full transient cases, in order to check whether it is possible to achieve good quality with this new method with less computation cost.

4.5.2 Simulation Setup

For the TBR-FT simulations, the same mesh grids per passage are used for a two-passage model, as illustrated in Figure 4.28. The main difference is that the two sides are defined as the phase-shifted periodic boundaries, while the middle overlapping side is defined as the sampling boundary. The impeller, diffuser and U-bend are defined as one single rotating domain, which avoids creating an extra rotor-stator interface. Consequently, the walls of the diffuser and the U-bend, as well as the hub and shroud after the impeller trailing edge are defined again as counter-rotating walls.

For the TBR-FT simulations, the boundary conditions can be directly taken from the previous measured 360° flow fields, including p_t, T_t and yaw angle. This is done by imposing the flow fields onto a stationary domain while the impeller is combined with a rotating

domain. In this way the impeller domain sees the different partial regions of 360° flow field at each different time step. For the TBR-FT simulations, a constant time of 1/24 blade-passing period (BP) is set as the time step based on a preliminary study on various time step lengths of 1/12, 1/24 and 1/48 BP.

In particular for the setup of the transient blade row model, the inlet distortion is modeled as rotational flow boundary condition, the phase corrected interfaces are the side boundaries of the two-passage model, and the sampling domain is the middle interface between the two passages. The external passage is defined as 1 per component and 1 per 360° turn, which guarantees that the two-passage model sees the inlet distortion as pitchwise non-periodic, but periodic once per the whole revolution. Therefore, the time period is equal to the time of one revolution. The TBR-FT method needs a minimum of 5 periods to reach time periodicity. During the calculation, the TBR-FT solver required a total of 10 periods to reach a good time-periodic state.

4.5.3 Result of Transient Blade Row Method

For a transient simulation, while a full 360° mesh model includes all of the blade numbers, a TBR-FT simulation only contains two passages. Experience shows that the transient simulations require a minimum of 5 periods to converge, while the TBR-FT needs a total of 10 revolutions to converge. The reason that the TBR-FT method requires more periods is that it needs 3 revolutions as initialization, and then needs 3 periods as start-up phase for the TBR calculation. Despite of the larger number of revolutions, the TBR-FT results in a quicker convergence due to its much smaller model size. Regarding the computation cost which can be simplified as the mesh size times the number of revolution until time periodicity is reached, the TBR-FT method is about 4.5 times faster than the transient method. Another advantage of TBR-FT method is that one single TBR result contains all the Fourier coefficients needed for the flow reconstruction at any point in time. This saves all the memory a full transient method needs during the computation.

Table 4.4 summarizes the overall performance parameters predicted by the steady, transient and the TBR-FT methods for type-A at IGV = 60°, including the total pressure ratio Π_t, polytropic efficiency η_{poly} and head coefficient h. All values are normalized by the experimental value. The numbers predicted by the different simulation methods are very close to each other, and this tendency in respect to the experimental results is quite consistent. Comparing the values for the steady, transient and TBR-FT methods, it is noticeable that the levels of TBR-FT CFD results are always between the steady and the transient CFD results. This agrees with the expectation since the TBR-FT method only

Table 4.4: Overall performance parameters predicted for type-A at IGV = 60° by the steady, transient and TBR-FT methods; shown are all values normalized by the experimental value

[t!]

Method	Π_t		η_{poly}		h	
Steady	0.9926	(−0.74%)	1.1043	(+10.43%)	0.9674	(−3.26%)
Transient	0.9911	(−0.89%)	1.0937	(+9.37%)	0.9621	(−3.79%)
TBR-FT	0.9925	(−0.75%)	1.1015	(+10.15%)	0.9672	(−3.28%)
Experiment	1.0000		1.0000		1.0000	

considers the harmonics of the periodic unsteadiness.

In order to examine the time progress of the transient and the TBR-FT methods, Figure 4.29 further demonstrates the total pressure progress for the monitor point at the impeller outlet during two revolutions. The transient results (full line) are compared with the TBR-FT results (dashed line) at the same spatial and the same circumferential positions. In general, the repeatable curves show that the time periodicity is reached for both result groups. The levels for the two groups are in good agreement. Specifically at the monitor points further downstream, the TBR-FT curves behave differently than the transient curves. They seem to be smoothed out by omitting the fluctuating peaks along the overall progress. Similar behavior can be found for the time progress for other physical parameters such as static pressure, static and total temperature (not shown). It is likely that due to the principle of Fourier reconstruction, all the harmonics of non-BP frequency are neglected by the TBR-FT method, which causes these instantaneous signals to be filtered out.

Figure 4.30 illustrates the contour plots of total pressure at the normal sections at the domain inlet as well as three different locations downstream towards the impeller leading

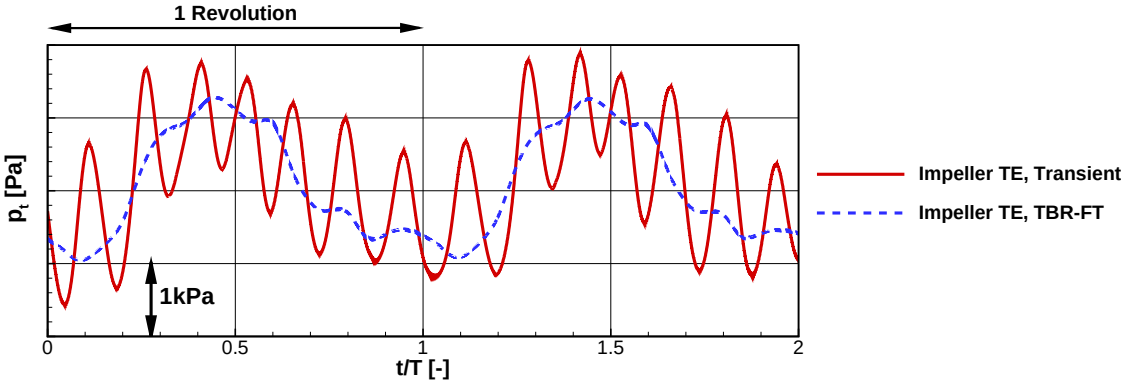

Figure 4.29: Total pressure time progress at impeller outlet with comparison between the transient and the TBR-FT methods

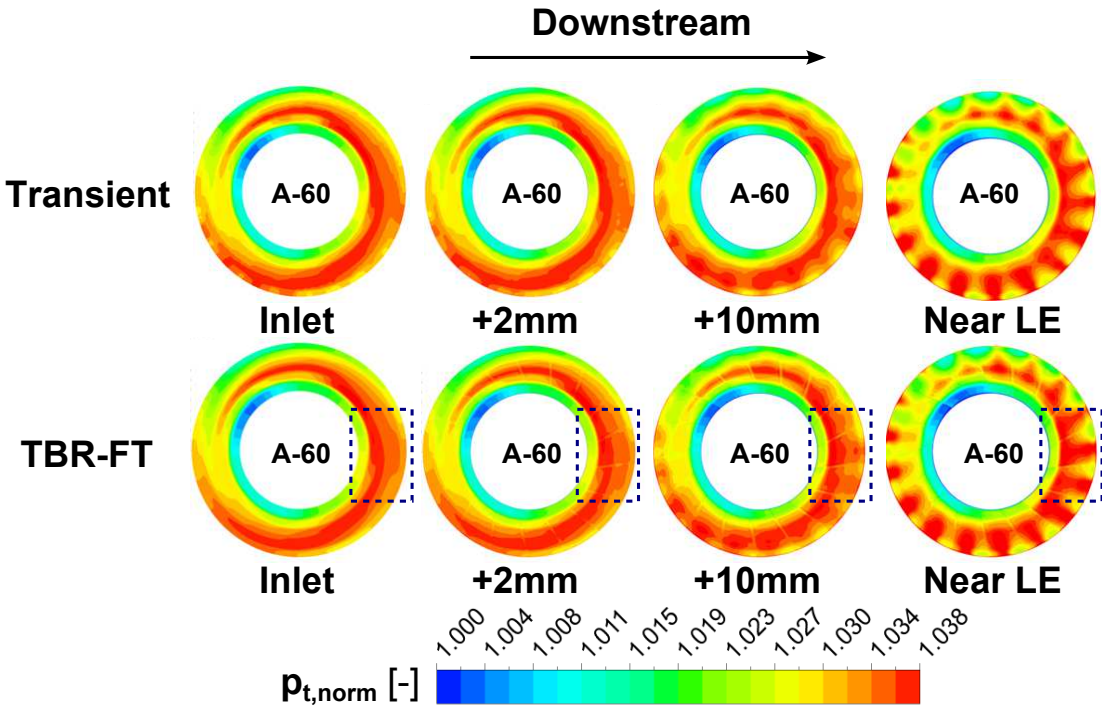

Figure 4.30: Inlet flow patterns of total pressure from domain inlet to the location near the impeller leading edge, with comparison between the transient and the TBR-FT results

edge. The transient and the TBR-FT results are shown as a comparison. In general, both of the results are able to represent the non-uniform distortion at the inlet, and produce sensible flow fields further downstream as the effects of IGV-impeller interactions. However, the contour plots of the TBR-FT method contain some small discontinuities (denoted by the dash boxes) across the blade passages, exactly where the boundaries are located. This indicates that the pitchwise update of signals used by the TBR-FT method, which extracts the signals at the middle boundary to the two side boundaries, may affect the smooth transition from one side of the boundaries to the other. Possibly this aspect might not be obvious when the inlet distortion is pitchwise periodic across the boundaries, however, for the application of this study, the inlet distortion is not periodic within one revolution. Therefore, it may be difficult for the TBR-FT method to connect the flow solution beyond the side boundaries.

Figure 4.31 shows the contour plots of total pressure at midspan section from the impeller inlet down to the diffuser, with comparison between the transient and the TBR methods. From Figure 4.31 the distinct behavior of the TBR-FT method, which has been shown in Figure 4.29 and 4.30, can be clearly identified again. The transient CFD result shows that the pressure-side flow separation induces quite different regions in the circumferential direction at the impeller outlet, which is plausible due to the large 360° flow non-uniformity

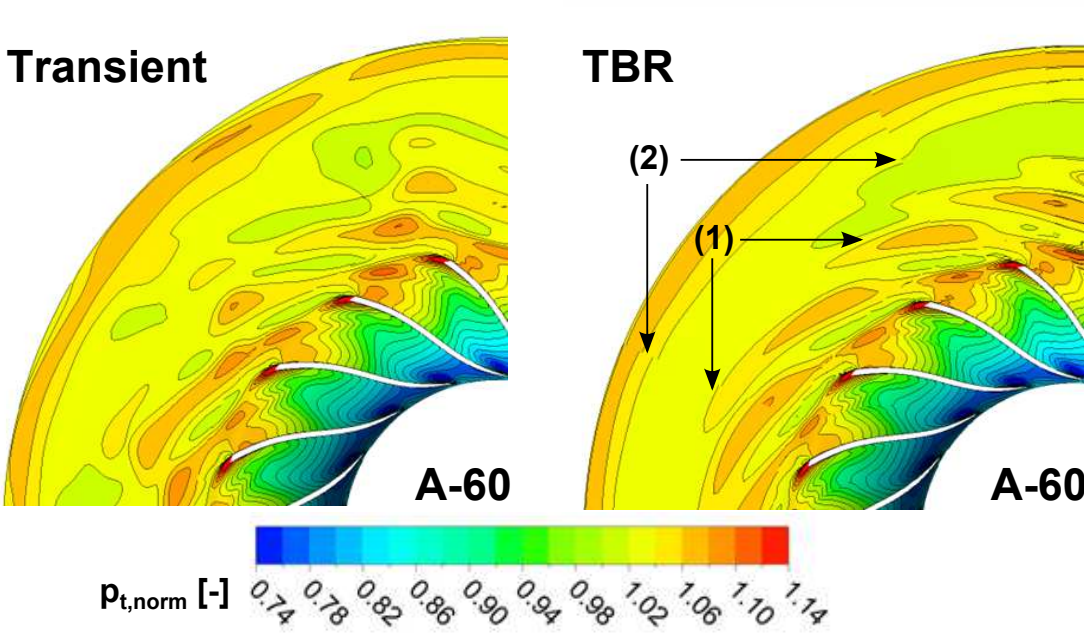

Figure 4.31: Contours of total pressure at the midspan section for the A-60 case, with comparison between the transient and the TBR-FT methods

and unsteadiness for type-A at IGV = 60°. This random shaped flow regions also indicate that they are not related to the blade passing frequency. In contrary, the TBR-FT result shows relatively ordered regions, which repeat from one passage to the next neighboring passage (1). This is consistent with the smoothed-out pressure fluctuations in Figure 4.29. Secondly, the flow discontinuities also show up on the spanwise direction across the side boundaries (2), which is similar to what was found in Figure 4.30. Despite of these two discrepancies, the TBR-FT predicts the flow field which is similar to the transient result.

4.5.4 Summary of Transient Blade Row Simulation

The comparison between TBR-FT and previous results show that this new method is capable of predicting time-average or spatial-average overall performance parameters with considerable less computation resources. Some small discrepancies are found for the TBR-FT method regarding the smooth-out pressure fluctuations and the discontinuities across the boundaries, which can be associated with the theoretical principle of Fourier transformation using two-passage model.

4.6 Summary

This chapter investigates the IGV-impeller flow mechanisms inside the compressor stage by performing a series of CFD simulations. Firstly from the steady single-passage simulation results, a match can be found in the prediction of total pressure which ensures a correct prediction of total pressure ratio. Some biases exist in the prediction of total temperature which leads to an over-prediction of work coefficient and polytropic efficiency. The relative levels of performance parameters are well preserved by the CFD simulations for the three IGV types. From the midspan compressor flow fields, it is found that the incidence angle is the main reason for the large deviation in the stage performance at higher IGV setting angles. For the baseline IGV, the large deviation in the incidence angle, which is due to its overturned swirl angle, creates large flow separation on the pressure-side blade surface. This incidence change can be largely mitigated by using the two new IGV designs, the unique cambered IGV and the multi-foil IGV, which ensure that the relative flow direction still remains in line with the impeller leading edge. As the next step by adopting the full-annulus model, the 360° circumferential flow distortion can be imposed as part of the inlet boundary conditions, which is one step closer to the real flow fields provided by the three IGV types. The quality of steady full-annulus CFD is improved accordingly in terms of successful capturing the impact of inlet distortion. It is found that the flow non-uniformity induced by the circumferentially non-uniform IGVs are further transported down to the impeller outlet, which demonstrate as large pressure fluctuations along the impeller circumference. From the full-annulus steady CFD results, the 360° flow non-uniformity is found to be responsible for 0.8% decrease of the impeller polytropic efficiency at design point for the baseline IGV, while type-B and type-C can largely reduce this type of performance degration cuased by the inlet flow non-uniformity (down to 0.5% and 0.4% of efficiency decrease, respectively) by providing more homogenious inlet flow conditions. The flow unsteadiness existed in the real flow requires further the full-annulus transient CFD results. It is further found that at design point, the baseline IGV can induce as twice as much as total pressure fluctuations (12% of p_{t10}) downstream at the impeller outlet than type-B and type-C (6% of p_{t10}) due to the stronger flow unsteadiness. In addition, the overall impeller performance is best predicted by the transient CFD, and the gaps between CFD and experiment in the impeller total pressure ratio and work coefficient are further reduced. The remaining over-prediction of efficiency indicates that there might be other practical factors existed during the experiment but not captured by the simplified CFD models. Although the transient full-annulus CFD improves the simulation accuracy, it changes only slightly in addition to what has been achieved by

the steady full-annulus simulation. This indicates that for this IGV study, the correct inlet swirl and the reduced 360° circumferential inlet distortion are the main reasons for the improved impeller performance achieved by type-B and type-C. The detailed internal flow structures and secondary flow patterns demonstrate that the three IGV types can significantly alter the flow development inside the impeller blade passages. For type-A at IGV = 60°, the normal jet-wake pattern for this type of centrifugal compressor is distorted by the pressure-side flow separation and passage vortices propagating from the pressure-side blade surface to the downstream passages. Finally since the unsteady CFD demands for very large computation costs, the new TBR-FT method is introduced and examined for possibly replacement of the 360° model. The TBR-FT result shows that it could be as good as the other methods in predicting the overall performance parameters, yet is subjected to the small discrepancies by smoothing-out the flow fluctuations of non-BPP frequency and discontinuities across the side boundaries.

Chapter 5

Conclusion and Prospect

5.1 Conclusion

This dissertation presents a complete research project on a centrifugal compressor stage with variable inlet guide vanes. A total of three IGV configurations, including a baseline IGV with NACA profile as reference, an unique-cambered IGV and a multi-foil IGV, have been experimentally validated and numerically investigated. The two new IGV configurations incorporate circumferentially non-uniform profile designs, which were optimized during the design process together with the radial IGV plenum. The experimental result from the IGV rotating test campaign shows that the two new IGV designs are able to generate very promising stage performance results. The two IGV designs, the unique-cambered IGV and the multi-foil IGV, contribute to the improvement of overall stage efficiency of up to 2% at design point, and surpass the baseline IGV at other off-design points. While the unique-cambered IGV (type-B) has an improved behavior in the positive range due to its biased profile design, the multi-foil IGV (type-C) demonstrates the best efficiency in both positive and negative ranges. At higher positive IGV setting ranges, the multi-foil IGV is able to maintain a good linearity between swirl angle magnitude and IGV setting angle, which ensures a correct incidence angle for the impeller. The benefits achieved by the two new IGV designs can be demonstrated by reduced pressure losses of the IGV plenum, more uniform flow fields at the impeller inlet section, and controlled magnitude of pre-swirl. With these advantages, the impeller can work more efficiently within a wider operation range. This leads to higher total pressure ratios and higher polytropic efficiencies at the impeller outlet, which can be further preserved by the downstream components to the stage outlet. While at smaller IGV setting angles the flow uniformity is the main contributor for the improved performance of two new IGV types, at larger IGV setting angles the correct flow incidence guaranteed by the better swirl linearity of the two

new IGV types is essential to avoid flow separation and vortex generation. In contrast to the significant stage performance improvement, during the surge test it is found that the compressor surge originates from the downstream diffuser channel, and thus cannot be directly influenced by the upstream IGVs. Therefore, the two new IGV types do not provide additional surge margin extension than what has been obtained by the baseline IGV at small mass flow rates.

The CFD results prove that the flow non-uniformity at smaller IGV setting angles (IGV = 0° and IGV = 20°), and the shifted operation point by the overturned inlet flow incidence at large IGV setting angles (IGV = 40° and IGV = 60°), are the main reasons for the baseline IGV to have deteriorated performance in comparison with the two new IGV types. For the baseline IGV at design point, the 360° circumferentially non-uniform flow at the impeller inlet and the flow unsteadiness are responsible for 0.6% of efficiency drop and 12% of total pressure variation at the impeller outlet, respectively. These two flow effects can be succesfully recaptured by the full-annulus model combined with transient CFD computation, which yet requires considerable computation cost. To save the computation resource, the new transient blade row method using FT method shoud be applied with caution because the pressure fluctuations which are not related to the blade passing frequency might be neglected.

From the experimental and numerical studies conducted by this project, it can be concluded that small pressure losses, good flow uniformity and correct flow guidance are the three decisive factors for a successful IGV design. In addition, the IGV design should be aerodynamically and mechanically optimized together with the other relevant components, for this study particularly the radial IGV plenum and the impeller, to achieve best synergic effects.

5.2 Future Prospect

Based on the results from this project, several possible directions might be considered as future work concerning the IGV design for centrifugal compressors.

- From the surge test it is found that the two new IGVs (type-B and type-C) have little impact on the extension of the surge margin than what has been obtained from the baseline standard IGV. This is because the surge for this centrifugal compressor stage mainly depends on the diffuser stall. As a next step in order to realize the performance map enhancement by further extending the surge margin, some other regulation possibilities should be considered, e.g. diffuser guide vane in Simon [75],

variable diffuser geometry in Tetu [83] and flow extraction and re-injection in Lang [59].

- Within this project, the IGV setting angle was only directly settled by a certain value input given by the operator directly. A real-time, automatic adjustment according to the feedback signals has not been realized yet. This affects the quality of adjustment especially at higher setting angles when the IGV setting angle largely deviates from the actual swirl angle. If the adjustment can be done automatically by a close-loop which constantly monitors the actual swirl angle as feedback, the overturned flow could be corrected by the control mechanism on time. Therefore, a more advanced close-loop control system may be of great value for future investigations. In fact, such type of close-loop systems have been already applied in jet engines. For example in Shaw [73], the compressor guide vanes could be adjusted based on the real-time parameters under various off-design conditions.

- During the rotating test campaign apart from the surge test, the speedlines of compressor stage with three IGV configurations were collected at the steady-state conditions. In practical applications, this centrifugal compressor needs to be operated under various unsteady operations as well, such as during the speed-up or under varying rotating speed. Therefore, the impact of IGVs while overcoming these unsteady conditions needs to be further examined.

- In this project, the IGVs were applied as a separate mechanism for the operation range extension. As a next step, the IGVs might be applied together with other types of control mechanisms at the same time, such as the diffuser guide vanes and speed control, to achieve the best synergy effects.

The ongoing project on the TUM-LFA centrifugal compressor test rig is about a combination of the IGVs in this project and a set of new guide vane configurations for the diffuser part. By performing this following project the great potential of further operation range enhancement is expected to be discovered soon in future.

Bibliography

[1] C. Aalburg, A. Simpson, J. Carretero, T. Nguyen, and V. Michelassi. Extension of the stator vane upstream across the 180 degrees bend for a multistage radial compressor stage. In *Proceedings of ASME Turbo Expo 2009, Orlando, USA*, GT2009-59522, 2009.

[2] C. Aalburg, A. Simpson, M. B. Schmitz, V. Michelassi, S. Evangelist, E. Belardini, and V. Ballarini. Design and testing of multistage centrifugal compressors with small diffusion ratios. In *Proceedings of the ASME Turbo Expo 2008, Berlin, Germany*, GT2008-51263, 2008.

[3] I. H. Abbott, A. E. Von Doenhoff, and L. Jr. Stivers. Summary of airfoil data. *NACA Technical Report NACA-TR-824, Langley Aeronautical Lab, USA*, 1945.

[4] ANSYS. *ANSYS CFX-Solver Theory Guide, Release 15.0.* ANSYS Inc., 2013.

[5] A. R. Aubry. *Return Channel Loss Reduction in Multi-Stage Centrifugal Compressors.* Master Thesis, Department of Aeronautics and Astronautics, Massachusetts Institute of Technology, 2012.

[6] S. T. Bailie, W. F. Ng, and W. W. Copenhaver. Experimental reduction of transonic fan forced response by inlet guide vane flow control. *Journal of Turbomachinery*, 132(2), 2010.

[7] E. A. Baskharone. *Principles of turbomachinery in air-breathing engines.* Cambridge University Press, 2006.

[8] T. Baumüller. *Investigation of Boundary Layer Effects on the Numerical Simulation of a Centrifugal Compressor with Inlet Guide Vanes.* Semester Thesis, Technische Universität München, 2015.

[9] E. Benvenuti. Aerodynamic development of stages for industrial centrifugal compressors, Part 1: Testing requirements and equipment - immediate experimental evidence.

In *ASME 1978 International Gas Turbine Conference and Products Show, London, England*, 1978.

[10] T. Biesinger, C. Cornelius, A. Braune, C. Rube, R. Campregher, P. G. Godin, G. Schmid, and L. Zori. Unsteady CFD methods in a commercial solver for turbomachinery applications. In *Proceedings of the ASME Turbo Expo 2010, Glasgow, UK*, GT2010-22762, 2010.

[11] H. P. Bloch. *A Practical Guide to Compressor Technology*. John Wiley & Sons, Inc., Hoboken, New Jersey, 2nd edition, 2006.

[12] R. Blumenthal, B. Hutchinson, and L. Zori. Investigation of transient CFD methods applied to a transonic compressor stage. In *Proceedings of the ASME Turbo Expo 2011, Vancouver, Canada*, GT2011-46635, 2011.

[13] C. Bode, T. Aufderheide, D. Kozulovic, and J. Friedrichs. The effects of turbulence length scale on turbulence and transition prediction in turbomachinery flows. In *Proceedings of the ASME Turbo Expo 2014, Düsseldorf, Germany*, GT2014-27026, 2014.

[14] M. Boehle, M. Cagna, and L. Itter. Compressible flow in inlet guide vanes with mechanical flaps. In *Proceedings of the ASME Turbo Expo 2004, Vienna, Austria*, GT2004-53191, 2004.

[15] D. Bonaiuti, A. Arnone, A. Milani, and L. Baldassarre. Aerodynamic analysis of a multistage centrifugal compressor. In *Proceedings of the ASME Turbo Expo 2003, Atlanta, USA*, GT2003-38495, 2003.

[16] O. Borm. *Instationäre numerische Untersuchung der aerodynamischen Rotor-Stator-Interaktion in einem Radialverdichter*. PhD Thesis, Technische Universität München, Lehrstuhl für Flugantriebe, 2012.

[17] M. P. Boyce. *Gasturbinen Handbook*. Springer-Verlag, 1999.

[18] M. Coppinger. *Aerodynamic performance of an industrial centrifugal compressor variable inlet guide vane system*. PhD Thesis, Loughborough University, 1999.

[19] M. Coppinger and E. Swain. Performance prediction of an industrial centrifugal compressor inlet guide vane system. *Journal of Power and Energy*, 214(A2):153–164, 2000.

[20] M. Coppinger and E. D. Swain. *CFD in Fluid Machinery Design - Numerical analyses and development of an industrial centrifugal compressor inlet guide vane system.* Mechanical Engineering Publications Limited, London, 1998.

[21] M. M. Cui. Unsteady flow around suction elbow and inlet guide vanes in a centrifugal compressor. *Journal of Aerospace Engineering*, 220(G1):11–28, 2006.

[22] N. A. Cumpsty. *Compressor Aerodynamics.* Longman Group UK Limited, 1989.

[23] I. J. Day. Active suppression of rotating stall and surge in axial compressors. *Journal of Turbomachinery*, 115(1):40–47, 1993.

[24] F. De Bellis, E. Guidotti, and D. T. Rubino. Centrifugal compressors return channel optimization by means of advanced 3D CFD. In *Proceedings of the ASME Turbo Expo 2015, Montreal, Canada*, GT2015-44143, 2015.

[25] R.C. Dean and Y. Senoo. Rotating wakes in vaneless diffusers. *Journal of Fluids Engineering*, 82(3):563–570, 1960.

[26] A. S. Del Greco and L. Tapinassi. On the combined effect on operating range of adjustable inlet guide vanes and variable speed in process multistage centrifugal compressors. *Journal of Engineering for Gas Turbines and Power*, 136(8):10, 2014.

[27] S. L. Dixon. *Fluid Mechanics and Thermodynamics of Turbomachinery.* Elsevier Science, 4th edition, 1998.

[28] L. Q. Duong, C. X. Hu, and N. Thayalakhandan. Inlet guide vane failure: Aeromechanical and system control interaction effect. In *Proceedings of the ASME Turbo Expo 2011, Vancouver, Canada*, GT2011-46742, 2011.

[29] N. Ebisawa, Y. Fukushima, and H. Orikasa. Dynamic simulation of centrifugal compressor startup with inlet guide vane. In *Proceedings of the ASME Turbo Expo 2011, Vancouver, Canada*, GT2011-45810, 2011.

[30] D. Eckardt. Detailed flow investigations within a high-speed centrifugal-compressor impeller. *Journal of Fluids Engineerin*, 98(3):390–402, 1976.

[31] J. I. Erdos, E. Alzner, and W. McNally. Numerical solution of periodic transonic flow through a fan stage. *AIAA Journal*, 15(11):1559–1568, 1977.

[32] D. A. Fink, N. A. Cumpsty, and E. M Greitzer. Surge dynamics in a free-spool centrifugal compressor system. *Journal of Turbomachinery*, 114(2):321–332, 1992.

[33] H. Franz. *Numerische Untersuchung der Durchströmung einer Rückführung eines mehrstufigen Radialverdichters*. PhD Thesis, Fakultät für Maschinenwesen, RWTH Aachen University, 2015.

[34] P. Frigne and R. Van den Braembussche. Distinction between different types of impeller and diffuser rotating stall in a centrifugal-compressor with vaneless diffuser. *Journal of Engineering for Gas Turbines and Power*, 106(2):468–474, 1984.

[35] Y. Funaba, T. Sato, S. Suzuki, A. Terunuma, and T. Nagahara. Unsteady fluid flow analysis as applied to the internal flow in a pump using ANSYS CFX. In *ANSYS Conference & 31th CADFEM Users' Meeting, Mannheim, Germany*, 2013.

[36] GE Oil & Gas. Centrifugal and axial compressors. *Press No. COMK/MARK 768/II*, 2013.

[37] T. F. Gelder, R. D. Moore, J. M. Sanz, and E. R. Mcfarland. Wind tunnel turning vanes of modern design. In *AIAA 24th. Aerospace Sci. Meeting*, AIAA PAPER 86-0044, 1985.

[38] M. B. Giles. Calculation of unsteady wake rotor interaction. *Journal of Propulsion and Power*, 4(4):356–362, 1988.

[39] E. M Greitzer. Surge and rotating stall in axial flow compressors, part I: Theoretical compression system model. *Journal of Engineering for Power*, 98(2):190–198, 1976.

[40] E. M Greitzer. Surge and rotating stall in axial flow compressors, part II: Experimental results and comparison with theory. *Journal of Engineering for Power*, 98(2):199–211, 1976.

[41] A. Grimaldi, L. Tapinassi, A. Bernocchi, F. R. Biagi, D. Guenard, and V. Michelassi. Impact of inlet swirl on high-speed high-flow centrifugal stage performance. In *Proceedings of the ASME Turbo Expo 2007, Montreal, Canada*, GT2007-27202, 2007.

[42] E. Guidotti, G. Naldi, L. Tapinassi, and V. Chockalingam. Cavity flow modeling in an industrial centrifugal compressor stage at design and off-design conditions. In *Proceedings of the ASME Turbo Expo 2012, Copenhagen, Denmark*, GT2012-68288, 2012.

[43] E. Guidotti, L. Tapinassi, L. Toni, L. Bianchi, P. Gaetani, and G Persico. Experimental and numerical analysis of the flow field in the impeller of a centrifugal compressor stage at design point. In *Proceedings of the ASME Turbo Expo 2011, Vancouver, Canada*, GT2011-45036, 2011.

[44] S. L. Gunter, S. A. Guillot, W. F. Ng, and S. T. Bailie. A three-dimensional CFD design study of a circulation control inlet guide vane for a transonic compressor. In *Proceedings of ASME Turbo Expo 2009, Orlando, USA*, GT2009-59360, 2009.

[45] M. D. Hathaway. NASA low-speed centrifugal compressor for 3-D viscous code assessment and fundamental flow physics research. *NASA Technical Report NASA-91-C-003*, 1991.

[46] M. D. Hathaway, R. M. Chriss, J. R. Wood, and A. J. Strazisar. Experimental and computational investigation of the NASA low-speed centrifugal compressor flow field. *Journal of Turbomachinery*, 115(3):527–541, 1993.

[47] L. He. An Euler solution for unsteady flows around oscillating blades. *Journal of Turbomachinery*, 112(4):714–722, 1990.

[48] M. Hensges. Simulation and optimization of an adjustable inlet guide vane for industrial turbo compressors. In *Proceedings of the ASME Turbo Expo 2008, Berlin, Germany*, GT2008-50242, 2008.

[49] A. Hildebrandt. Aerodynamic optimisation of a centrifugal compressor return channel and u-turn with genetic algorithms. In *Proceedings of ASME Turbo Expo 2011, Vancouver, Canada*, GT2011-45076, 2012.

[50] H. I Hill. *2D CFD Simulation of a Circulation Control Inlet Guide Vane*. Master thesis, Department of Mechanical Engineering, Virginia Polytechnic Institute and State University, 2007.

[51] D. Händel, R. Niehuis, and U. Rockstroh. Aerodynamic investigations of a variable inlet guide vane with symmetric profile. In *Proceedings of the ASME Turbo Expo 2014, Düsseldorf, Germany*, GT2014-26900, 2014.

[52] G. V. Hobson, A. Gannon, W. Holmes, M. McCormick, and V. Capece. Experimental and numerical performance characterization of a transonic compressor rotor operating behind an inlet-guide vane with variable flap angles. In *Proceedings of the ASME Turbo Expo 2014, Düsseldorf, Germany*, GT2014-27308, 2014.

[53] M. Ishino, Y. Iwakiri, A. Bessho, and H. Uchida. Effects of variable inlet guide vanes on small centrifugal compressor performance. In *ASME 1999 International Gas Turbine and Aeroengine Congress and Exhibition*, 99-GT-157, 1999.

[54] R. J. Jackson. Effects on the weight-flow range and efficiency of a typical axial-flow compressor inlet stage that result from the use of a decreased blade camber of decreased guide-vane turning. *NACA Research Memorandum NACA-RM-E52G02, Lewis Flight Propulsion Laboratory, USA*, 1952.

[55] D. Japikse. *Centrifugal Compressor Design and Performance*. Concepts ETI, Inc., 1996.

[56] Y. Kim, A. Engeda, R. Aungier, and G. Direnzi. The influence of inlet flow distortion on the performance of a centrifugal compressor and the development of an improved inlet using numerical simulations. *Journal of Power and Energy*, 215(A3):323–338, 2001.

[57] H. Krain. Review of centrifugal compressor's application and development. *Journal of Turbomachinery*, 127(1):25–34, 2005.

[58] R. Kunte. *Experimentelle und numerische Untersuchung eines Radialverdichters mit Pipe Diffusor und Umlenkbeschaufelung für eine Triebwerksanwendung*. PhD Thesis, Fakultät für Maschinenwesen, RWTH Aachen University, 2013.

[59] S. Lang, W. Erhard, H. P. Kau, R. Pannekeet, C. Aalburg, and R. d. Cauze de Nazelle. Application of flow control on a radial compressor for operating range extension. In *15th International Symposium on Transport Phenomena and Dynamics of Rotating Machinery, Honolulu, USA*, 2014.

[60] K. H. Lüdtke. *Process Centrifugal Compressors - Basics, Function, Operation, Design, Application*. Springer-Verlag, 2004.

[61] S. Leichtfuss, C. Biela, H. P. Schiffer, and F. Heinichen. Influence of inlet guide vane wakes on the passage flow in a transonic axial compressor. In *Proceedings of the ASME Turbo Expo 2012, Copenhagen, Denmark*, GT2012-69485, 2012.

[62] R. L. McAlpin, P. L. Talley, H. L. Bernstein, and R. E. Holm. Failure analysis of inlet guide vanes. *Journal of Engineering for Gas Turbines and Power*, 125(1):236–240, 2002.

[63] F.R. Menter, R. Langtry, and T. Hansen. CFD simulation of turbomachinery flows - Verfication, validation and modelling. In *European Congress on Computational Methods in Applied Sciences and Engineering, Jyväskylä, Finland*, 2004.

[64] A. Mohseni, E. Goldhahn, R. A. Van den Braembussche, and J. R. Seume. Novel IGV designs for centrifugal compressors and their interaction with the impeller. *Journal of Turbomachinery*, 134(2):8, 2012.

[65] C. Moler. *Numerical Computing with MATLAB*. Society for Industrial and Applied Mathematics, 2008.

[66] N.I.S.T. *Handbook of Statistical Methods*. NIST/SEMATECH, 2012.

[67] H. Rick. *Gasturbinen und Flugantriebe - Grundlagen, Betriebsverhalten und Simulation*. VDI-Buch. Springer-Verlag, 2013.

[68] C. Rodgers. Centrifugal compressor inlet guide vanes for increased surge margin. *Journal of Turbomachinery*, 113(4):696–702, 1991.

[69] H.I.H. Saravanamuttoo, G.F.C. Rogers, and H. Cohen. *Gas Turbine Theory*. Prentice Hall, 5th edition, 2001.

[70] J. Schmidt, P. Schwarz, B. E. Wilkosz, P. Jeschke, and C. Smythe. Detailed performance analysis of a centrifugal compressor stage with pipe diffuser and immerged tandem deswirler. In *Proceedings of the ASME Turbo Expo 2015, Montreal, Canada*, GT2015-43484, 2015.

[71] Y. Senoo and Y. Kinoshita. Influence of inlet flow conditions and geometries of centrifugal vaneless diffuser on critical flow angle for reverse flow. *Journal of Fluids Engineering-Transactions of the ASME*, 98(103), 1977.

[72] G. Sharma, L. Zori, S. Connell, and P. Godin. Efficient computation of large pitch ratio transonic flow in a fan with inlet distortion. In *Proceedings of the ASME Turbo Expo 2013, San Antonio, USA*, GT2013-95059, 2013.

[73] M. J. Shaw, P. Hield, and P. G. Tucker. The effect of inlet guide vanes on inlet flow distortion transfer and transonic fan stability. *Journal of Turbomachinery*, 136(2):021015, 2013.

[74] Siemens. Process compressors. *Press No. E50001-G420-A109-V4-4A00*, 2013.

[75] H. Simon, T. Wallmann, and T. Monk. Improvements in performance-characteristics of single-stage and multistage centrifugal compressors by simultaneous adjustments of inlet guide vanes and diffuser vanes. *Journal of Turbomachinery*, 109(1):41–47, 1987.

[76] A. Simpson, C. Aalburg, M. B. Schmitz, R. Pannekeet, V. Michelassi, and F. Larisch. Application of flow control in a novel sector test rig. *Journal of Turbomachinery*, 136(4), 2014.

[77] P. E. Smirnov, T. Hansen, and F. R. Menter. Numerical simulation of turbulent flows in centrifugal compressor stages with different radial gaps. In *Proceedings of the ASME Turbo Expo 2007, Montreal, Canada*, GT2007-27376, 2007.

[78] F. Soranna, Y. C. Chow, O. Uzol, and J. Katz. The effect of inlet guide vanes wake impingement on the flow structure and turbulence around a rotor blade. *Journal of Turbomachinery*, 128(1):82–95, 2006.

[79] R. J. Steinke and Crouse J. E. Preliminary analysis of the effectiveness of variable-geometry guide vanes to control rotor-inlet flow conditions. *NASA Technical Note TN D-3823*, 1967.

[80] S. Svensdotter, O. El Shamy, N. Ghizawi, V. Michelassi, and S. Sankaran. An optimization procedure for the aerodynamic model tuning of centrifugal compressor stages. In *Proceedings of the ASME Turbo Expo 2011, Vancouver, Canada*, GT2011-45499, 2011.

[81] H. Tamaki. Effect of recirculation device with counter swirl vane on performance of high pressure ratio centrifugal compressor. In *Proceedings of the ASME Turbo Expo 2011, Vancouver, Canada*, GT2011-45360, 2011.

[82] H. Tamaki, M. Unno, R. Tanaka, S. Yamaguchi, and Y. Ishizu. Enhancement of centrifugal compressor operating range by control of inlet recirculation with inlet fins. In *Proceedings of the ASME Turbo Expo 2015, Montreal, Canada*, GT2015-42154, 2015.

[83] L. G. Tetu. Improving centrifugal compressor performance by optimizing diffuser surge control (variable diffuser geometry) and flow control (inlet guide vane) device settings. In *International Compressor Engineering Conference*. Purdue University, 2004.

[84] W. Traupel. *Thermische Turbomaschinen - Regelverhalten, Festigkeit und dynamische Probleme*. Springer-Verlag, 2nd. edition, 1968.

[85] A Whitfield. Review of variable geometry techniques applied to enhance the performance of centrifugal compressors. In *International Compressor Engineering Conference*. Purdue University, 2000.

[86] A. Whitfield and A. H. Abdullah. The performance of a centrifugal compressor with high inlet prewhirl. *Journal of Turbomachinery*, 120(3):487–493, 1998.

[87] D. C. Wilcox. *Turbulence Modeling for CFD*. DCW Industries Inc., 3th edition, 2006.

[88] D. C. Wilcox. Formulation of the k-w turbulence model revisited. *AIAA Journal*, 46(11):2823–2838, 2008.

[89] B. E Wilkosz. *Aerodynamic Losses in an Aero Engine Centrifugal Compressor with a Close-Coupled Pipe-Diffuser and a Radial-Axial Deswirler*. PhD Thesis, Fakultät für Maschinenwesen, RWTH Aachen University, 2015.

[90] J. Yan and G. Stuckert. A study of a centrifugal compressor using mixing plane implementations. In *Proceedings of the ASME Turbo Expo 2007, Montreal, Canada*, GT2007-27344, 2007.

[91] A. Zemp. *CFD investigation on inlet flow distortion in a centrifugal compressor*. PhD Thesis, Laboratory for Energy Conversion, Swiss Federal Institute of Technology, 2007.

[92] A. Zemp. *Experimental investigation and validation of high cycle fatigue design systems for centrifugal compressors*. Master Thesis, Laboratory for Energy Conversion, Swiss Federal Institute of Technology, 2012.

[93] A. Zemp, A. Kammerer, and R. S. Abhari. Unsteady CFD investigation on inlet distortion in a centrifugal compressor. In *Proceedings of the ASME Turbo Expo 2008, Berlin, Germany*, GT2008-50744, 2008.

Appendix A

Definition of Yaw Angle

Figure A.1 illustrates the yaw angle definition at section 10 (impeller inlet section), section 20 (impeller outlet section) and section 60 (stage outlet section).

At section 10, the 3-hole probe is mounted on the hub wall (by default). Therefore, the yaw angle at section 10 is positive when the flow velocity vector is turned towards the right hole. At section 60, since the probe is mounted on the shroud wall, the yaw angle reading is inverted, thus the yaw angle at section 60 is negative when the flow vector is oriented to the left hole. At section 20, the yaw angle starts to count from the radial outward direction. For the applied backswept impeller with a clockwise rotating direction, the yaw angle is defined as positive when the absolute velocity vector falls into the counter-clockwise (backsweep) region, and is negative when the absolute velocity vector is in the clockwise (forward-sweep) region.

During the rotating test, the sign of yaw angle at section 10 denotes whether the swirl provided by the upstream IGV stage is a pre-swirl (positive) or a counter-swirl (negative). At section 20, a yaw angle less than -90° is due to a negative radial velocity component, and thus describes a reversed flow at the impeller outlet.

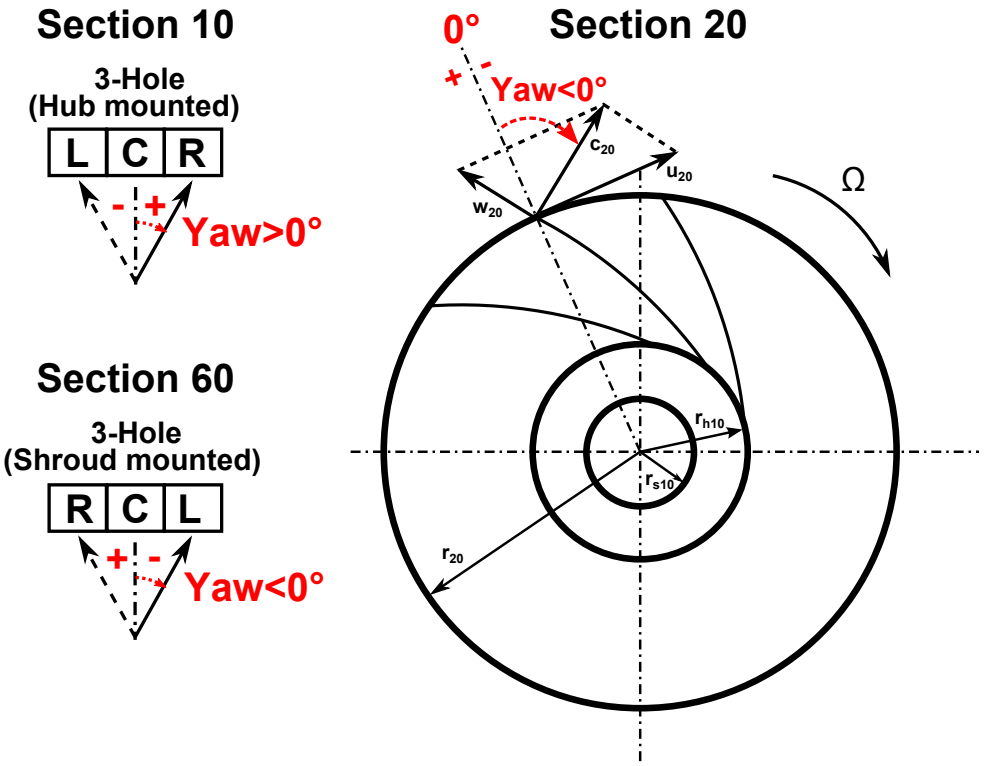

Figure A.1: Yaw angle definition for the IGV test campaign; shown are section 10, 20 and 60 seen from the stage upstream side towards the downstream side